Poly(DTE-*co*-PEG Carbonate) as a Model System for Investigating the Effects of Physicochemical Polymer Characteristics on Protein Adsorption and Cell Attachment

by
Arnold Luk

A dissertation submitted to the

Graduate School-New Brunswick

Rutgers, The State University of New Jersey

and

The Graduate School of Biomedical Sciences

University of Medicine and Dentistry of New Jersey

In partial fulfillment of the requirements

For the degree of

Doctor of Philosophy

Graduate Program in Biomedical Engineering

Written under the direction of

Joachim Kohn, Ph.D.

And approved by

Joachim Kohn
Adrian Mann
Charles Roth
Robert Latour

New Brunswick, New Jersey

October, 2010

ABSTRACT OF THE DISSERTATION

Poly(DTE-*co*-PEG Carbonate) as a Model System for Investigating the Effects of Physicochemical Polymer Characteristics on Protein Adsorption and Cell Attachment

By ARNOLD LUK

Dissertation Director:

Joachim Kohn, Ph.D

Protein adsorption is one of the first events to occur upon implantation of a biomaterial, and can modulate both the initial and long-term cellular response. Poly(ethylene glycol) (PEG) is often copolymerized with other biomedical polymers to control and reduce protein adsorption. The thermodynamic incompatibility stemming from copolymerization of a highly hydrophilic polymer such as PEG with a copolymer often results in phase separation. The spatial distribution of phase-separated structures may allow for protein adsorption to occur even in PEG-containing polymers. Physical properties that affect phase separation, such as polymer molecular weight and polydispersity, may also play a role in modifying protein adsorption behavior.

To study the physicochemical factors that modulate phase separation and subsequent protein adsorption and cell attachment, a model random multiblock hydrophobic-hydrophilic copolymer system consisting of desaminotyrosyl-tyrosine ethyl ester (DTE) as the hydrophobic component and PEG as the hydrophilic component was investigated. The effect of systematic changes in PEG molecular weight and PEG composition on phase separation was explored. The spatial effects of phase separation on protein adsorption were examined using proteins with different dimensions. Additional changes in physicochemical properties were achieved by isolating specific molecular weight chains from certain polymer compositions. Finally, the effects of phase separation on cell attachment and spreading were examined.

Variations in PEG content and molecular weight produced clear, systematic changes in the spatial distribution of hydrophobic and hydrophilic regions within each polymer composition. The effects of phase separation were initially inconclusively linked to protein adsorption behavior. However, variations in polymer molecular weight and chain distribution within certain polymer compositions appear to modulate protein adsorption capabilities. Phase separation also appears to play a significant role in cell attachment and spreading. While intermediate amounts of PEG repelled cells and proteins, high amounts of PEG caused cells to increase spreading on the polymeric substrates. The increased spreading was linked to dynamic overexpression of integrin α5 over time. The results of this study elucidate additional design parameters in the rational design of biomaterials, and also suggest that intermediate amounts of PEG may be optimal for developing cell-repellent surfaces.

Acknowledgements

There are so many people that made this thesis possible that for me to properly acknowledge all of them would probably be a thesis in and of itself. I am immensely grateful to Dr. Joachim Kohn for giving me the opportunity to work in his lab. Perhaps foolishly, I came into graduate school not actually knowing anything about doing research, and Dr. Kohn decided to take a chance on me. This document is the product of the resulting five years of honest (and sometimes necessarily harsh) feedback, incremental learning and self-discovery.

My committee members, Drs. Robert Latour, Adrian Mann, and Charlie Roth, were all instrumental in providing the perspective and input that helped this work come together. They helped me to understand where my scientific shortcomings were and how to improve on them. While sitting through those closed-door meetings wasn't ever easy, they were always constructive and I always came out with a clear sense on what needed work and what went right.

There were a number of people who helped me to somehow get through the first-year gauntlet of coursework, and those people deserve special recognition for keeping me in the game. Dr. Loreto Valenzuela (who would go on to also be part of the Kohn lab), Dr. Mike Wininger, Dr. Eric Yang, Er Liu, Nilay Shah, Aana Kim, and Aaron Seto were always available to help me understand the course material to the point where my work became at least somewhat respectable. Certainly without their help, I would never have made it this far.

My mentors, Drs. Jaap Schut, Paul Holmes, Hak-Joon Sung, and Sanjeeva Murthy, have all helped provide direction and insight for both the understanding and dissemination of the science. In particular, without Dr. Murthy's extension of the work into phase separation and small angle neutron scattering, I wouldn't have much of a thesis at all.

All of the Kohn lab people have been both wonderful colleagues and friends during my years in the lab. While there are far too many to credit since my time here at the lab, the graduate students, postdocs/faculty, and technicians have all been helpful, knowledgeable, friendly, and most importantly, patient. I would like to specially acknowledge Drs. Das Bolikal and Ramiro Rojas for helping me with the chemistry portions of my work, and for displaying an inexhaustible supply of the aforementioned patience. Dan Lewitus, and Drs. Aniq Darr, Jared Bushman, and Sanjeeva Murthy also deserve special mention for reading and revising parts of my thesis.

As for my life outside of the lab, I can't thank my good friends Tom Lamaina and Vince Sust enough for being their ridiculous selves and much-needed sounding boards for all things both mentionable and unmentionable in public. They've been sympathetic when I needed to be selfish, energetic when I was sluggish, and politically incorrect at all times.

I would also like to thank a few of the artists, some of whom I have had the pleasure of meeting in person, that have kept me level and sane during my recent life. Charlie Cooper (RIP) and Josh Eustis (Telefon Tel Aviv), Ben Watkins (Juno Reactor), Brian Transeau (BT), Tom Middleton and Mark Pritchard (Global Communication), Richard D. James (Aphex Twin), Matthew Herbert, Geoff Barrow, Adrian Utley, and

Beth Gibbons (Portishead), Akira Yamaoka, Robert Del Naja and Grant Marshall (Massive Attack), Ramble Krohn (RJD2), Josh Davis (DJ Shadow), and Aaron McGruder (Boondocks).

Finally, I'd like to thank my family, who deserve the dedication on the next page.

Dedication

To my dear family, Mom, Dad, and Debbie

For all your unconditional love and support

This would never have been possible without you.

June 2010.

Table of Contents

ABSTRACT OF THE DISSERTATION ii

Acknowledgements iv

Dedication vii

List of Tables xiii

List of Figures xv

List of Symbols and Abbreviations xxiii

1. Introduction 1

1.1. Protein adsorption – general phenomena and driving forces 1

1.2. Commonly studied proteins – general properties and roles in biocompatibility 3

1.2.1. Fibrinogen 3

1.2.2. Albumin 4

1.3. Material Effects on Protein Adsorption 5

1.4. PEG use in biomaterials and effects on protein adsorption 6

1.5. Phase separation in copolymers 8

1.6. Cellular response to phase separation 11

1.7. Tyrosine-derived polycarbonates as a model polymer system 13

1.8. Hypotheses and aims 15

1.9. Specific analytical techniques 16

1.9.1. Small Angle Neutron Scattering (SANS) 16

1.9.2. Quartz Crystal Microbalance with Dissipation (QCM-D) 18

1.10. Structure of the thesis 21

2. Materials and Methods 23
2.1. Materials used 23
2.2. Polymer synthesis 23
2.2.1. Manual polymer synthesis 23
2.2.2. Parallel polymer synthesis 25
2.3. Polymer characterization 28
2.3.1. Gel permeation chromatography (GPC) 28
2.3.2. Nuclear magnetic resonance (NMR) 29
2.3.3. Differential scanning calorimetry (DSC) 30
2.3.4. Equilibrium water content (EWC) measurement 31
2.4. Sample preparation 31
2.4.1. Compression molding 32
2.4.2. Spin-coating 32
2.4.3. Polymer fractionation 33
2.5. Atomic force microscopy (AFM) 34
2.6. Protein surface characterization – quartz crystal microbalance with dissipation (QCM-D) 34
2.6.1. QCM-D modeling 35
2.6.2. Cleaning procedure 37
2.7. Small angle neutron scattering (SANS) 37
2.7.1. SANS data analysis 38
2.8. Contact angle measurements 41
2.9. Cell studies 43

2.9.1. Cell population and spreading 43
2.9.2. Apoptosis measurement – nuclear translocation of GFP-GAPDH: 44
2.9.3. Integrin α5 expression and intracellular distribution 44
2.9.4. Fluorescence in-situ hybridization (FISH) 45
2.9.5. Quantitative polymerase chain reaction (QPCR) 46
3. Manual synthesis and characterization of poly(DTE-*co*-PEG carbonate) polymers 47
3.1. Background 47
3.2. Results 49
3.2.1. General polymer properties 49
3.2.2. Scattering from PGA and PLA 51
3.2.3. Scattering from PDLLA, PLGA 54
3.2.4. Scattering in DTE-PEG polymers: 57
3.3. Physical and biological implications 70
3.4. Initial protein adsorption studies 72
3.5. Conclusions 77
4. Parallel synthesis and characterization of poly(DTE-*co*-PEG carbonate) polymers 80
4.1. Background 80
4.2. Results and Discussion 82
4.2.1. Automated parallel polymer synthesis 82
4.2.2. Small angle neutron scattering (SANS) 84
4.2.3. Protein adsorption: 87
4.2.4. Fractionation and characterization of 20-20k 89
4.2.5. Fractionation and characterization of 11.5-1k 93

4.2.6. Contact angle and surface energy analysis 101
4.3. Conclusions 105
5. Cell response on phase-separated, DTE-PEG polymers 107
5.1. Background 107
5.2. Results 108
5.2.1. Adsorption of serum components 108
5.2.2. Cell attachment on DTE-PEG substrates 109
5.2.3. GAPDH nuclear translocation as a measure of apoptosis on DTE-PEG substrates 110
5.2.4. Cell spreading on DTE-PEG substrates 111
5.2.5. Integrin α5 spatial features and expression 112
5.2.6. Detection of intracellular integrin α5 mRNA through fluorescence in situ hybridization (FISH) 115
5.2.7. Dynamic upregulation of integrin α5 measured through quantitative polymerase chain reaction (QPCR) 116
5.3. Conclusions 118
6. Conclusions and Future Work 120
6.1. Thesis summary 120
6.2. Novelty and significance 121
6.3. Future work 123
7. Appendix 125
7.1. Spin-coating optimization for QCM-D studies 125
7.2. Sample NMRs for polymers with varying PEG molecular weights 129

7.3. NMR sample calculations 132

7.4. NMR calculation tables 134

References 137

Curriculum Vitae 149

List of Tables

Table 2.1 – Mol% and wt% of manually synthesized poly((I_2)DTE-*co*-PEG carbonate) polymers..... 24

Table 2.2 – Stock solutions prepared for automated parallel synthesis of a library of poly(DTE-*co*-PEG carbonate) polymers..... 26

Table 2.3 – weight of PEG, triphosgene (TP), and pyridine (Py) added to each reaction during automated parallel synthesis for the poly(DTE-*co*-PEG carbonate) library 26

Table 2.4 – Dispersive, polar, and total surface tension values for water, glycerol, and diethylene glycol (DEG). Values obtained from [141]. All values have units in mJ/m^2.. 43

Table 3.1 – Material properties of polymers examined with SANS..... 50

Table 3.2 – % water uptake of PGA, PLA, PDLLA, and PLGA as a function of incubation time..... 51

Table 3.3 – Effect of PEG on Z-P model parameters in non-iodinated DTE-PEG polymers..... 60

Table 3.4 – Effect of PEG molecular weight on Z-P model dimensions..... 62

Table 3.5 – Effect of temperature on Z-P parameters for selected DTE-PEG polymers.. 64

Table 3.6 – Effect of PEG in I_2DTE-PEG polymers 67

Table 4.1 – Characteristics of polymers synthesized by automated parallel synthesis. PS = phase separated, i.e. multiple T_gs present on 2^{nd} heat. 83

Table 4.2 – Glass transition data for polymers containing PEG_{35k}..... 84

Table 4.3 – Fitted Z-P dimensions and R^2 correlation coefficient for DTE-PEG library. 85

Table 4.4 – Average amount of PEG present per polymer chain as determined by measured composition and molecular weight of 20-20k fractions. 93

Table 4.5 – Contact angle measurement results for fractions of 11.5-1k and poly(DTE carbonate). Surface energy of poly(DTE carbonate) was not measured. 104

Table 7.1 – NMR calculations of manually synthesized (I_2)DTE-PEG polymers 134

Table 7.2 – NMR calculations for DTE-PEG polymers prepared by automated parallel synthesis 135

Table 7.3 – NMR calculations for fractionated 20-20k polymers 136

Table 7.4 – NMR calculations for fractionated 11.5-1k polymers 136

List of Figures

Figure 1.1 – Schematic of the biological environment of an implanted biomaterial. Proteins adsorb to the material prior to larger biological agents such as cells, platelets, and bacteria. Picture courtesy of the New Jersey Center for Biomaterials. 2

Figure 1.2 – Phase separation compared between blends and copolymers. From [81]. Reprinted with permission from AAAS. 8

Figure 1.3 – Chemical structure of poly((I_2)DTE-*co*-PEG carbonate). Iodine atoms are shown incorporated into the desaminotyrosine ring of the DTE comonomer. 15

Figure 1.4 – Schematic of the time scales for frequency, dissipation, and data acquisition in the QCM-D technique across several different overtones (Illustration courtesy of Q-Sense). 19

Figure 2.1 – Peak assignments DTE-PEG polymers in proton NMR. Figure reproduced from [104] with permission from Elsevier Limited. 30

Figure 2.2 – A sample QCM-D graph with frequency (blue line) and dissipation (orange line) of the 3rd overtone shown. Modeling limits were set from point 1 (onset of protein adsorption) to point 2 (end of rinsing step). 36

Figure 2.3 – Schematic that illustrates the parameters described by the Z-P model. Hydrated clusters are described as spheres, with a radius R, center-to-center distance d, and short range ordering of σ. In instances of zero-angle scattering, the size of large, merged clusters are described by the radius of gyration, R_g. 41

Figure 3.1 – PGA *d*-spacing and area vs. water uptake – insets: *q* vs. intensity graphs of selected points. A scattering peak is visible for the dry PGA sample due to its

semicrystalline properties. The reduced scattering peak seen at ~4% EWC is due to coincidental contrast matching between the lamellar scattering intensity and D_2O. 53
Figure 3.2 – PDLLA slope vs. water uptake: inset – sample fractal plot showing the fitted linear portion of the log-log 1-D data. Fractal analysis shows that an inflection point in the slope (21 days, 40% EWC) occurs at approximately the same time as the reported degradation of PDLLA 55
Figure 3.3 – PDLLA slope and intercept vs. temperature for 7 and 21 day incubation. Temperature scans for 7 day incubated samples show an increase in fractal dimensions, while 21 day incubated samples remain relatively constant. 56
Figure 3.4 – PLGA slope vs. water uptake. Behavior is identical to that of PDLLA. 56
Figure 3.5 – Samples of scattering data (solid circles) curve-fitted using Z-P approximation (blue lines) from hydrated polymers. a) Very weak scattering with no distinct scattering peak (DTE-13% PEG_{1k}). Error bars are omitted for all future scans to improve visibility of the data. b) A sample with a scattering peak (DTE-41% PEG_{1k}). c) A sample with both central diffuse scattering and a scattering peak (DTE-71% PEG_{2k}). 58
Figure 3.6 – SANS data for different PEG compositions. 59
Figure 3.7 – Changes in a) water *d*-spacing as a function of EWC and b) Domain radius as a function of EWC for PEG_{1k} and PEG2k polymers. Poly(DTE carbonate) and poly(I_2DTE carbonate) homopolymers did not show any scattering, and are not included in the figure. A schematic representation shows how the *d*-spacing changes as hydration occurs at low (d_l), medium (d_m), and high (d_h) water contents. 61
Figure 3.8 – Raw SANS data for DTE-41% PEG_{1k} and DTE-41% PEG_{35k}. 62

Figure 3.9 – SANS data for a) DTE-11.5% PEG_{1k}, b) DTE-24% PEG_{1k}, and c) DTE-41% PEG_{1k} at different temperatures. RT1 = initial scan at room temperature, RT2 = scan at room temperature after heating 63

Figure 3.10 – Comparisons in SANS interference peaks between DTE (blue squares) and I_2DTE (red squares) polymers containing (a) 41% and 29% PEG_{1k}, (b) 50% and 37% PEG_{2k}, and (c) 71% and 58% PEG_{2k}. The three polymer pairs contain 20mol%, 15mol%, and 30mol% PEG, respectively. 66

Figure 3.11 – Plot of the changes in the position and the intensity of the interference peak maximum in the non-iodinated series as a function of the equilibrium water uptake. 69

Figure 3.12 – A graphic representation of phase inversion, where orange represents DTE and white represents PEG. At low PEG contents, PEG is present as small domains within a DTE matrix. When PEG content increases above ~50 wt%, PEG becomes the matrix, and DTE becomes the minor component. This results in a lowered scattering intensity, and the invariant is no longer indicative of water content. 70

Figure 3.13 – Fibrinogen adsorption results for DTE-41% PEG_{100}, DTE-41% PEG_{1k}, and DTE-41% PEG_{35k}. Complete repellence was observed for the PEG_{1k}-containing material, while the PEG_{100} and PEG35k-containing materials both showed substantial adsorption. 74

Figure 3.14 – Number of ether oxygens per PEG molecule as a function of PEG molecular weight. The number of ether oxygens per molecular weight of PEG is the number of repeat units minus 1, e.g. PEG_{100} has 2 repeat units and 1 ether oxygen, while PEG_{1000} has 23 repeat units and 22 ether oxygens. 75

Figure 3.15 – Quantification of DTE-rich and PEG-rich areas based on SANS data. Dimensions for fibrinogen based on [26]. 76

Figure 4.1 – Raw scattering data (blue dots) and Z-P fit (solid black line) for DTE-PEG polymers. Panel A shows a material with a scattering peak (30-1k), indicating the formation of discrete hydrated regions. Panel B shows a material with no scattering peak (30-100), showing that water is homogeneously distributed within the sample..... 85

Figure 4.2 – *d*-spacing (Panel A) and radius (Panel B) of the DTE-PEG library. *d*-spacing and radius both increase as PEG molecular weight is increased. *d*-spacing and radius initially decrease, then remain constant from 20% to 40% PEG, indicating that domains become smaller, closer together, and more numerous. PEG_{100}-containing polymers are omitted from the graphs because of their lack of scattering as described previously..... 86

Figure 4.3 – Voigt mass-measured protein adsorption for fibrinogen (red bars) and BSA (blue bars) on a series of DTE-PEG polymers. Error bars represent standard deviation. Polymers are named by wt% PEG-MW PEG, e.g. Poly(DTE-*co*-20wt% PEG_{2k} carbonate) = 20-2k. The DTE carbonate homopolymer and PEG_{100}-containing polymers show high protein adsorption, polymers with PEG_{1k}, PEG_{2k}, and PEG_{8k} show overall protein repellence, while polymers with PEG_{20k} and PEG_{35k} show inconsistent protein adsorption. No relationship between phase separation and protein dimensions was observed. 88

Figure 4.4 – Raw QCM-D data for 20% PEG_{20k}, shortly after synthesis (Panel A), and after 1 month in storage (Panel B). Note differences in scale of frequency shift and dissipation axes. Panel A represents an adsorbed Voigt mass of approximately 2800 ng/cm^2 (modeled as described in Section 2.6.1), while Panel B shows adsorption of about 96 ng/cm^2. 89

Figure 4.5 – Weight average molecular weight and polydispersity of the 20-20k series of polymers. F1 and F3 were not run because a sufficient amount of sample could not be recovered from the fractionation process..... 90

Figure 4.6 – Protein adsorption and weight % PEG for 20-20k. Error bars represent standard deviation. n < 3 for F1 and F3 due to small amounts of sample after fractionation. *: $p < 0.05$ for all other samples. **: $p < 0.05$ for all other samples except F2 and F4. Black line – expected weight % PEG across all fractions. Red line – drawn to guide the eye between F1 and F1-2. Protein adsorption is similar for F1 and F1-2 despite the similar amount of PEG in each fraction..... 91

Figure 4.7 – Weight average molecular weight (blue bars) and polydispersity (red line) of fractions from 11.5-1k. F0 indicates the unfractionated as-is material..... 94

Figure 4.8 – Fibrinogen adsorption and weight % PEG in fractions of 11.5-1k. Error bars represent standard deviation. *: $p < 0.05$ for all samples except F2 and F3. **: $p < 0.05$ for all samples except for F1..... 95

Figure 4.9 – Correlation plot between weight average molecular weight (M_w) (red squares, dotted line), number average molecular weight (M_n) (blue diamonds, solid line), and fibrinogen adsorption for 11.5-1k. Correlations between Mw and adsorbed fibrinogen are strong, with an R^2 value of 0.82..... 96

Figure 4.10 – GPC chromatograms of blends with 11.5-1k fractions. a) 50/50 blend of F1-1 and F1-2, b) 90/10 blend of F1-1 and F1-2, c) 50/50 blend of F1-1 and F4, d) 90/10 blend of F1-1 and F4. M_ws show a weighted averaging effect. Polydispersity (Pd) shows a weighted averaging effect for blends of F1-1 and F1-2, while Pd is increased when F1-1

is blended with F4 due to the appearance of multiple peaks or a shoulder for the 50/50 blend and the 90/10 blend, respectively. 98
Figure 4.11 – QCM-D results of Fg adsorption onto blends of fractions of 11.5-1k. Error bars represent standard deviation. * - $p > 0.05$ compared to all other samples. Fg adsorption does not show a weighted average between blends, as blending with just 10% of another fraction reduces protein adsorption by 50% compared to F1-1, regardless of the fraction used. Blending with a 50/50 ratio further decreases Fg adsroption. 99
Figure 4.12 – A schematic of contact angle measurements of wetting (left) and non-wetting (right) surfaces. 101
Figure 4.13 – A schematic of how liquid spreading is affected by morphological features. The movement of the drop along the surface can be impeded by high or low energy features during its advancing or receding motion. Image reproduced from with permission from [139]. Copyright owners: Springer Science and Business Media. 102
Figure 4.14 – A sample fit of the x and y parameters for the Fowkes approximation in determining surface energy. The slope and intercept of the linear fit are used to calculate the surface energy. 103
Figure 4.15 – Contact angle hysteresis, surface energy, and fibrinogen adsorption for poly(DTE carbonate) and fractions of 11.5-1k. Error bars represent standard deviation. *: $p < 0.05$ vs. all other samples for contact angle hysteresis. Surface energy was not measured for poly(DTE carbonate). While surface energy is relatively constant between each 11.5-1k material, hysteresis varies significantly between the “as is” polymer and the fractions, suggesting that PEG is more homogeneously distributed on the surface of the “as is” polymer. 105

Figure 5.1 – Fetal bovine serum adsorption for DTE homopolymer, PLLA, and DTE-PEG polymers (n=3). Error bars represent standard error. Increases in PEG lower protein adsorption to negligible levels at greater than 24% PEG. 109

Figure 5.2 – Cell attachment of SaOS-2 cells on DTE homopolymers, PLLA, and DTE-PEG substrates (n=4). Error bars represent standard error. 110

Figure 5.3 – GAPDH green fluorescence nucleus-to-cytoplasm ratio as a marker for apoptosis. Increasing amounts of PEG result in higher GAPDH nuclear translocation. Error bars represent standard error. *: $p < 0.05$ vs. DTE homopolymers. 111

Figure 5.4 – Cell spreading of SaOS-2 cells on PEG-containing DTE polymers, DTE homopolymer, and PLLA. Error bars represent standard error. *: $p < 0.05$ vs. 20% and 24% PEG (n=16) 112

Figure 5.5 – Representative samples of cell spreading and integrin α5 localization of GFP-integrin α5 SaOS-2 cells 114

Figure 5.6 – Immunostained integrin α5 protein levels normalized to cell area. (n=25). Error bars represent standard error. *: $p < 0.05$ vs. DTE homopolymers. 115

Figure 5.7 – In situ hybridization for expression of mRNA. Error bars represent standard error. All polymers are significantly different from each other, $p < 0.05$ 116

Figure 5.8 – QPCR of integrin α5 RNA at 24 hours relative to 4 hours. Error bars represent standard error. *: $p < 0.05$ for 24% PEG and 41% PEG vs. DTE and 11.5% PEG 118

Figure 7.1 – General spin-coating procedure [191]. Image reproduced with permission from copyright owners, The Society for Imaging Science and Technology. 126

Figure 7.2 – AFM image from poly(DTE carbonate) spin-coated from a 1% w/v solution in THF. Large holes are present on the surface. 127

Figure 7.3 - AFM image for poly(DTE carbonate) spin-coated from a 1% w/v solution in sieved THF. Small holes are still present, even after using molecular sieves. 128

Figure 7.4 – AFM image from poly(DTE carbonate) spin-coated from a 1% w/v solution in sieved dioxane. Surfaces appear to be smooth and pinhole-free. 129

Figure 7.5 – NMR overlay of poly(DTE-co-41wt% PEG_{100} carbonate) (red), poly(DTE-co-41wt% PEG_{1k} carbonate) (green), and poly(DTE-co-41wt% PEG_{35k} carbonate) (black). 131

Figure 7.6 – NMR overlay of poly(DTE-co-41wt% PEG_{100} carbonate) (red), poly(DTE-co-41wt% PEG_{1k} carbonate) (green), and poly(DTE-co-41wt% PEG_{35k} carbonate) (black) between 3.3 and 4.6 ppm. 132

Figure 7.7 – Sample NMR of 20-1k. 134

List of Symbols and Abbreviations

General Abbreviations

AFM – atomic force microscopy

BSA – bovine serum albumin

D_2O – deuterium oxide, a.k.a. heavy water

DEG – diethylene glycol

DI – deionized

DMF – N, N-dimethylformamide

DMSO – dimethylsulfoxide

DPBS – deuterated phosphate buffered saline

DSC – differential scanning calorimetry

DTE – desaminotyrosyl-tyrosine ethyl ester

EWC – equilibrium water content

Fg – fibrinogen

FITC – fluorescein isothiocyanate

GAPDH – glyceraldehyde 3-phosphatase dehydrogenase

GFP – green fluorescent protein

GPC – gel permeation chromatography

HFIP - hexafluoroisopropanol

I_2DTE – di-iodo-desaminotyrosyl-tyrosine ethyl ester

IPA – isopropanol

MeCl – methylene chloride

MW – molecular weight

M_n – number average molecular weight

M_w – weight average molecular weight

NIH – National Institute of Health

NMR – nuclear magnetic resonance

ORNL – Oak Ridge National Laboratories

PBS – phosphate buffered saline

PDLLA – poly(D,L-lactic acid) – denotes an approximately 1:1 mixture of the D and L isomers

PEG – poly(ethylene glycol)

PFA – paraformaldehyde

PGA – poly(glycolic acid)

PLA – poly(lactic acid), denotes unspecified mixture between D and L isomers, with a large majority of the L isomer

PLGA – poly(lactic-co-glycolic acid)

Py – pyridine

QCM-D – quartz crystal microbalance with dissipation

QPCR – quantitative polymerase chain reaction

SAND – small angle neutron diffractomemter at Argonne National Laboratories

SANS – small angle neutron scattering

TEM – transmission electron microscopy

TFA – trifluoroacetic acid

T_g – glass transition temperature

TGA – thermogravimetric analysis

THF – tetrahydrofuran

T_m – melting temperature

TP – triphosgene

Z-P – Zernicke-Prins

Small angle neutron scattering terms

q – scattering vector ($Å^{-1}$)

$d\Sigma/d\Omega$ – absolute intensity (cm^{-1}). For purposes of this thesis, it is analogous to $I(q)$.

d-spacing – center-to-center distance between hydrated domains (Å)

I_0 – initial intensity

R – radius of scattering bodies

σ – the spread in *d* (lower value indicates more uniformity in distances, and vice versa)

I_{CDS} – central diffuse scattering intensity

R_g – radius of gyration

Quartz crystal microbalance with dissipation terms

f – frequency (Hz)

d – dissipation (unitless)

m – Voigt mass (kg/m^2)

C – Sauerbrey constant, 17.7 ng/(Hz-cm^2)

δ – Voigt layer thickness (m)

ρ – Voigt layer density (kg/m^3)

Contact angle/surface energy terms

θ_a – advancing contact angle (°)

θ_d – receding contact angle (°)

γ_l – total liquid surface tension (mJ/m^2)

γ_l^d – dispersive component of the liquid (mJ/m^2)

γ_l^p – polar component of the liquid (mJ/m^2)

γ_s – total surface energy (mJ/m^2)

γ_s^p – polar component of the surface (mJ/m^2)

γ_s^d – dispersive component of the surface (mJ/m^2)

1. Introduction

1.1. Protein adsorption – general phenomena and driving forces

Protein adsorption is often considered to be the "first observable event" at the fluid-material interface [1]. Proteins in solution that come in contact with a material surface will adsorb within minutes. This event has significant implications in a number of industries. In marine applications, barnacles, mussels, and algae can stick to equipment and ship hulls through protein-mediated means, resulting in decreased efficiency and speed [2-3]. In the food industry, undesired protein adsorption from bacterial secretions, known as fouling, can contaminate food processing equipment and product [4]. Similarly, protein adsorption predictably plays a large role in the performance of biomedical devices, where an implanted biomaterial can come in contact with protein-rich fluids such as blood, synovial fluid, and cerebrospinal fluid. As proteins approach a surface, they vie for open positions on a material surface and upon adsorption, serve as modulators of future cellular behavior [5-9]. To this end, proteins can be considered the front-line agents that determine the success or failure of a biomaterial. A schematic of this phenomenon is given in Figure 1.1.

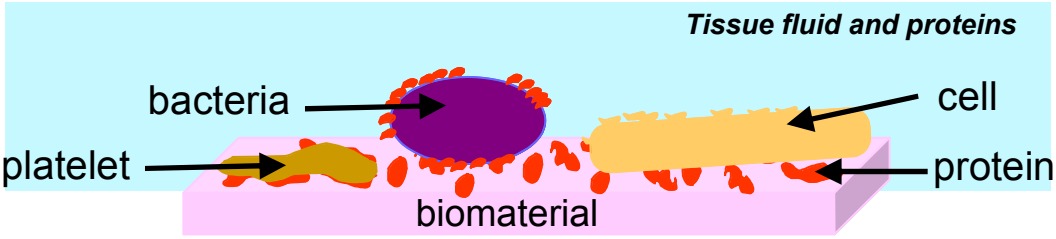

Figure 1.1 – Schematic of the biological environment of an implanted biomaterial. Proteins adsorb to the material prior to larger biological agents such as cells, platelets, and bacteria. Picture courtesy of the New Jersey Center for Biomaterials.

Protein adsorption is a thermodynamically driven event that is affected by a number of factors in both the polymer surface and the protein structure. As proteins approach a synthetic surface, they interact with the surface through van der Waals forces, electrostatic interactions, and hydrogen bonding [10]. Over time, the adsorbed proteins will rearrange and adopt a lowest-energy conformation [11]. This attempt to minimize free energy typically involves some degree of denaturation of the protein's native structure [12]. The degree of denaturation may vary greatly depending on the protein and surface, though more stable, "rock-like" proteins such as lysozyme tend to undergo very little change, while flexible proteins such as bovine serum albumin (BSA) may change drastically [10, 13].

The phenomenon of protein adsorption is one of constant motion and optimization, reliant on both the bulk concentration of proteins available as well as the presence of other species. Proteins that first adsorb to a surface are typically smaller proteins that are present at higher concentrations [14]. In blood, albumin is typically the protein that represents these characteristics [15]. However, over time, larger, higher-affinity proteins can displace low-affinity proteins [16-17]. This phenomenon is termed the Vroman effect. The Vroman effect also states that maximum protein adsorption

generally occurs at intermediate protein concentrations [6, 18]. These observations show that protein adsorption is a dynamic process that can occur over multiple length scales.

Protein adsorption strongly affects biomaterial function and biological response. Undesirable adsorption can range from mere inconveniences, such as fouling of contact lenses that results in decreased vision [19], to life-threatening, as evidenced by thromboembolytic events and restenosis that can occur in vascular stents [20-21]. On the other hand, protein adsorption is necessary for tissue regeneration materials. For example, tissue regeneration scaffolds that adsorb higher amounts of adhesive protein also report improved cell attachment properties [22]. In aneurysm coils, protein adsorption and subsequent thrombus formation serve the dual purpose of reducing the chances of aneurysm rupture and acting as a "provisional scaffold" for re-endothelialization [23-24].

1.2. Commonly studied proteins – general properties and roles in biocompatibility

Fibrinogen and albumin are two of the most widely studied proteins when examining the suitability of biomaterials for *in vivo* applications. Both are present at high concentrations in the blood, and serve as appropriate representative proteins for determining biocompatibility.

1.2.1. Fibrinogen

Fibrinogen is present in the blood at a concentration of 3 mg/mL and is responsible for hemostasis following an injury [25]. It is a rod-like protein with

dimensions of 4.5 nm x 4.5 nm x 46 nm [26]. Several amino acid sequences on the fibrinogen molecule interact with the glycoprotein IIb-IIIa receptor on platelet surfaces, and interactions between this receptor on activated platelets and fibrinogen results in thrombus formation and the clotting cascade [27-28]. Fibrinogen has extremely high surface activity, and can adsorb to a wide variety of substrates [7]. Fibrinogen has previously been implicated as the main blood protein responsible for chronic inflammation in implanted biomaterials [29]. Studies have shown that as few as 7 ng/cm^2 of adsorbed fibrinogen is enough to cause a high level of platelet recruitment [30]. Because of its commercial availability and highly relevant biological consequences, fibrinogen is one of the most widely studied proteins in determining the biocompatibility of a candidate material.

1.2.2. Albumin

Albumin is one of the most abundant proteins in blood, present at a concentration of 40-60 mg/mL [15]. For economical reasons, bovine serum albumin (BSA) is often substituted for human serum albumin in most protein research. The high homology between the two molecules [31] suggests that the impact of this change is minimal. BSA has been previously characterized as a prolate ellipsoid, with dimensions of 4 nm x 4 nm x 14 nm [32]. The difference in size compared to the relatively rod-like fibrinogen has allowed researchers to use it as a probe for nanometer-level features in surfaces and layers [12, 33]. However, charge effects for both proteins should be minimal, or at least identical, in saline-buffered conditions, as both have isoelectric points below 7.4 (4.7 for

BSA [34] and 5.7 for fibrinogen [35]). In stark comparison to fibrinogen, albumin is often considered to be a non-reactive protein, as several researchers have shown that albumin is able to passivate surfaces [29, 36-37].

1.3. Material Effects on Protein Adsorption

Several material parameters dictate the ability of a surface to adsorb proteins, including chemistry, charge, roughness, surface energy, and morphology. Regarding surface chemistry, the reader is directed towards excellent articles by Ostuni et al. about the role of chemical functional groups in the ability of a material to adsorb proteins [38-39]. In short, they arrived at the following four properties to generalize the characteristics of protein-repellent surfaces: they are 1) hydrophilic, 2) hydrogen bond acceptors, 3) not hydrogen bond donors, and 4) neutrally charged. Poly(ethylene glycol) (PEG) is one of the materials that fulfills these requirements, and is commonly used as a protein-repellent material. Its properties and usage in copolymer systems is a central focus point of this thesis, and will be discussed at length in the coming sections.

Because many proteins contain charged “pockets” within their structure, the hydrophobicity or hydrophilicity of a surface may dictate the adsorption of certain proteins in a solution over others [40-42]. Also related to the charge of the material is the surface energy. Baszkin and Lyman reported that contact angle can differentiate between polar and dispersive components of a surface, and that these properties can grossly predict the protein adsorptive behavior of a material [43]. Material topography plays an

important role as well, as rougher surfaces result in higher surface area and therefore higher adsorptive capabilities [44].

Another potential material variable for protein adsorption is the morphology of substrate. Morphological features typically arise from a combination of compositional and architectural variables, e.g. how much of each copolymer is present, and how they are copolymerized (graft, block, random, etc.). For homopolymers or copolymers with one largely dominant component, the morphology of the material will tend to be a non-factor. However, two relatively unlike monomers blended or copolymerized at certain quantities may form specific structures to lower their interfacial energy, an event which is called phase separation. The resulting morphological features from phase separation have been shown to affect surface properties, protein adsorption, and cellular behavior [45-51].

This thesis will focus specifically on the interplay between two of these material effects, polymer chemistry and morphology, and how they affect biological properties such as protein adsorption and cell attachment. These two features are discussed in greater detail in the following sections.

1.4. PEG use in biomaterials and effects on protein adsorption

Modulation of protein adsorption to achieve a specific design criterion is an important consideration in biomaterial design. One of the most successful materials for use in protein repellence is poly(ethylene glycol) (PEG). Some of the first clues to the biological inertness of PEG were observed by Abuchowski et al., who discovered that modification of BSA with PEG completely removed any immunogenicity of the protein

[52]. PEG was first discovered to be a protein-repellent biomaterial in the early 1980s by Mori et al., when they noted that grafting the material onto poly(vinyl chloride) (PVC) achieved high levels of protein repellence in an *in vivo* model [53]. Since then, research on this particular polymer for purposes of protein adsorption modulation has grown considerably.

The unique interactions of PEG with water are illustrated when one realizes that similar polymers, namely poly(methylene glycol) and poly(butylene glycol) are both insoluble in water [54]. In particular, poly(methylene glycol) has a higher ether oxygen "density" than PEG, but its insolubility in water compared to PEG suggests that PEG has a specific structure that allows it to associate optimally with water. While the exact mechanism behind the protein repellent properties of PEG remains a source of debate, it is generally accepted that a combination of steric, entropic, and thermodynamic effects are responsible for the ability of PEG to repel proteins. When a protein first encounters a PEG group, its approach compresses a PEG chain such that water associated with the ether oxygens is released. Both the compression of the PEG chain as well as the expulsion of water during compression of the chain (as many as three water molecules per ether oxygen [55]) tends to be thermodynamically unfavorable [56-57], resulting in the repulsion of proteins.

To achieve protein repellence, surfaces are often modified with PEG or PEG-containing structures, such as grafts [12, 33, 53, 58-63], self-assembled monolayers [64-70], and block copolymers [71-77]. In particular, graft copolymers are used because of their ability to functionalize a large number of surfaces and to maximize mobility, and therefore repellent capabilities, of PEG on the surface [78]. The key parameters for

determining the efficacy of protein adsorption are graft density and PEG molecular weight [79]. Increasing graft density increases the PEG chains on the surface, while increasing the PEG molecular weight provides protein repulsion for reasons explained previously.

1.5. Phase separation in copolymers

A complication that may occur in copolymers with highly hydrophilic polymers such as PEG is phase separation, or the spontaneous formation of separate, concentrated regions of a polymer within the bulk or surface. Leibler described the phenomenon of phase separation in his seminal work [80]. Essentially, phase separation in idealized diblock copolymers (i.e. where polydispersity is 1 and both blocks are the same molecular weight) is dependent on three parameters: the Flory-Huggins interaction parameter, the degree of polymerization, and the molar fraction of each copolymer unit.

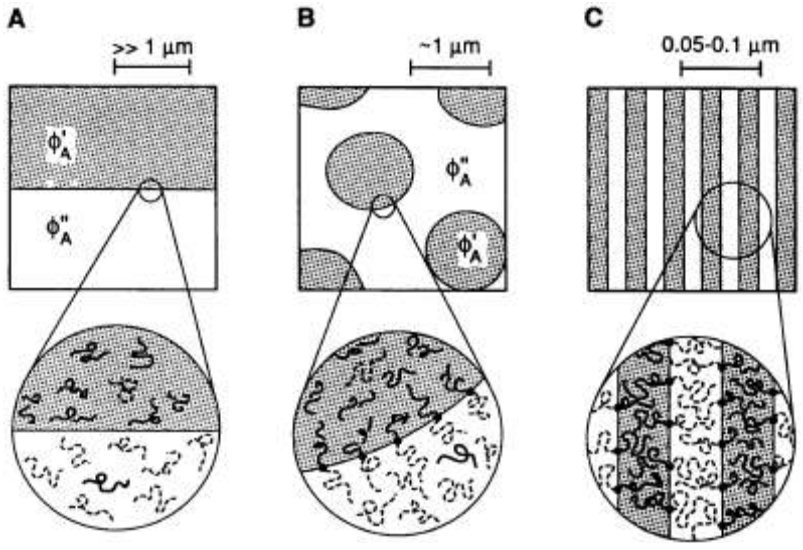

Figure 1.2 – Phase separation compared between blends and copolymers. From [81]. Reprinted with permission from AAAS.

Specific morphologies have been established for many diblock and triblock copolymer systems by varying these parameters, and the distance between the phase-separated domains tends to be on the order of 50-100 nm [82-83]. Phase separation has been shown to modulate the behavior of adsorbed proteins. In block copolymers with well-defined phases, proteins will adsorb preferentially to one phase over the other [41-42, 84], effectively patterning the surface with proteins.

The phase behavior of random copolymers, by comparison, has not been well-studied, though some theoretical work has been performed that suggests that the phase separated structures are in general smaller and far more complex than those seen in diblock or triblock copolymers [85-86]. Though their exact morphological structure of is more difficult to characterize, random copolymers provide various advantages versus their more organized counterparts. They are typically easier and cheaper to synthesize because fewer controls are required to obtain a specific structure [87]. Additionally, the relative intermixing of the different chemical components often results in materials that are stronger or tougher than diblock or triblock copolymers [88-89]. In biomaterial applications, benefits have been seen in tribology studies, where random copolymers have been observed to provide more uniform and predictable behavior between bulk and surface properties in implanted load-bearing devices compared to block copolymers and polymer blends [90]. All of these beneficial properties may be attributed to morphological properties resulting from nanophase separation that occurs at length scales smaller than those from diblock or triblock copolymers [87].

Perhaps because of their relatively homogeneous morphology, protein adsorption on random, PEG-containing polymers has been studied on a limited basis. It should be

noted that monomeric units copolymerized with PEG in a random conformation are random multiblock copolymers by definition, as opposed to true random copolymers, because individual ethylene glycol mers are very rarely used in copolymers. Nevertheless, as mentioned previously, the effects of PEG copolymerization with other monomeric units are typically studied with PEG existing as a diblock, triblock, or graft copolymer. It has been shown that many of the same factors that affect protein adsorption, such as PEG molecular weight and PEG composition, are the same for both random multiblock and graft copolymers, namely, proteins will be repelled either PEG concentration is increased, or when PEG molecular weight is increased [91].

However, if PEGylated random multiblock copolymers phase separate, the separation would be facilitated by increasing the block size of PEG, thereby reducing the possibility that the other polymer component can interrupt continuous PEG chains. It may therefore be possible that the increased spatial distance between PEG-rich domains may allow for proteins to adsorb by virtue of having large hydrophobic regions. The idea that spatial distances between PEGylated regions may repel proteins of varying sizes has previously been investigated by Sofia et al. [92] They calculated the critical distance between star-grafted PEG brushes could determine whether certain proteins could adsorb to a silicon surface as a function of brush density, brush size, and protein size. If PEG-containing random multiblock copolymers can also be quantified as such, it may be possible that the adsorptive capabilities of a surface can be determined through its structure.

It has been previously shown that molecular weight and polydispersity can affect polymer morphology [93]. Because phase-separated structures tend to affect protein

adsorption in ways that homogeneous surfaces do not, it then follows that molecular weight and polydispersity may play key roles in the protein adsorption behavior of a biomedical polymer. However, this link has not yet been established in the literature definitively, despite its potentially vast importance in the manufacturing control of biomedical materials.

1.6. Cellular response to phase separation

As discussed previously, morphological features resulting from phase separation can alter protein adsorption. Preferential protein adsorption to a certain phase essentially creates a patterned surface that cells will attempt to attach to and navigate. Cellular attachments to surfaces are modulated by focal adhesions. Specifically, integrin receptors present on the surface are responsible for associating with extracellular matrix proteins to regulate processes such as attachment. The presence or absence of interactions with matrix proteins facilitates signaling within the cell to undergo processes such as proliferation or apoptosis, respectively [94-96].

Several studies have examined how cells respond to spatial effects induced by polymer morphology. Khor et al. examined a polystyrene-block-poly(vinylpyridine) system that exhibits either a dot-like or worm-like morphology through variations in polymer chemistry molecular weight [48]. They found that surfaces that exhibited a worm-like lamellar morphology were able to more readily adsorb proteins and facilitate cell attachment. By contrast, a dot-like morphology did not accommodate cells as well, and cells on these surfaces exhibited significantly more filopodia, as though the cells

were constantly trying to find a suitable region to attach to. The results suggest that large, continuous phases of a hydrophobic polymer are better suited for allowing cells to attach and proliferate, while, erratic surfaces with "islands" stress cells into a constant state of seeking out an appropriate region for attachment.

A study by Seo et al. used a triblock copolymer system consisting of poly(2-methacryloyloxyethyl phosphorylcholine) (PMPC) as a hydrophilic segment and poly(dimethylsiloxane) (PDMS) as a hydrophobic segment [49]. By varying the compositions of each block, they were able to modulate cell attachment such that by increasing the hydrophilic block content, cells were poorly spread and attached, while increasing the hydrophobic block content allowed for cells to attach, spread, and proliferate readily. Most interestingly, they noted that random copolymerization of MPC with other molecules results in high repellence of proteins and cells [97]. This study further reinforces that material morphology and architecture can affect biological behavior. However, the threshold and characteristics of the "tipping point" for materials to transition between protein and cell permissiveness and repellence remains unknown. The apparent link between spatial characteristics and biological behavior makes the investigation and discovery of this information a potentially powerful tool in the rational design of biomaterials for tissue regeneration.

To examine the effects of PEG in a phase-separated system and its biological consequences, a model random multiblock copolymer system of hydrophobic tyrosine-derived polycarbonates copolymerized with PEG will be studied. This system is well-suited for this thesis work due to its versatility in examining multiple chemical, physical,

and biological properties. The properties of the system are elaborated upon in the following section.

1.7. Tyrosine-derived polycarbonates as a model polymer system

Tyrosine-derived polycarbonates have been previously examined in a number of different biomedical applications, such as vascular stents [98], bone regeneration pins [99], and drug-delivery nanospheres [100]. Because of the numerous variations that are possible with these materials, such as changes in pendent chain length, [101], addition of desaminotyrosyl-tyrosine [102], incorporation of iodine [98, 103], and copolymerization with PEG [104], they serve as an ideal polymer system for studying how systematic structural changes can affect overall polymer properties. Polymer molecules are arranged randomly upon polymerization [105] and, barring incorporation of a large amount of a crystalline material, the polymers exhibit an amorphous morphology.

Of the tyrosine-derived poly carbonates, poly(desaminotyrosyl tyrosine ethyl ester carbonate) (poly(DTE carbonate)) is one of the most extensively studied. It is a relatively stiff, hydrophobic polymer that induces a lower inflammatory response compared to both other commonly studied biomaterials and other polymers in the tyrosine-derived polycarbonate family [99, 106-107]. It also demonstrates high protein adsorption at around 2.4 $\mu g/cm^2$ as measured by QCM-D [108]. Synthetic schemes regarding copolymerization with PEG and basic characterization has been described previously [104]. Additionally, the effect of PEG molecular weight was studied by increasing block size from 1000 to 20000, which resulted in an increased tensile strength, but lower

elongation at failure, with no notable changes in thermal properties aside from the presence of a melting peak at higher molar percentages of PEG_{20000} [104]. However, the biological consequences of increasing PEG block size in this polymer system are still unknown.

Incorporation of iodine into the desaminotyrosine (Dat) ring of DTE imparts the molecule with radio-opacity. This monomer is called di-iodo-desaminotyrosyl-tyrosine ethyl ester, or I_2DTE. The clinical effects of this modification are beneficial, as devices made from such a material may be visualized during insertion, a property foreign to the overwhelming majority of polymers. This property has been exploited for the use of I_2DTE-containing materials as degradable polymeric vascular stents [98].

Incorporation of iodine can affect the polymer in significant ways. Macario et al. studied the effects of I_2DTE on various polymer properties, such as hydrophobicity, surface composition, and protein adsorption [103]. I_2DTE-containing polymers are markedly more hydrophobic than DTE-containing polymers, as determined by contact angle. Additionally, iodine seemed to restrict the migration of PEG to the surface of polymers containing both I_2DTE and PEG, compared to DTE-co-PEG polymers. These properties in combination lead to increased protein adsorption with iodinated polymers compared with non-iodinated polymers. The incorporation of iodine also increases the glass transition temperature significantly (136 °C for poly(I_2DTE carbonate) vs. 96 °C for poly(DTE carbonate)), which implies that the increased stiffness of the iodinated polymer may be the result of steric hindrance that is caused by the bulky iodine atoms.

The potential phase separation behavior in PEG-containing polymers with DTE and I_2DTE will be described in Chapter 3. The effect of PEG block size and PEG

composition in DTE-containing polymers will be focused upon in Chapter 4. The chemical structure of poly((I_2)DTE)-co-PEG carbonate)s is given in Figure 1.3.

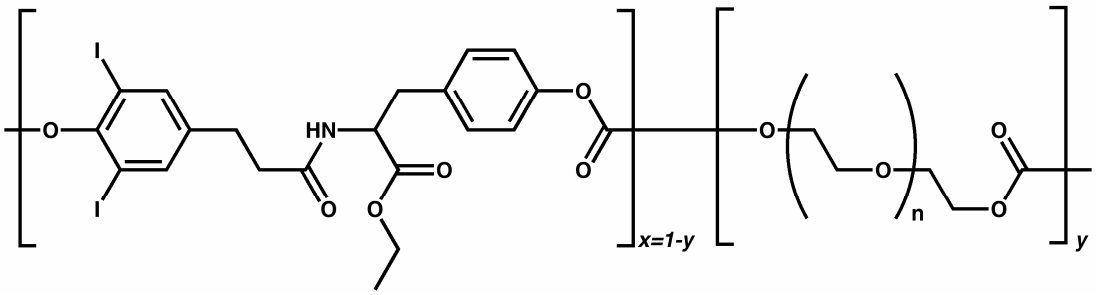

Figure 1.3 – Chemical structure of poly((I_2)DTE-*co*-PEG carbonate). Iodine atoms are shown incorporated into the desaminotyrosine ring of the DTE comonomer.

1.8. Hypotheses and aims

There are three hypotheses in this thesis:

1. Phase separation occurs in a quantifiable manner in random, multiblock copolymers with distinct hydrophobic (DTE) and hydrophilic (PEG) components, such that changes in chemistry, such as increasing or decreasing the concentration and molecular weight of the hydrophilic block, affect morphology and the spatial distribution of phase-separated regions.
2. The spatial distribution of PEG affects protein adsorption in such a way that large hydrophobic patches can support protein adsorption of different sized proteins.
3. Subsequent cell attachment and spreading to a phase-separated surface is affected by the spatial distribution of PEG-rich regions such that larger hydrophobic patches will allow cells to spread more.

To answer these hypotheses, the following three aims are proposed:

1. Establish and synthesize a hydrophobic/hydrophilic polymer system that spans a sufficiently wide range of chemical and morphological properties such as PEG molecular weight, PEG concentration, and overall polymer molecular weight.
2. Characterize these physicochemical factors and determine their quantitative effects on phase separation of each material.
3. Determine how these chemical and morphological factors affect biological phenomena through investigation of protein adsorption and cell attachment.

1.9. Specific analytical techniques

Aside from traditional characterization techniques to determine standard polymer properties, several specialized techniques will be used to determine characteristics of phase separation and protein adsorption in this study. These techniques, small angle neutron scattering and quartz crystal microbalance with dissipation, are discussed in more detail below.

1.9.1. Small Angle Neutron Scattering (SANS)

SANS is one of the small angle scattering techniques that can be used to determine the nanoscale morphology of a material. Because neutrons are far more massive than other commonly used scattering bodies, such as electrons, they can readily penetrate into the bulk of a material. The technique has been used in determining molecular features such as polymer structural changes after swelling in solvent [109-110]

and after temperature application [111], and protein conformation during hydration [112]. For polymers, it can be used to deduce fine structural details such as lamellar structure [113], particle aggregation [114], and nanoscale phase separation [115].

The process of neutron scattering can briefly be described as follows: a collimated beam of neutrons penetrates a sample, and incident neutrons will deflect off neutrons in the sample. Based on the angle of deflection from the incident beam through the sample and onto a detector, a scattering pattern can be determined. 1-dimensional reduction of this scattering pattern provides a plot of q, the scattering vector, versus intensity. A rough estimate of the distance, or d-spacing, of scattered bodies can be determined by the equation:

$$d = \frac{2\pi}{q} \tag{1.1}$$

From this equation, it is clear that large intensity peaks at low q scattering vectors indicate that scattering bodies are farther apart.

1.9.1.1. SANS Data Analysis

Many amorphous structures, while lacking a distinct scattering peak, can give scattering data in the shape of a power law pattern, with high intensity at low q values and vice versa. Martin and Hurd have previously described that this data can be modeled in such a way that the slope of a Porod log-log plot of the q vs. intensity data can indicate the fractal dimension of the sample [116-117]. In short, the fractal dimension gives an indication of both the order and the dimension of the material. An increase in the fractal

dimension indicates a "roughening" of the scattered body. For example, a material with a fractal dimension of 2.5 can be thought of as a pockmarked plane, such as a "pothole filled-road" (N.S. Murthy, personal communication), while a material with a fractal dimension of 3.5 indicates a roughened 3-dimensional object, like a golf ball. Information about the fractal dimension of an amorphous polymer can potentially be related to the gross morphology of a material.

Materials that exhibit nanophase inhomogeneities show a distinct scattering peak when measured by SANS. In many cases, *a priori* knowledge (e.g. whether a material is crystalline or amorphous) of a system is necessary to properly analyze this scattering curve from a polymer system. If no such knowledge exists, however, attempting to fit a curve to a model may serve as a "brute force" method of obtaining this information. One relatively simple model for modeling SANS data is the Zernicke-Prins (Z-P) model, which assumes that scattered bodies are spherical in shape [118]. The model is described in detail in Section 2.7.1.

1.9.2. Quartz Crystal Microbalance with Dissipation (QCM-D)

QCM-D is a technique that is gradually gaining recognition as a well-suited technique for measuring interfacial phenomena. While QCM has been around for several decades, the dissipation variant of this technique has only been commercially available for just over a decade. Some recent applications of QCM-D include measurement of substrate hydration and swelling [119], layer-by-layer deposition [120-121], detection of

substrate conformational changes [122-123], in-situ crosslinking [124-125], detergent activity [126], and protein adsorption [108, 127-128].

The main advantages of QCM-D are its high sensitivity (on the order of ng/cm^2), ability to measure in real time under temperature controlled conditions, and its relatively simple operation setup. The machine simply requires a power outlet and computer for data acquisition, and because it is a gravimetric technique, it can measure materials directly, and does not rely on secondary detection methods such as fluorescently conjugated antibodies. The basic function is as follows: an alternating current is applied to a quartz crystal, causing the crystal to oscillate its fundamental frequency. As mass adsorbs to the crystal, the oscillation frequency will decrease. To measure dissipation, the driving voltage is cut at set intervals, and the amount of time required for the crystal to come to rest is measured. The QCM-D measurement process is detailed in Figure 1.4. Viscous surfaces that come to rest quickly are considered to be high-dissipation surfaces, while more rigid surfaces will come to rest slowly, and are considered to be low-dissipation surfaces. To measure different penetration depths and distances, overtones of the fundamental frequency are also employed.

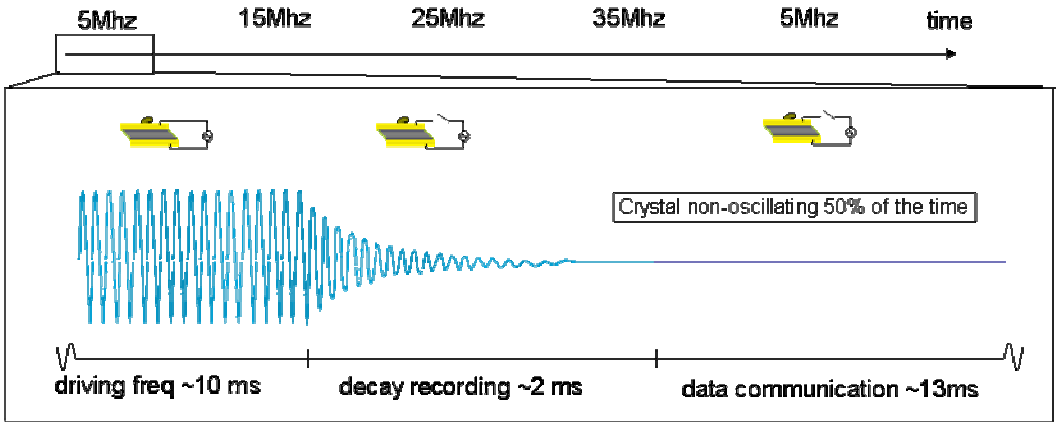

Figure 1.4 – Schematic of the time scales for frequency, dissipation, and data acquisition in the QCM-D technique across several different overtones (Illustration courtesy of Q-Sense).

Adsorbed mass on low-dissipation ($< 10^{-6}$) surfaces can be measured directly using the Sauerbrey relationship [129]:

$$\Delta m = \frac{-C\Delta f}{n} \tag{1.2}$$

where C is a constant, approximately 17.7 ng/(Hz*cm^2), Δf is the frequency shift, and n is the overtone number. However, for materials that exhibit high dissipation [130], a more sophisticated model must be used to incorporate the potential viscous damping effects seen during dissipation measurement cycles and to correctly determine the adsorbed mass [98].

The Voigt model applies a parallel spring-dashpot system to measure both viscous and elastic contributions to the quartz surface. In this system, the dissipation factor, given by:

$$D = \frac{1}{\pi f \tau} \tag{1.3}$$

where f is the frequency and τ is the decay time. In brief, the properties of the adsorbed layer are modeled with four parameters: density (ρ), shear modulus (μ), shear viscosity (η), and thickness (δ). The reader is directed to Voinova et al. and Höök et al. for a detailed mathematical overview of the model [131-132].

Raw frequency and dissipation data are typically least-squares curve fitted using supplied software to obtain the four Voigt parameters. To provide unique solutions to the equation, frequency and dissipation data from different overtones are applied to the fitting algorithm. The main assumptions to the Voigt model are that the frequency shift is negative, dissipation is positive, the adsorbed layers are in a no-slip condition, and that

the layers cover the surface uniformly [133]. For phase separated PEGylated surfaces, the assumption most likely to be violated is that the surface is covered with a uniform layer of protein. In this case, the reported mass will indicate sub-monolayer coverage of the protein being measured.

Another consideration for this technique is that because it is a gravimetric technique, water entrapped within an adsorbed protein layer or tightly coupled to certain macromolecular moieties will also contribute to the frequency and dissipation shifts [134]. As a result, mass and layer thickness readings obtained by QCM-D will often be higher than those observed for optical techniques such as surface plasmon resonance, ellipsometry, and optical wavelength laser spectroscopy [134-135]. Because of this, some researchers have instead proposed that QCM-D-measured density be referred to as the "effective density" [135] and may be more indicative of an actual situation in an aqueous or physiological environment. Additionally, coupled water that is lost during certain processes, such as in-situ crosslinking, can be measured using QCM-D [124-125].

1.10. Structure of the thesis

The thesis is divided into six chapters, including the introduction. The second chapter provides the materials and methods for the experiments performed. The third chapter covers manual synthesis and characterization of a small library of poly((I_2)DTE-*co*-PEG carbonate) polymers, as well as initial phase separation and protein adsorption studies. The fourth chapter describes the results of automated parallel synthesis of a larger library of poly(DTE-*co*-PEG carbonate), phase separation trends as a function of

PEG molecular weight and concentration, protein adsorption using differently sized protein probes, and an examination of physical polymer properties that may potentially modulate protein adsorption. The fifth chapter describes the effects of phase separation and polymer composition on a model cell system under physiological conditions. The sixth and final chapter summarizes the work performed, and presents conclusions and proposed future work that may be of interest.

2. Materials and Methods

2.1. Materials used

All solvents were used as received unless otherwise indicated. 1, 4-dioxane, methylene chloride (MeCl), trifluoroacetic acid (TFA), isopropanol (IPA), ethanol, and pyridine were purchased from Fisher Scientific Co (Pittsburgh, PA). Tetrahydrofuran (THF), N, N-dimethylformamide (DMF), and ammonium hydroxide were purchased from EMD Chemicals (Gibbstown, NJ). Dimethyl sulfoxide (DMSO), deuterated chloroform, and phosphate buffered saline (PBS), PBS powder, and bovine serum albumin (BSA) were obtained from Sigma-Aldrich (St. Louis, MO). 30% hydrogen peroxide and deuterium oxide (D_2O) were purchased from Acros Organics (Morris Plains, NJ) and kept out of direct contact with light whenever possible. Human fibrinogen was purchased from Calbiochem (LaJolla, CA). Gold quartz crystals (QSX 301, Q-Sense AB, Göteborg, Sweden) were used as received.

2.2. Polymer synthesis

2.2.1. Manual polymer synthesis

Desaminotyrosyl tyrosine ethyl ester (DTE) and di-iodo desaminotyrosyl-tyrosine ethyl ester (I_2DTE) monomers were prepared by Dr. Das Bolikal and Barry Cunningham using methods described previously [101, 136]. The synthesis of poly(DTE-*co*-PEG

carbonate) polymers was performed as previously described by Yu et al. [104]. Synthesis of poly(I_2DTE-co-PEG carbonate)s follows the same synthetic scheme. To eliminate potential hazards associated with working with gaseous phosgene, triphosgene (TP, Aldrich) was used instead. TP was dissolved in methylene chloride to make a 20% w/w solution and added dropwise using a peristaltic pump (Fluid Metering Inc., Syosset, NY) over three hours with continuous overhead stirring (Cole-Parmer, Vernon Hills, IL). Reactions were quenched with a 90:10 mix of THF: deionized (DI) water and poured into 5x volume of IPA. To accommodate the precipitation process, solvent was evaporated using a rotovap (Büchi AG, Flawil, Switzerland) to concentrate the polymer, which prevents "billowing" of the polymer upon pouring into IPA. Because of the tackiness of some of the highly PEGylated polymers, precipitation with grinding was not possible. Instead, the polymers were precipitated in isopropanol in a 5:1 ratio and centrifuged after each wash. Polymers were then frozen at -20 °C and lyophilized (Labconco Corp., Kansas City, MO). Residual solvents were measured with thermogravimetric analysis (TGA, TA Instruments, New Castle, DE). A volatiles level of less than 1% was considered acceptable. Additional vacuum drying was performed if volatiles were too high (vacuum oven: Fisher Scientific, pump: Edwards High Vacuum, Crawley, Sussex, England). A list of synthesized polymers is given in Table 2.1. Other polymers mentioned in the text not listed in Table 2.1 were previously synthesized by Dr. Das Bolikal.

Table 2.1 – Mol% and wt% of manually synthesized poly((I_2)DTE-*co*-PEG carbonate) polymers

(I_2)DTE-PEG mol%	PEG MW	PEG wt%
DTE-70	106*	40.9
DTE-10	1000	23.7
DTE-20	1000	41.2

DTE-40	1000	65.1
DTE-15	2000	49.7
DTE-30	2000	70.6
DTE-0.71	35000	41.2
I_2DTE-5	1000	7.93
I_2DTE-20	1000	29.0

*: named "PEG_{100}" for the remainder of the thesis.

2.2.2. Parallel polymer synthesis

Polymers were synthesized in a Chemspeed Accelerator SLT-100 (Chemspeed AG, Augst, Switzerland) using methods described previously [137]. A detailed methodology is given below.

2.2.2.1. Monomer preparation

DTE monomer was purified to increase yield and prevent premature termination of the polymerization reaction. The monomer was dissolved to make a 20% w/v solution in methylene chloride and stirred for 3 h. The solution was then vacuum-filtered with a sintered flask, re-dissolved to make a 33% w/v solution, and stirred for an additional two hours. A second vacuum filtration was performed and the monomer was vacuum dried for 24 hours at 40 °C.

2.2.2.2. Chemspeed Accelerator synthesis method

Polymers were synthesized using a Chemspeed Accelerator SLT-100 parallel synthesizer. Bulk solutions for each mer unit were prepared and completed with CH_2Cl_2 to the volumes described on Table 2.2.

Table 2.2 – Stock solutions prepared for automated parallel synthesis of a library of poly(DTE-*co*-PEG carbonate) polymers

Solution	Weight (g)	Pyridine added (g)	Total volume (mL)
DTE	18.5	12.9	100
PEG_{100}	1.94	4.24	25.0
PEG_{1k}	1.94	0.84	25.0
PEG_{2k}	1.94	0.73	25.0
PEG_{8k}	1.94	0.65	25.0
PEG_{20k}	1.94	0.63	25.0
PEG_{35k}	1.94	0.62	25.0
TP (PEG_{100})	5.92	n/a	25.0
TP (other PEGs)	7.96	n/a	75.0

A separate, more concentrated solution of TP was made exclusively for PEG_{100} because of the large amount of TP needed to achieve polymerization with a large number of hydroxyl groups. Pyridine was added to each solution in excess to form leach HCl formed during the reaction. All solutions were dried with 8-12 mesh 4A molecular sieves (Acros) prior to usage to remove as much water as possible. Table 2.3 describes the volumes used for each polymer set that were transferred for each polymer to obtain the proper stoichiometric proportions.

Table 2.3 – weight of PEG, triphosgene (TP), and pyridine (Py) added to each reaction during automated parallel synthesis for the poly(DTE-*co*-PEG carbonate) library

wt% PEG	PEG MW	PEG (mg)	DTE (mg)	TP (mg)	Py (mg)
20%	PEG_{100}	66.0	264	162	395
30%	PEG_{100}	99.0	231	187	458

40%	PEG_{100}	132	198	213	521
20%	PEG_{1k}	66.0	264	95.5	233
30%	PEG_{1k}	99.0	231	88.5	216
40%	PEG_{1k}	132	198	81.4	199
20%	PEG_{2k}	66.0	264	91.6	224
30%	PEG_{2k}	99.0	231	82.6	202
40%	PEG_{2k}	132	198	73.6	180
20%	PEG_{8k}	66.0	264	88.7	217
30%	PEG_{8k}	99.0	231	78.2	191
40%	PEG_{8k}	132	198	67.7	165
20%	PEG_{20k}	66.0	264	88.1	215
30%	PEG_{20k}	99.0	231	77.3	189
40%	PEG_{20k}	132	198	66.5	163
20%	PEG_{35k}	66.0	264	87.9	215
30%	PEG_{35k}	99.0	231	77.1	188
40%	PEG_{35k}	132	198	66.2	162

Each reaction was then diluted to 3.6 mL with a stock solution of CH_2Cl_2 and vortexed at 800 RPM for 5 minutes to cause complete mixing of the solutions. TP was then dispensed in the volumes specified in Table 2.3 for each reaction at a flow rate of 50 µl/min, with continuous vortexing at 800 RPM of the reactions for 45-60 mins. Reactions were quenched with 1.5 mL of a 6:4 THF:DI water solution.

Because of the extreme toxicity of phosgene [138], the following safety precautions were taken: 1) A phosgene detector (TLD-1 Toxic Gas Detector, Honeywell, Morristown, NJ) was placed inside the SLT-100 that would audibly sound if the phosgene level surpassed 100 ppb. 2) A phosgene hangtag (Morphix Technologies, Virginia Beach, VA) with a red chemical indicator and detection threshold of 900 ppb was placed on the outside surface of the SLT-100. 3) An open bottle of 8 mL stock solution of NH_4OH was placed in the SLT-100 to quench any possible gaseous phosgene that resulted from TP breakdown during the reaction process. 4) A large excess of 10% v/v triethylamine in ethanol was transferred to each vial of TP solution to quench any

remaining TP. 5) Before opening the hood of the SLT-100, a nearby chemical hood was opened completely to allow negative pressure from the hood to take in any possible phosgene breakdown products. All personnel were evacuated from the lab for 10 minutes.

2.2.2.3. Work up

Reacted polymer solutions were transferred to 20 mL scintillation vials (Wheaton Science Products, Millville, NJ) and precipitated with IPA. After shaking for ~10 mins, the IPA supernatant was decanted and the polymers were redissolved in THF and reprecipitated in DI water for additional purification and removal of pyridine hydrochloride and low molecular weight oligomers. After the second precipitation, polymers were frozen at -80 °C and lyophilized (Labconco).

2.3. Polymer characterization

2.3.1. Gel permeation chromatography (GPC)

7-10 mg of polymer were dissolved in DMF with 0.1% TFA. DMF with 0.1% TFA was used as a mobile phase (Waters 410 RI detector, Perkin Elmer, Waltham, MA) for GPC. A flow rate of 1 mL/min was used in gel columns with pore sizes ranging from $10^3 – 10^5$ Å (Varian Inc., Palo Alto, CA). Polystyrene standards were used a reference. Weight average molecular weight (M_w), number average molecular weight (M_n), and polydispersity (Pd) were measured by integrating peaks from the onset of the first peak to the end of the last peak.

2.3.2. Nuclear magnetic resonance (NMR)

10-15 mg of polymer was dissolved in 750 μL dimethylsulfoxide (DMSO, Acros) and transferred to an NMR tube. In instances where PEG was difficult to differentiate from water, chloroform was used instead. The tube was placed inside a 500 MHz NMR (Varian) until 32 counts were obtained. Peak assignments for each chemical group were described by Yu and coworkers [104] and can be seen in Figure 2.1. To calculate the amount of PEG present in each sample, the following calculations were used:

$$DTE_{norm} = \frac{DTE_{peak}}{DTE_{H}} \tag{2.1}$$

$$PEG_{norm} = \frac{PEG_{peak}}{\frac{PEG_{MW} * PEG_{H}}{PEG_{unit}}} \tag{2.2}$$

$$PEG_{wt\%} = \frac{PEG_{norm} * PEG_{MW}}{PEG_{norm} * PEG_{MW} + DTE_{norm} * DTE_{MW}} \tag{2.3}$$

where:

DTE_{peak} = the value of the NMR peak for the CH_2 part of the ethyl group at 4.1 ppm

DTE_H = the number of hydrogens in the CH_2 = 2,

DTE_{MW} = the MW of DTE ≈ 357,

PEG_{peak} = the value of the NMR peak for the CH_2CH_2 unit of PEG.

PEG_{MW} = the molecular weight of PEG

PEG_H = the number of hydrogens in a repeat unit of PEG = 4,

PEG_{unit} = the molecular weight of the CH_2CH_2O PEG repeat unit ≈ 44.

Sample NMR calculations are presented in the Appendix, Section 7.3.

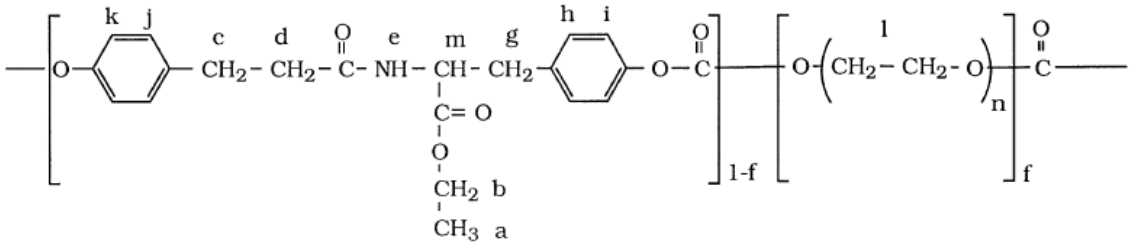

Hydrogen	Chemical shift (ppm)	Hydrogen	Chemical Shift (ppm)
a	1.17, 1.21, 1.24	b	4.08, 4.11, 4.15,4.18
d	2.48	m	4.85, 4.82
c	2.94	e	6.00
g	3.07	i/k/h/j	7.00/7.04/7.12/7.18
l (PEG)	3.64		

Figure 2.1 – Peak assignments DTE-PEG polymers in proton NMR. Figure reproduced from [104] with permission from Elsevier Limited.

2.3.3. Differential scanning calorimetry (DSC)

2-5 mg of material were weighed into an aluminum pan (Mettler Toledo, Columbus, OH), covered, and sealed. Samples were loaded into a DSC 2520 (Mettler Toledo) and analyzed using the following program:

1. Cool from room temperature to -50 °C
2. Heat from -50 °C to 150 °C at 10 °C/min
3. Isothermal for 5 minutes
4. Cool from 150 °C to -50 °C at 10 °C/min
5. Isothermal for 5 minutes
6. Heat from -50 °C to 150 °C at 5 °C/min

The program allowed for greater sensitivity in detecting possible melting points from high PEG concentrations. The second heating scan was performed at 5 °C/min to allow for better detection of multiple transitions that may occur from phase-separated systems. T_g was calculated from the intersection point of a horizontal line at half step height and the inflectional tangent, step-height being the change in the specific heat between the onset and endpoint of the glass relaxation (ASTM midpoint method).

2.3.4. Equilibrium water content (EWC) measurement

5 mm diameter discs were punched from 200 μm compression molded films and incubated in 5 mL PBS for several different time points – 3 hours, 6 hours, 24 hours, 48 hours, and 168 hours (1 week) at 37 °C. Discs were retrieved after incubation and dab-dried with a Kimwipe (Kimberly-Clark, Dallas, TX) to remove surface liquid. Samples were immediately run in a TGA to prevent moisture loss. Instrument temperature was ramped from room temperature to 350 ºC at 10 ºC/min. Equilibrium water content was measured using the following equation:

$$EWC = \frac{M_{wet} - M_{dry}}{M_{wet}} * 100\% \quad (2.4)$$

where M_{wet} is the mass of the sample at 23 ºC and M_{dry} is the mass at 150 ºC.

2.4. Sample preparation

In several instances, samples were prepared specifically to take advantage of various characterization techniques.

2.4.1. Compression molding

Kapton films were cut to the size of a custom-made mold and cleaned thoroughly with acetone and nitrogen air. 200 μm shims were placed at the end of each Kapton film to control film thickness. 500 mg of polymer were placed in between the two cleaned Kapton films and stacked in a pyramid shape to allow for dispersion upon pressing. For powder polymers, 500 mg powder was first cold-pressed into a tablet at 15000 lbf in a hydraulic press (Carver, Wabash, IN). Polymers were pressed at the glass transition temperature (T_g) + 50 °C using the following procedure:

1. Leave polymer at T_g + 50 °C and P = 0 for 5 minutes.
2. Ramp up to 15000 lbf gradually over 90 seconds.
3. Leave the polymer at 15000 lbf for 60 seconds.
4. Gradually release pressure from the press and remove the mold.

This procedure typically gave fault-free, uniform films. Additional polymers treatments, such as annealing or quenching, were performed at this time if necessary.

2.4.2. Spin-coating

All solvents used in spin coating were first dried using 4A sieves (Acros). Polymers were dissolved in a 1% w/v solution with 1,4-dioxane. When spin-coating onto glass cover slips, additional steps were taken to clean the cover slips. 15 mm diameter glass cover slips (Fisher) were first sonicated in ethanol for 1 hour, and then sprayed with

bulk isopropanol and dried with nitrogen. Prior to spin-coating, humidity was controlled by running drierite-treated air through a glove box containing the spin-coater. Humidity was at less than 10% relative humidity before spin-coating. Cover slips or gold quartz crystals were placed onto the vacuum chuck of the spin coater (Headway Research, Garland, TX) and centered. 50 μL polymer solution for gold quartz crystals, or 80 μL for glass cover slips, were pipetted onto the substrate to cover the entire surface. The spinner motor was immediately activated at 4000 RPM for 30 seconds. Coated cover slips or crystals were then placed in a vacuumed desiccator overnight. Spin coating results are described in Section 7.1.

2.4.3. Polymer fractionation

Polymers were dissolved in THF to make a 10% w/v solution. IPA was added dropwise until the solution became slightly turbid. Solutions were then centrifuged at 4 ºC at 2300 RPM for 20 minutes (Beckman Coulter, Brea, CA). The supernatant was decanted into another container, and the process of adding IPA and centrifuging was repeated three more times, resulting in four separate fractions. Fractions were then frozen and lyophilized to remove any residual solvent. Fractions were named in order of precipitation, i.e. F1 was the first fraction precipitated, F2 was the second, and so on. A large amount of IPA was added during precipitation of F4 to maximize yield of the material, and as a result, this fraction often contained oligomeric units. In instances where F1 yield was high (>250 mg), F1 was redissolved and fractionation was performed again

to yield four additional fractions. These fractions were named F1-1, F1-2, F1-3, and F1-4, and are referred to in the text as “subfractions”.

2.5. Atomic force microscopy (AFM)

Spin-coated glass cover slips were mounted on a metal disc using two-sided adhesive and placed in a magnetic sample holder in an AFM (Veeco Instruments, Woodbury, NY). A silicon probe (NanoAndMore, Lady’s Island, SC) was mounted in the probe holder and the probe tip was aligned with the feedback laser. The cantilever was tuned and the peak offset by 5%. Integral and proportional gains were adjusted until proper sample tracking was achieved, and 20 μm x 20 μm fields were scanned. Large irregularities, such as dust particles and streaks, were omitted from the measurements.

2.6. Protein surface characterization – quartz crystal microbalance with dissipation (QCM-D)

Polymer solutions were spin-coated onto gold quartz crystals (QSX301, Q-Sense AB, Göteborg, Sweden) as described in Section 2.4.2. Coated crystals were mounted into stainless steel flow modules in a Q-Sense E4 system. The temperature for the modules, buffer, and protein solution aliquots was set at 37 ºC. Frequency sweeps were performed to determine the resonant frequencies for each crystal. PBS was then flowed through the system at a flow rate of 0.17 mL/min until liquid reached the chambers, evidenced by a sharp decrease in frequency and increase in dissipation. The resonant frequency was

found again after exposure to liquid, and frequency and dissipation readings were allowed to equilibrate. After a stable baseline was achieved ($\Delta f < -1$ Hz per 10 mins, $\Delta D < 1E-6$ per 10 mins), 3 mg/mL protein solutions of either fibrinogen or BSA were introduced for 1 hour. After adsorption for 1 hour, PBS was flowed through the system again for 1 hour to remove any irreversibly adsorbed protein.

2.6.1. QCM-D modeling

Raw QCM-D data was modeled using provided software (Q-Tools, Q-Sense AB). Modeling limits were set between the endpoint of the equilibration step and the end of the PBS rinsing step. For samples with low dissipation ($\Delta D < 2E-6$), the Sauerbrey relationship [129] was used as an acceptable approximation to determine the adsorbed mass.

$$\Delta m = -\frac{C\Delta f}{n} \tag{2.5}$$

This relationship is simply a linear relationship between frequency shift and adsorbed mass, where C = 17.7 ng/(Hz-cm^2) and n = the overtone number. It has been reported that for low dissipations, the adsorbed mass can be determined accurately with the Sauerbrey relationship [130]. When dissipation is high, the Sauerbrey relationship underestimates the actual mass, and is no longer applicable [98, 130]. In these cases, the Voigt model was used.

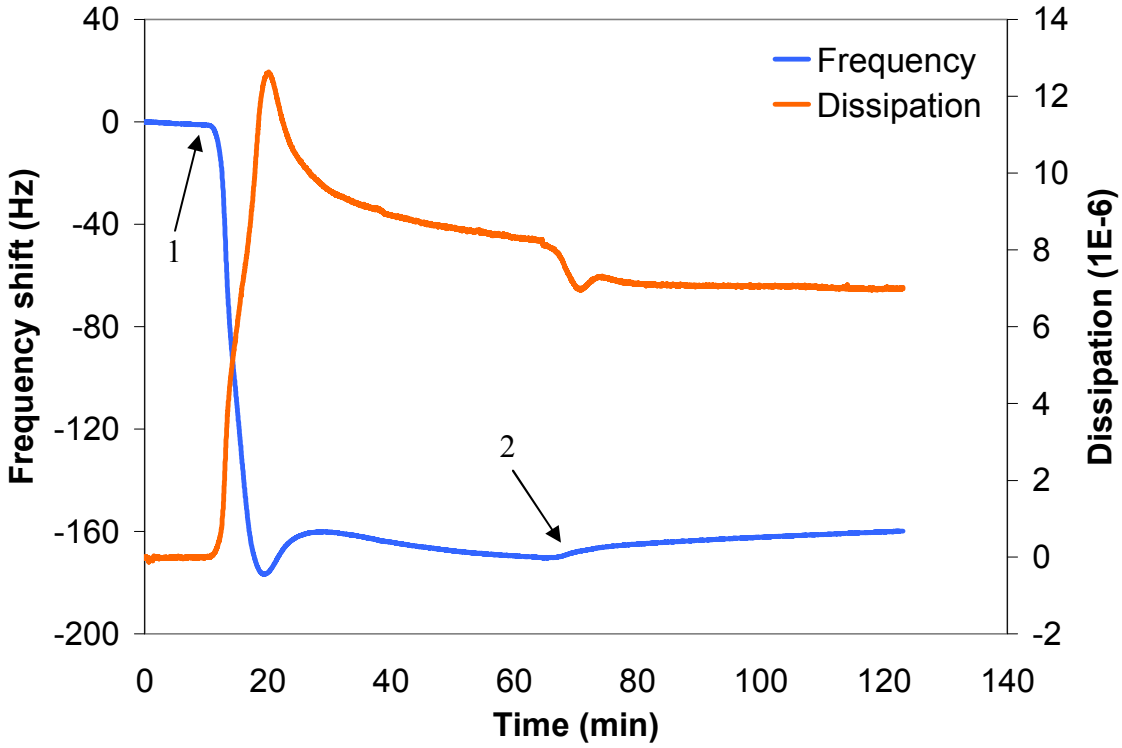

Figure 2.2 – A sample QCM-D graph with frequency (blue line) and dissipation (orange line) of the 3rd overtone shown. Modeling limits were set from point 1 (onset of protein adsorption) to point 2 (end of rinsing step).

Overtones 3, 5, and 7 were selected when possible for the modeling of the raw QCM-D data. Overtone 9 was substituted when overtones 3, 5, or 7 were excessively noisy or deviant. Fluid density, viscosity, and layer density were fixed at 1000 kg/m^3, 0.001 kg/m-s, and 1200 kg/m^3, respectively, as determined previously by Weber et al. for a similar polymer/protein system [98]. Layer viscosity, shear, and thickness limits were set to 10^{-5} – 10^{-2} kg/m-s, 10^4 – 10^7 Pa, and 10^{-10} – 10^{-7} m, respectively, as the curve-fitting parameters. The layer thickness value obtained from the Voigt model was converted to adsorbed mass per area by the equation:

$$m = \delta\rho \tag{2.6}$$

which is reported in ng/cm^2 or μg/cm^2. A minimum of n=3 was obtained for each sample. Significance was determined by a two-tail student's t-test at a p value of <0.05.

2.6.2. Cleaning procedure

After use, the QCM-D system was cleaned at high flow rates (2.5 mL/min) with 50 mL of deionized (DI) water, followed by 50 mL of 1% v/v Tween-20 solution (Sigma-Aldrich), and followed by 100 mL DI water. Chambers were dried with nitrogen to remove residual water, and the quartz crystals were removed. Crystals were then soaked in THF to remove polymer coatings, and then placed in a 1:1:5 solution of ammonium hydroxide, hydrogen peroxide, and DI water at 80 ºC for 10 minutes. Crystals were rinsed off with DI water, dried with nitrogen, and placed in a UV/ozone chamber (Jelight Company, Irvine, CA) for 10 minutes before reuse.

2.7. Small angle neutron scattering (SANS)

11 mm discs were punched from 200 μm compression molded polymer films. Deuterated PBS (DPBS) was made by reconstituting PBS powder with an appropriate amount of deuterium oxide (D_2O). The polymer samples were incubated in 10 mL DPBS for specified amounts of time or until their EWC was reached. Samples were then placed into quartz chambers and filled with a few drops of DPBS. Temperature was varied between 23 ºC, 37 ºC, and 60 ºC for certain samples to examine temperature effects on bulk morphology.

SANS data were collected at the spallation sources (Argonne National Laboratory, Chicago, IL) using the small angle neutron diffractometer (SAND) instrument over a q range from 0.004 to 1 $Å^{-1}$ (q is the scattering vector; $q = 2\pi/d$, where is d is the Bragg spacing), the low-Q diffractometer (LQD) from Los Alamos National (Los Alamos, NM) laboratories (q = 0.003 $Å^{-1}$ - 0.5 $Å^{-1}$), and at the HFIR's SANS3 beam line at the Oak Ridge National Laboratories (ORNL, Oak Ridge, TN) using 6.5 m (q = 0.006 to 0.135 $Å^{-1}$) and 14.5 m (q = 0.003 to 0.06 $Å^{-1}$) sample-to-detector distances.

2.7.1. SANS data analysis

The isotropic 2D-data were reduced to 1D I(q) vs. q plots, where I(q) was the radially averaged intensity at each value of q. Scattering from PGA was used to calculate the spacing between the D_2O-rich interlamellar regions, and the area of the interference peak. The peak was fitted to a Gaussian,

$$I(q) = (aq + b) + I_0 e^{-(\ln 2)\left\{\frac{2(q-q_0)}{w}\right\}^2} \quad (2.7)$$

where a and b are the slope and intercept, respectively, of a baseline under the curve, I_0 is the maximum intensity, measured perpendicular to the baseline, q_0 is the position of I_0, and w is the full-width at half-maximum. The a and b values were determined by using the SLOPE and INTERCEPT functions, respectively, at the onset and endset of the peak. I_0 and q_0 were then curve-fitted in Microsoft Excel (Microsoft Corp., Redmond, WA) using the Solver add-in function.

Data from PDLLA, PLA and PLGA were analyzed as fractals [116], using the slope of the log(q) vs. log(I(q)) curve to determine the fractal dimensions. A slope of ~3 indicates a mass fractal, while a slope ~4 indicates a surface fractal. Trends for the data are described in Chapter 3.

Raw SANS data from DTE-PEG polymers was modeled using the Zernicke-Prins (Z-P) approximation [118], which assumes that scattering domains are spherical. The equation is given as:

$$I(q) = B + I_0 \left\{ \frac{\left(\sin(qR) - qR\cos(qR)\right)}{(qR)^3} \right\}^2 \left\{ \frac{1 - A^2}{1 - 2A\cos(qd) + A^2} \right\} \tag{2.8}$$

where:

$$A = \exp\left(\frac{1}{2} q^2 \sigma^2 \right) \tag{2.9}$$

I_0 = initial intensity

q = scattering vector

R = radius of scattering bodies

d = center-to-center distance between scattering bodies

σ = the spread in d (lower value indicates more uniformity in distances, and vice versa)

and,

$$B = I_{CDS} \exp\left(-q^2 \frac{R_g^2}{3} \right) \tag{2.10}$$

where:

I_{CDS} = central diffuse scattering intensity, referred to in the remainder of the text as zero-angle scattering

R_g = radius of gyration

The B term is a modification of the Z-P equation that helps to model the possible existence of a central diffuse curve, i.e. large I(q) values at low q values. This event typically occurs when scattering bodies physically merge during a phase separation event. In most cases, the B value was close to 0. The data was curve-fitted using the Solver add-in for Excel (Microsoft) using a trial-and-error approach until a best fit was achieved, i.e. when R^2 was maximized.

The fitting parameters and their relationship to the scattering bodies are shown in Figure 2.3**Error! Reference source not found.**. In this model, σ is a measure of the short-term order of the scattering domains, but does not denote any statistical chance of the location between scattering bodies. To reduce confusion, and to also normalize σ to the d-spacing, the value σ/d, termed the "fractional deviation," can be calculated. This value effectively expresses the minimum and maximum possible center-to-center distance between scattering bodies as a percentage above and below the calculated d-spacing.

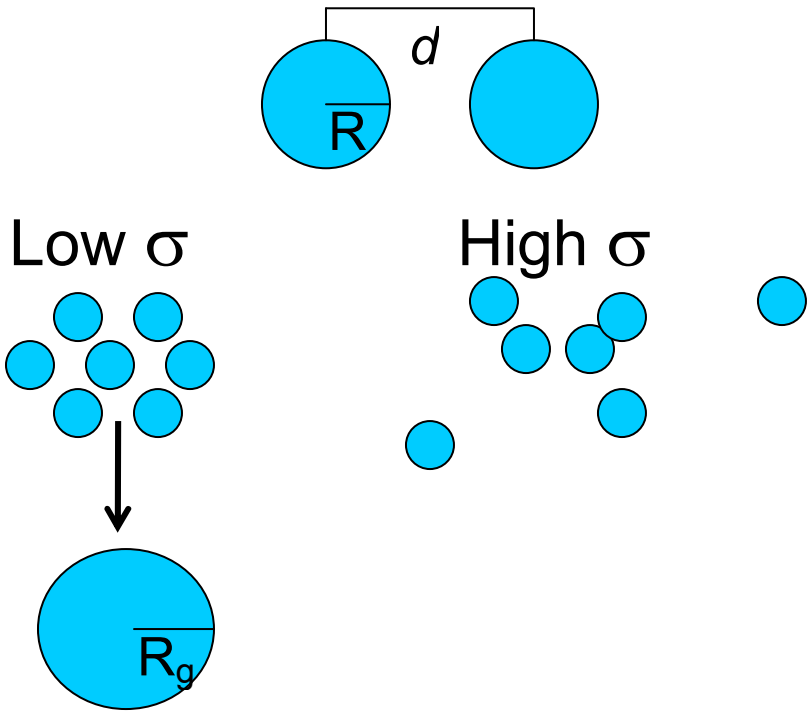

Figure 2.3 – Schematic that illustrates the parameters described by the Z-P model. Hydrated clusters are described as spheres, with a radius R, center-to-center distance d, and short range ordering of σ. In instances of zero-angle scattering, the size of large, merged clusters are described by the radius of gyration, R_g.

In some samples, a high intensity signal may be obtained at low *q* values in addition to a regular scattering peak. This signal is typically the result of several scattering bodies merging together to form a larger body, and is described by the second term in the equation. The value R_g describes the size of the merged cluster.

2.8. Contact angle measurements

Contact angle hysteresis has been described as a method for detecting micro- and nanofeatures, [139], and can be calculated from the difference between the advancing and receding contact angles:

$$Hysteresis = \theta_a - \theta_r \tag{2.11}$$

Polymers were spin-coated onto glass cover slips as described previously, and cleaned off with nitrogen to remove any potential contaminants from the surface. DI water was filtered twice through 0.45 μm Whatman filter to remove particulates and placed into a syringe. A goniometer (Ramé-Hart, Mountain Lakes, NJ), was used to measure this angle, with the leading edge of the water drop lined up tangentially with the reader and the base horizontal line aligned with the contacting surface between the water drop and the substrate. A single drop was dripped onto the surface of the cover slip, with the needle still contained within the drop. The angle measured for the drop in this situation is known as the advancing contact angle, θ_a. The water droplet was then retracted until the syringe separated from the drop, and the receding contact angle, θ_d was measured. Both sides of four separate drops were measured, giving a total of n=8 measurements.

Surface energy measurements were performed to obtain additional information about surface properties. Three probe liquids, water, glycerol, and diethylene glycol, were used to determine the surface free energy [140-141]. During changeover of probe liquids, the syringe and all contacting parts were flushed out with copious amounts of DI water and dried with nitrogen. The probe liquid was then used to "rinse" the syringe and needle three times to ensure that the concentration of liquid present was primarily the probe liquid used to measure the surface. Eight replicates of each probe liquid were measured, as described above.

The surface energy was calculated using the Fowkes approximation [140, 142]:

$$\left[\frac{1+\cos\theta}{2}\right]\times\left[\frac{\gamma_l}{\sqrt{\gamma_l^d}}\right] = \sqrt{\gamma_s^p}\times\sqrt{\frac{\gamma_l^p}{\gamma_l^d}} + \sqrt{\gamma_s^d} \tag{2.12}$$

where γ_l is the total liquid surface tension, γ_l^d is the dispersive component of the liquid, γ_l^p is the polar component of the liquid, γ_s^p is the polar component of the surface, and γ_s^d is the dispersive component of the surface. The value of θ is determined by the contact angle, while γ_l and γ_l^p are known values as given in Table 2.4.

Table 2.4 – Dispersive, polar, and total surface tension values for water, glycerol, and diethylene glycol (DEG). Values obtained from [141]. All values have units in mJ/m^2.

	γ_l^d	γ_l^p	γ_l
water	21.8	51.0	72.8
glycerol	34.0	30.0	64.0
DEG	31.7	12.7	44.4

After applying the contact angle, γ_l, and γ_l^d values, it becomes evident that equation (2.12) follows the form $y = mx + b$, where $m = (\gamma_s^p)^{1/2}$ and $b = (\gamma_s^d)^{1/2}$. By plotting x vs. y for the three probe liquids, m and b can be determined by drawing a least-squares linear trendline between the three points. The total surface free energy, γ_s can then be found by adding m^2 and b^2, i.e. γ_s^p and γ_s^d.

$$\gamma_s = \gamma_s^p + \gamma_s^d \tag{2.13}$$

2.9. Cell studies

2.9.1. Cell population and spreading

SaOS-2 cells (ATCC, Manassas, VA) were propagated in F12H (Invitrogen, Carlsbad, CA) supplemented with L-glutamine, penicillin-streptomycin, and 10% fetal bovine serum (Sigma). Cell nuclei were stained with Hoechst 3328 (Molecular Probes

Inc., Eugene, OR), and cells were imaged using both fluorescence and phase-contrast modes at 24 hours post seeding. Cell population was assessed by counting the number of Hoechst-positive nuclei in a random image field per a replicate with 4 replicates of each substrate type (n=4). Cell spreading was analyzed by measuring cell areas of 16 individual cells on 4 replicates of each substrate type (n=16) using Image J (NIH, Bethesda, MD).

2.9.2. Apoptosis measurement – nuclear translocation of GFP-GAPDH:

At 24 hours post seeding, the nuclear and cytoplasmic distributions of endogenous GFP-GAPDH in SaOS-2 cells were analyzed quantitatively following previously published methods [143-145]. Briefly, cells nuclei were stained using Hoechst 3328 (Molecular Probes) and imaged at 60x using a fluorescent multiphoton microscope (Leica Microsystems, Wetzlar, Germany). The average green fluorescence in the nucleus and cytoplasm was determined after subtracting the background. Apoptotic activity was determined by dividing the nuclear fluorescence intensity by the cytoplasmic intensity, with a higher ratio indicating more apoptotic activity. Images were analyzed using ImageJ (NIH). Each experiment consisted of analyzing 16 individual cells on 4 replicates of each substrate type (n=16).

2.9.3. Integrin α5 expression and intracellular distribution

The protein expression of integrin α5 was assessed by immunocytochemistry and image analysis. Samples were fixed with 2% paraformaldehyde (PFA, Sigma), blocked and permeabilized with 5% horse serum (Sigma) and 0.1% triton x-100 (Sigma), incubated with a 1:50 dilution of monoclonal mouse anti-human integrin α5 antibody (R&D Systems, Minneapolis, MN), and then incubated with a 1:100 dilution of Alexafluor 594-conjugated goat anti-mouse secondary antibody (Invitrogen). Cells were counterstained with Hoechst 3328 (Molecular Probes) and fluorescein isothiocyanate (FITC)-phalloidin (Sigma) to identify cell number and cell area. Cells were then imaged by fluorescence microscopy (Carl Zeiss Inc., Thornwood, NY). Both fluorescence signals from integrin α5 proteins and cell areas were measured from image fields using ImageJ (NIH). The fluorescence signals from single cells were normalized to the corresponding cell areas. Twenty-five individual cells on 5 replicates of each substrate type were examined (n=25). Intracellular distribution of integrin α5 proteins was assessed by imaging GFP signals from GFP-integrin α5-transfected cells.

2.9.4. Fluorescence in-situ hybridization (FISH)

mRNA expression of integrin α5 was assessed by in situ hybridization and image analysis. Cells were fixed using 2% PFA in PBS, washed with xylene (Sigma), and rehydrated with 100 % ethanol. A fish sperm DNA FITC-conjugated mRNA probe (56FAM/CAGCTATGGCGTCCCACTGTG) was custom-made (Exiqon, Vedbaek, Denmark). Cell were incubated with the probes (250 ng/μL) for 16 hours and washed with 60% formamide, NaCl, and sodium citrate. Cell nuclei were counterstained with a

ToPro-3 dye (Molecular Probes) and imaged. Both fluorescence signals from integrin α5 mRNA probes and cell areas were measured from image fields using ImageJ (NIH). The fluorescence signals from single cells were normalized to the corresponding cell areas. Eight individual cells on 3 replicates of each substrate type were examined (n=8).

2.9.5. Quantitative polymerase chain reaction (QPCR)

Polymers were spin-coated onto 15 mm glass coverslips as described in Section 2.4.2. 50,000 SaOS-2 cells were seeded onto. After 4 hours, non-adherent cells were washed out and RNA was either harvested immediately or cells were allowed to culture for 20 additional hours prior to harvest of RNA (Promega, Madison, WI) and synthesis of cDNA (Qiagen Valencia, CA). Quantitative PCR was conducted on the cDNA using the Roche 480 LightCycler, utilizing SYBR-green detection dye (Roche Applied Sciences, Indianapolis, IN). Expression of integrin α5 was held relative to GAPDH expression levels to calculate ΔΔCp.

3. Manual synthesis and characterization of poly(DTE-*co*-PEG carbonate) polymers

Based on the manuscript: "Study of nanoscale hydration modes in current and prospective biomaterials using small-angle neutron scattering", by Arnold Luk, N. Sanjeeva Murthy, Wenjie Wang, and Joachim Kohn, in preparation.

3.1. Background

The main purpose of this chapter is to determine whether phase separation can occur at a quantifiable length scale in a focused set of random multiblock poly(DTE-*co*-PEG carbonate)s. SANS was used to identify potential phase separation at the nanoscale, and these results were correlated with protein adsorption studies to determine possible relationships between spatial characteristics protein adsorption capabilities of a polymer. The SANS studies on potential phase separation may also provide insight into modes of hydration and subsequent degradation of hydrophobic/hydrophilic systems. A study by Sousa et al. had previously reported that over the course of 12 months, poly(DTE-*co*-8 mol% PEG_{1k} carbonate) exhibits preferential degradation and erosion of PEG-rich regions in the form of hollowed channels [146]. Other previous studies have shown that degradation products in PEG-containing polymers tend to be PEG-rich, showing that preferential degradation of PEG segments can be extended to several polymer systems [147-148]. Though extensive research into polymer degradation and erosion are outside of the scope of this thesis, spatial features deduced from the SANS studies presented in this chapter may correlate with the channel sizes observed in their study and elucidate

morphological changes that may occur between short-term hydration and eventual erosion.

Several poly(DTE-*co*-PEG carbonate) polymer compositions previously synthesized by Yu et al. [104] were replicated for this study, with polymers extending to poly(DTE-*co*-40 mol% PEG carbonate). Polymers with even more PEG were reported to be water soluble [104], making their biological substrate properties difficult to study. To investigate how PEG molecular weight affects phase separation, three polymers with identical weight percentages of PEG and different PEG molecular weights were also analyzed: poly(DTE-*co*-70 mol% PEG_{100} carbonate), poly(DTE-*co*-20 mol% PEG_{1k} carbonate) and poly(DTE-*co*-0.71 mol% PEG_{35k} carbonate). Poly(DTE-*co*-PEG carbonate)s with PEG contents ranging from 0-10 mol% PEG_{1k} have been previously investigated to examine fibronectin adsorption, fibroblast motility, and cellular mechanics as a function of increasing PEG [77, 149]. Additionally, poly(I_2DTE-*co*-PEG carbonate)s were studied, as they are promising candidates for biodegradable vascular stents [98]. Examination of an iodinated set of polymers also provides valuable insight into how phase separation may be affected by a stiffer backbone mer.

To examine how increased mobility affects phase separation, SANS was performed while varying temperature dynamically from 23 ºC to 37 ºC to 60 ºC and back to 23 ºC. Such studies could provide perspective on phase behavior during processes such as sterilization and subsequent shelf storage. Finally, commonly used biomaterials, poly(lactic acid) (PLA), poly(glycolic acid) (PGA), poly(lactic-*co*-glycolic acid) (PLGA), and poly(D-L-lactic acid) (PDLLA) were also obtained and studied to draw comparisons

between different copolymers systems, semicrystalline polymers, and the poly(DTE-*co*-PEG carbonate)s.

3.2. Results

3.2.1. General polymer properties

For brevity, poly((I_2)DTE-*co*-PEG carbonate) polymers will be simply referred to as (I_2)DTE-PEG polymers for the remainder of the thesis. Weight % PEG will be used to describe polymers to improve comparisons between materials with different PEG molecular weights. Specific (I_2)DTE-PEG polymers will be described in this chapter as ((I_2)DTE wt%-PEG_{MW}), e.g. DTE-41%-PEG_{1k} = poly(DTE-*co*-41wt% PEG_{1k} carbonate).

Relevant characteristics of the polymers used in this work are given in Table 3.1. The mol % PEG is provided for reference. Increases in PEG weight % increase the water content and decrease the T_g, consistent with previous results [98, 104]. At lower PEG compositions the water content equilibrates to a low value over a long period of time [104]. As PEG content increases, polymers become increasingly soft and hydrogel-like, and higher levels of equilibrium water contents is reached at a faster rate. Interestingly, DTE-65% PEG_{1k} was water-soluble, while DTE-70% PEG_{2k} was not. DTE-65% PEG_{1k} was therefore not investigated further. PGA and PLA were both semicrystalline as confirmed by their melting peaks (223 and 169 ºC, for PGA and PLA respectively). PDLLA and PLGA were both amorphous.

Table 3.1 – Material properties of polymers examined with SANS

Sample composition with x mol% PEG	Weight % PEG	T_g (°C)	M_w (kDa)	EWC (wt. %)
DTE- x% PEG_{nk}				
DTE 0 % PEG	n/a	96		3.0
DTE-5% PEG_{1k}	12.8	63	198	5.3
DTE-10% PEG_{1k}	23.7	39	186	13
DTE-20% PEG_{1k}	41.2	4.3	75	42
DTE-15% PEG_{2k}	49.7	-18	140	63
DTE-30% PEG_{2k}	70.6	-46	226	85
DTE-0.71% PEG_{35k}	41.2	-5.7	185	56
I_2DTE- x% PEG_{nk}				
I_2DTE 0% PEG	n/a	140	219	1.5
I_2DTE-5% PEG_{1k}	7.93	81	57	2.7
I_2DTE-20% PEG_{1k}	29.0	8.9	45	19
I_2DTE-15% PEG_{2k}	36.6	4.2	113	29
I_2DTE-30% PEG_{2k}	58.4	-31	129	62
poly(glycolic acid)	n/a	46, 220*	n/a	27
poly(lactic acid)	n/a	57, 170*		0.0
poly(D, L-lactic acid)	n/a	42		43
poly(lactic-co-glycolic acid)	n/a	44	95	33

Table 3.2 describes the water uptake characteristics of PGA, PLA, PDLLA, and PLGA as a function of time. These four polymers were tested until 28 days, a length of time over which significant degradation occurs in the amorphous PDLLA and PLGA polymers [150]. PLA showed no water uptake during the 28 day incubation period,

consistent with previous literature [151-152], PGA, PDLLA, and PLGA all showed a large increase in water uptake at one point during the incubation process. For PGA and PDLLA, this occurred after 14 days, while for PLGA, it occurred after 21 days. The sudden jump in water uptake suggests that significant morphological changes occurred that allowed water to infiltrate the samples. The surges in water uptake for PGA, PDLLA, and PLGA also correspond to the onset of degradation as reported in the literature [150, 153]. In this sense, the sudden influx of water may be caused by additional free volume and end groups that may be initiated by degradation [154]. The correlation between these changes and scattering data is addressed in the following sections.

Table 3.2 – % water uptake of PGA, PLA, PDLLA, and PLGA as a function of incubation time

Sample	7 day	14 day	21 day	28 day
poly(glycolic acid)	3.30	21.2	27.7	27.2
poly(lactic acid)	0.00	0.00	0.00	0.00
poly(D,L-lactic acid)	1.87	35.5	39.9	43.3
poly(lactic-*co*-glycolic acid)	0.81	1.04	29.9	32.8

Polymers are discussed based on their general morphological characteristics in the following sections. Semicrystalline polymers will be discussed first, followed by amorphous homopolymers, and amorphous, PEG-containing copolymers will be discussed last. These results will highlight the differences in the distribution of water, and hence degradation behavior, in these three classes of polymers.

3.2.2. Scattering from PGA and PLA

Scattering curves from PGA show a peak at 0.062 $Å^{-1}$ (d = 102 Å) even in the dry state (Figure 3.1). This is due to the inherent contrast between the amorphous and crystalline regions in the lamellar structure of this polymer, and its distance is close to the 132 Å reported in the literature [155]. As the amount of water absorbed by the polymer increases, at intermediate EWCs, scattering intensity decreases, as evidenced by a large decrease in the area under the scattering peak. Upon further hydration, the scattering peak becomes more intense compared to the dry sample. This sequence of events is due to the preferential diffusion of water in semicrystalline polymers into amorphous regions in both the interlamellar regions and to regions outside the crystalline lamellar stacks, but only the former contributes to the SANS peak [156-158]. The decrease in intensity at 3-20% water-uptake is due to contrast matching between the hydrated amorphous regions and the crystalline regions. The reduction in domain spacing at larger EWC that corresponds to longer times of immersion in water is likely due to hydrolytic degradation of the polymers. GPC could not be done to confirm this because the polymer was not soluble in either THF or DMF, even after intermediate dissolution in hexafluoroisopropanol (HFIP).

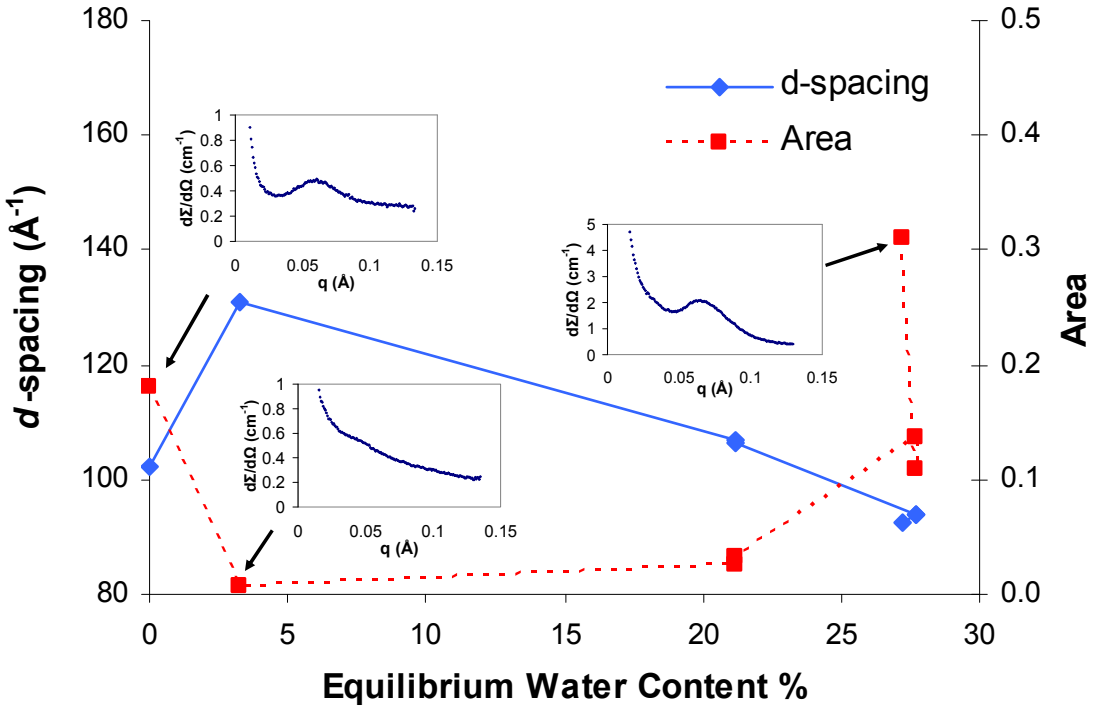

Figure 3.1 – PGA *d*-spacing and area vs. water uptake – insets: *q* vs. intensity graphs of selected points. A scattering peak is visible for the dry PGA sample due to its semicrystalline properties. The reduced scattering peak seen at ~4% EWC is due to coincidental contrast matching between the lamellar scattering intensity and D_2O.

Water uptake in PLA, and hence the scattering, was negligible. Although PLA is semicrystalline like PGA, the hydrophobicity of PLA makes even the less densely packed amorphous domains in PLA impermeable to water. Because very little water infiltrates in the sample, trends and correlations between water uptake and scattering behavior could not be determined. The ratio of D to L in the PLA that could not be obtained from the suppliers, but by comparing the large melting peak and the lack of water uptake to that observed in PDLLA, a large majority (~90-95%) of the polymer appears to contain mostly the L isomer.

3.2.3. Scattering from PDLLA, PLGA

Figure 3.2 shows the evolution of the Porod slope as a function of water uptake for PDLLA. The scattering from PDLLA (Figure 3.2, inset), unlike PGA, has no interference peak, indicating a lack of organized hydration clusters. The linearity over one decade of q in the log I(q) vs. log q plot is indicative of a fractal distribution of water in the polymer matrix [116]. Figure 3.2 shows the evolution of the logarithmic slope as a function of water uptake for PDLLA. After hydration for 7 days, the fractal dimension increases from 1.5 to almost 4, indicating a change in the hydration structure from a mass fractal to a surface fractal and finally to a smooth interface between the hydrated domains and the surrounding matrix. The increase in fractal dimension is also accompanied by a corresponding increase in SANS intensity (data not shown). Despite a large increase in the water uptake over several more weeks, the changes in the fractal dimensions are small. The inflection of the slope at water uptake of 36 % corresponds to the sample that was incubated for 21 days, the approximate time when the polymer begins to show signs of degradation [150].

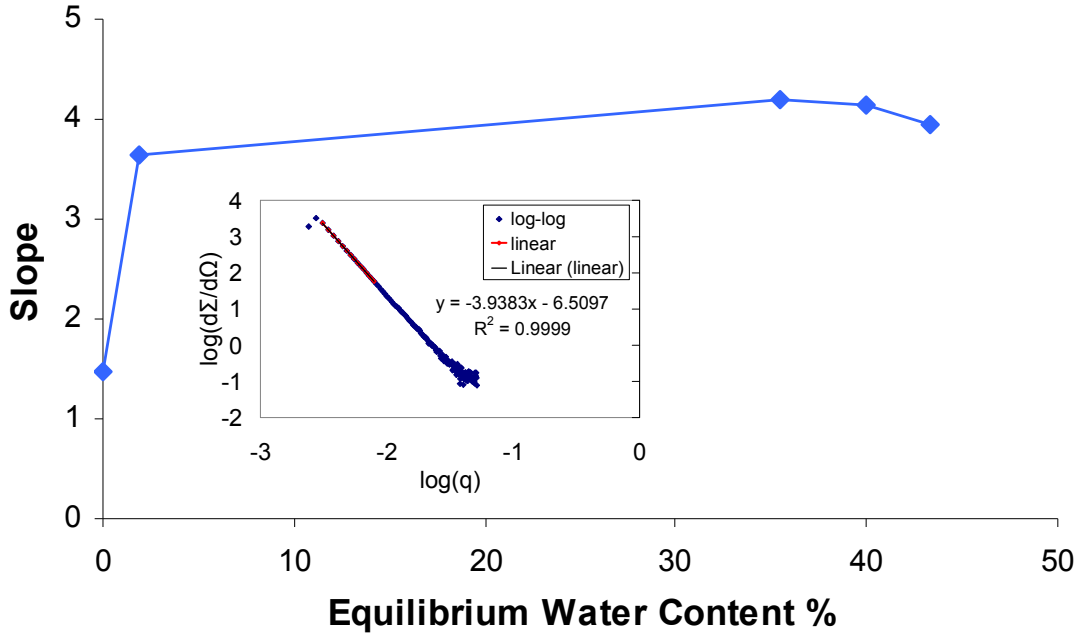

Figure 3.2 – PDLLA slope vs. water uptake: inset – sample fractal plot showing the fitted linear portion of the log-log 1-D data. Fractal analysis shows that an inflection point in the slope (21 days, 40% EWC) occurs at approximately the same time as the reported degradation of PDLLA

Figure 3.3 shows that an increase in temperature can also increase the fractal dimension of PDLLA similar to that observed with increased water uptake. This increase in fractal dimension is more pronounced in the less hydrated 7-day samples than in more thoroughly hydrated 21-day samples. From these results, it appears that sufficiently hydrated samples reach a "plateau" in fractal dimension, but that additional heating can increase the fractal dimension of a material that has not yet achieved its EWC. PLGA shows a behavior similar to that of PDLLA with the fractal dimension increasing from 3.5 to 4 from low to high water uptake (Figure 3.4).

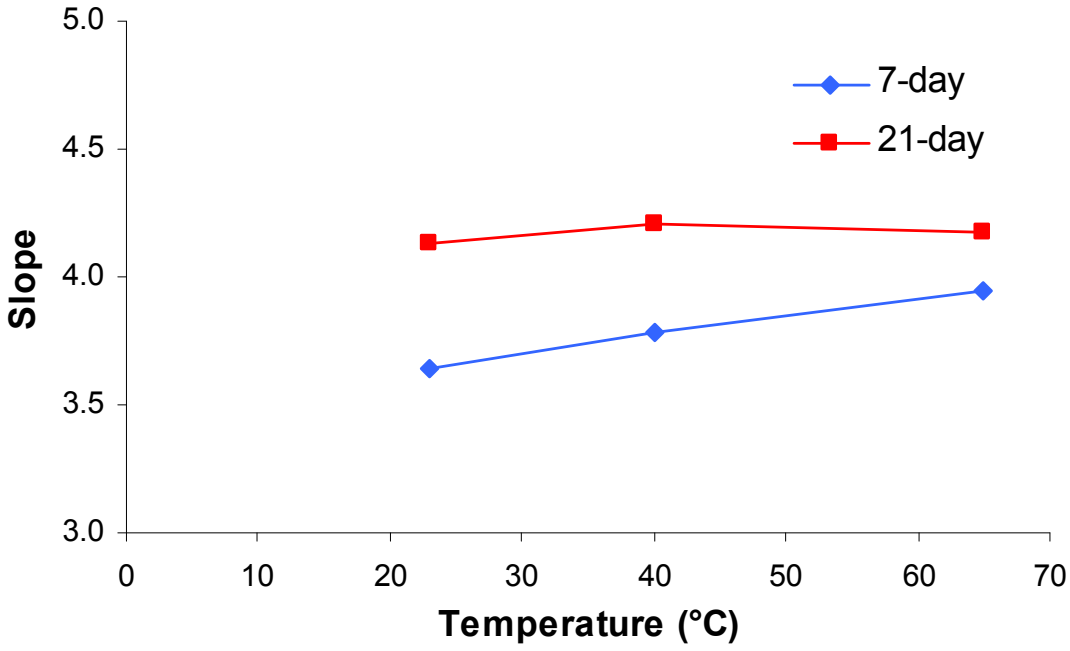

Figure 3.3 – PDLLA slope and intercept vs. temperature for 7 and 21 day incubation. Temperature scans for 7 day incubated samples show an increase in fractal dimensions, while 21 day incubated samples remain relatively constant.

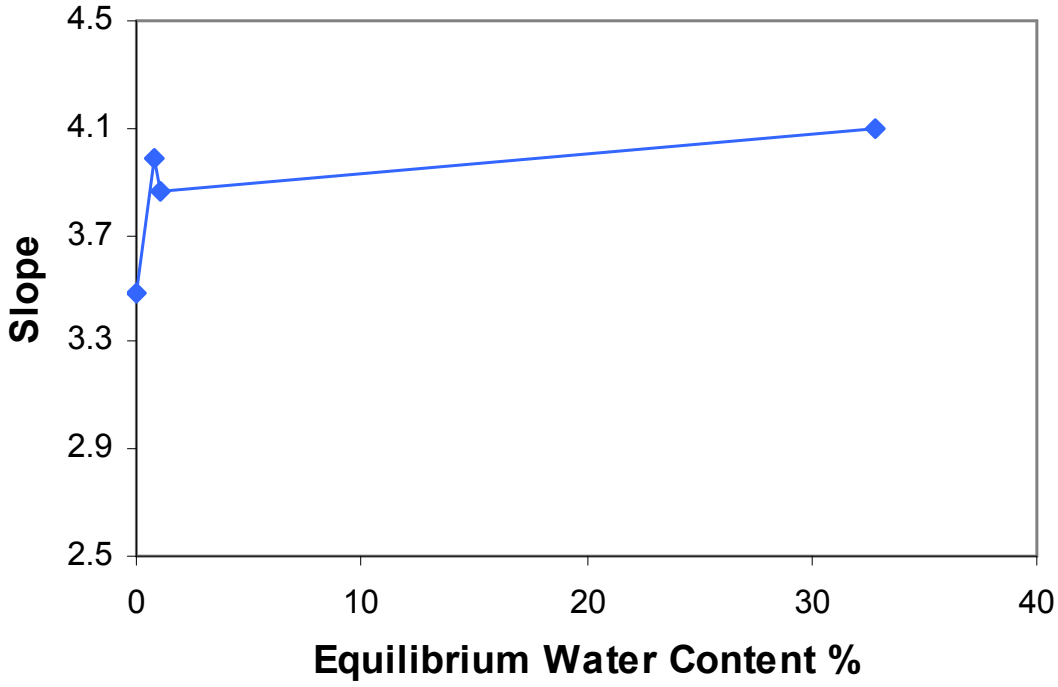

Figure 3.4 – PLGA slope vs. water uptake. Behavior is identical to that of PDLLA.

3.2.4. Scattering in DTE-PEG polymers:

Representative examples of the SANS data for DTE-PEG polymers are shown in Figure 3.5. Figure 3.5a shows a sample scan of a polymer that contains no scattering peak. The absence of a scattering peak in certain polymer compositions suggests that water is homogeneously distributed throughout the bulk of the polymer. The scattering peaks seen clearly in Figure 3.5b and Figure 3.5c at $q \sim 0.03$ Å^{-1} indicate the formation of hydrated, segregated clusters. Additionally, Figure 3.5c also shows the presence of central diffuse scattering, which suggests the existence of large, merged hydrated clusters. The graphs also illustrate the good agreement between the observed SANS curve and the Z-P model, indicating that this model is adequate for parameterizing the scattering curves despite its relatively simplistic nature. The three fit parameters from the Z-P model, radius of the scattering domains (*r*), the separation between the domains (*d*), and fractional deviation (f_d, a measure of the distribution in *d*-spacings), are shown in Table 3.3 – Table 3.6. Also shown is the fourth parameter, the radius A of the large isolated domains of water that are present in some of the samples (Figure 3.5c).

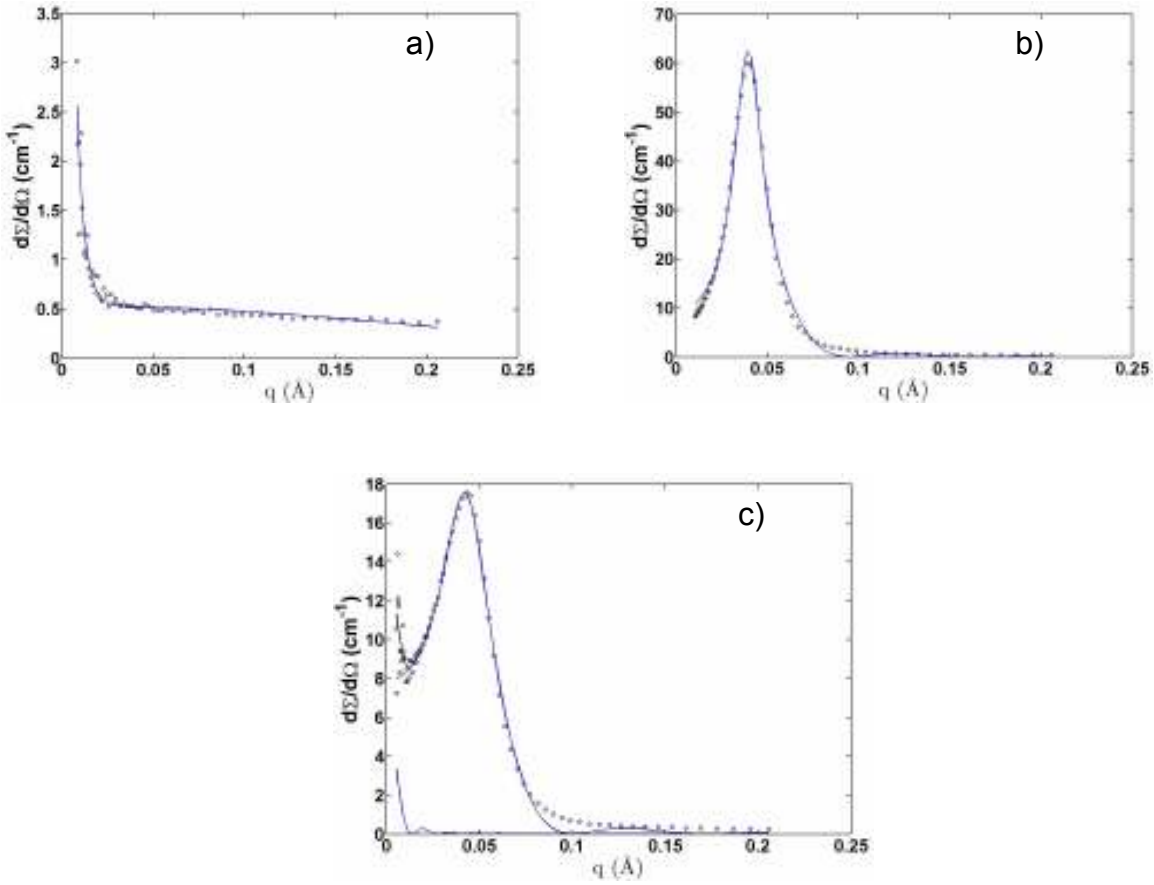

Figure 3.5 – Samples of scattering data (solid circles) curve-fitted using Z-P approximation (blue lines) from hydrated polymers. a) Very weak scattering with no distinct scattering peak (DTE-13% PEG_{1k}). Error bars are omitted for all future scans to improve visibility of the data. b) A sample with a scattering peak (DTE-41% PEG_{1k}). c) A sample with both central diffuse scattering and a scattering peak (DTE-71% PEG_{2k}).

3.2.4.1. Effect of PEG

Figure 3.6a shows the SANS scans from a series of non-iodinated polymers with different PEG concentrations, with the Z-P fitting results presented in Table 3.3. No interference peak was seen in the 0% PEG_{1k} polymer, and there was no distinct peak in the DTE-13% PEG_{1k} polymers even after immersion in dPBS for several days. The small (~ 7 Å) radius calculated from the data for the hydrated domains in these polymers

suggests that water is homogeneously distributed in the hydrated regions of these two polymers. An interference peak appears beginning with 24% PEG_{1k}, and indicates the formation of clusters of hydrated domains with *d*-spacings between 110 to 150 Å. Because water associates preferentially with PEG domains, it can be concluded that the hydrated domains seen in SANS are the result of hydration-induced phase separated PEG-rich regions. This observation is further supported in SAXS data (Murthy et al., submitted for publication). The data suggest that PEG-poor and PEG-rich domains begin to appear in hydrated samples at PEG concentration between 13 and 24%.

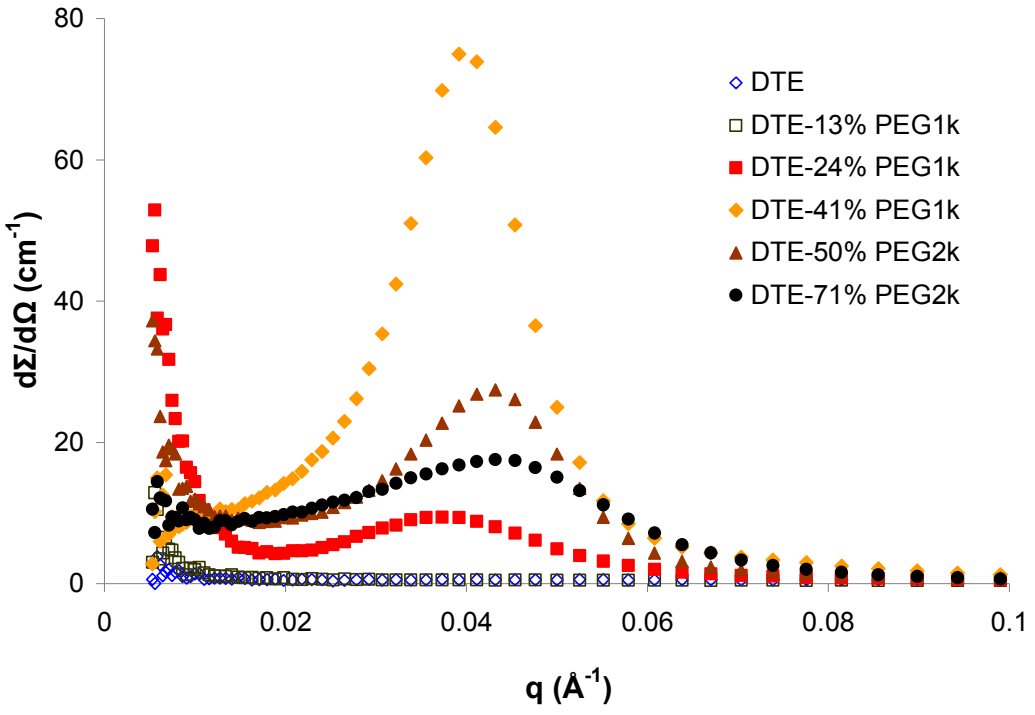

Figure 3.6 – SANS data for different PEG compositions.

Table 3.3 – Effect of PEG on Z-P model parameters in non-iodinated DTE-PEG polymers

Sample (with wt% PEG)	*d*-spacing (Å)	Fractional deviation (f_d)	Domain radius (Å)	Zero-angle scattering domains (Å)
0% PEG	581	0.28	6.85	
13 % PEG_{1k}	39.2	1.6	6.99	
24% PEG_{1k}	138	0.37	45.7	
41% PEG_{1k}	148	0.26	51.4	
50% PEG_{2k}	128	0.31	52.0	256
71% PEG_{2k}	106	0.44	45.7	239

An AFM study of the morphology in a segmented block copolymer, with PEG as one of the blocks in a chain of crystallizable tetra-amide segments, showed that the polymer is inhomogeneously swollen and the surfaces showed 10-50 nm high and 100 nm wide clusters [159]. In contrast, PEG incorporated into a noncrystallizable main-chain in our study shows much smaller hydrated domains. Figure 3.7 shows the changes in the domain size and the inter-domain spacing as a function of the water content for all polymers listed in Table 3.1, except for the polymer with PEG_{35k} that falls outside this family. At water content > 40 wt%, the *d*-spacing decreases with increasing water content, while domain radius remains essentially unchanged. The increase in the intensity between 20 and 40 wt% PEG (Figure 3.6a) with only a small change in the position of the peak suggests that the existing domains do not grow in size as the PEG (and water) content increases, but that new domains of roughly the same sizes are formed. As the number of these domains increases, they tend to pack more closely as shown schematically in Figure 3.7.

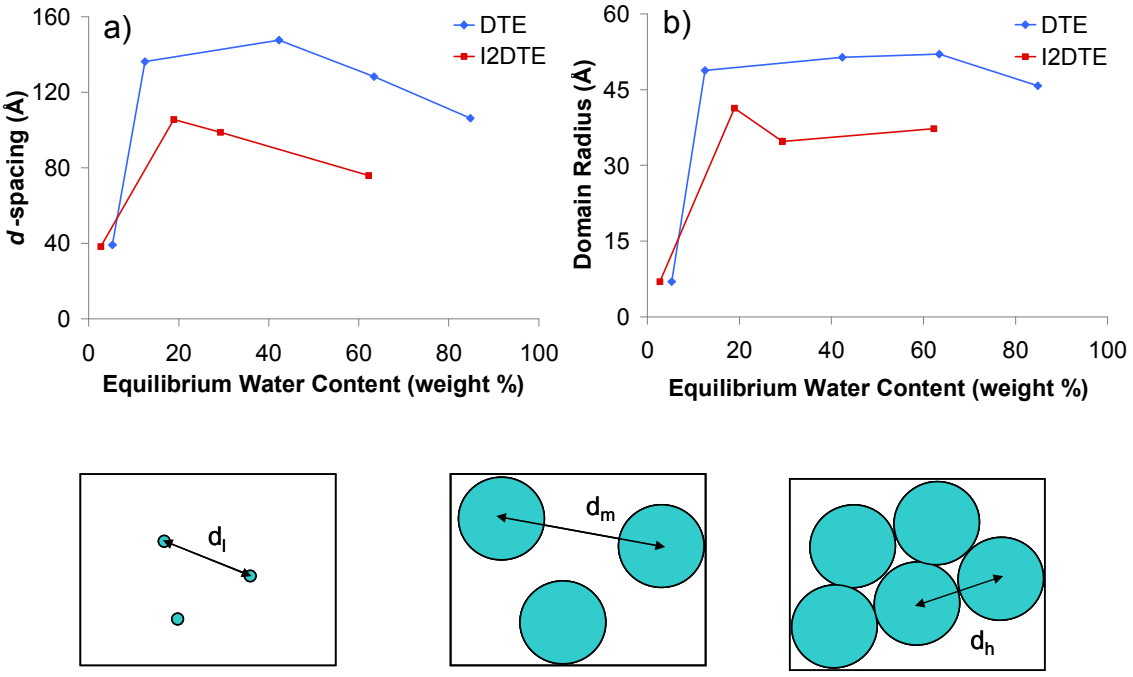

Figure 3.7 – Changes in a) water *d*-spacing as a function of EWC and b) Domain radius as a function of EWC for PEG_{1k} and PEG2k polymers. Poly(DTE carbonate) and poly(I_2DTE carbonate) homopolymers did not show any scattering, and are not included in the figure. A schematic representation shows how the *d*-spacing changes as hydration occurs at low (d_l), medium (d_m), and high (d_h) water contents.

The effect of PEG molecular weight is shown in Figure 3.8 and Table 3.4 DTE-41% PEG_{1k} and DTE-41% PEG_{35k}. An increase in PEG molecular weight from 1K to 35K increases the size of the hydrated domains (51 to 101 Å), *d*-spacing (148 to 325 Å), and fractional deviation (0.26 to 0.66). The increase in the water content from 42 to 56 wt% suggests that large blocks of PEG are able to absorb more water than smaller ones. One explanation is that the larger PEG blocks encounter stiff DTE blocks less frequently than small PEG blocks, thereby allowing them to swell more than the smaller PEG blocks.

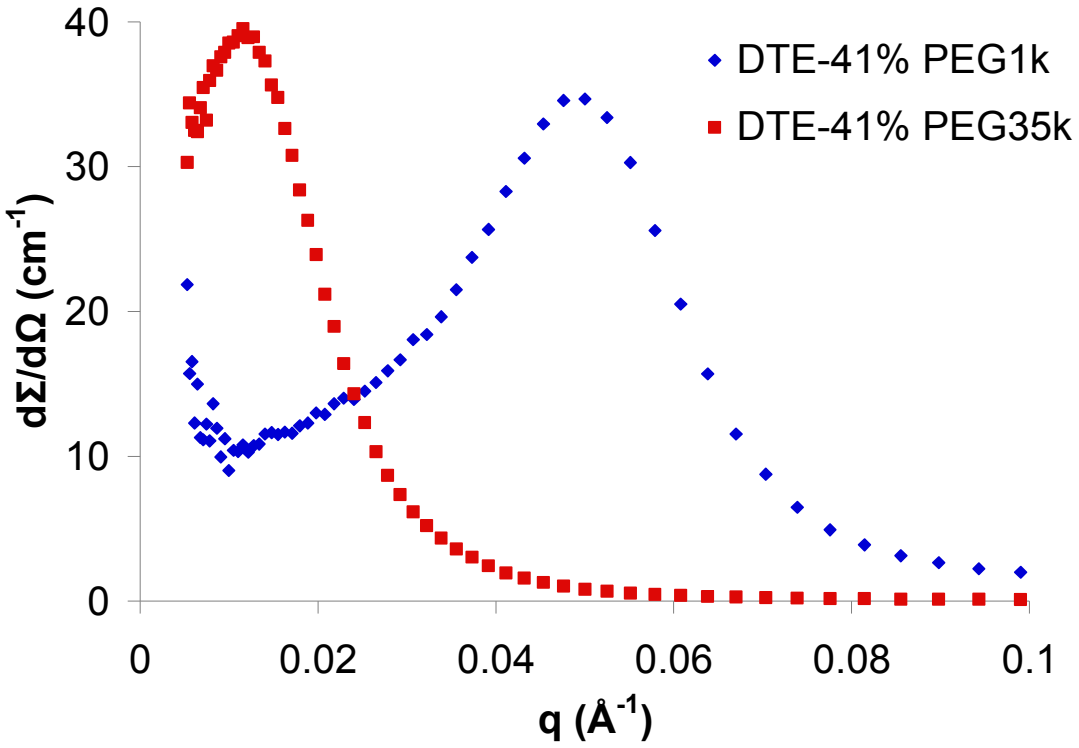

Figure 3.8 – Raw SANS data for DTE-41% PEG_{1k} and DTE-41% PEG_{35k}.

Table 3.4 – Effect of PEG molecular weight on Z-P model dimensions

Sample	*d*-spacing (Å)	Fractional deviation (f_d)	Domain radius (Å)
DTE-41% PEG_{1k}	148	0.26	51.4
DTE-41% PEG_{35k}	325	0.66	101

3.2.4.2. Effect of temperature

The effect of temperature on size and the spacing of the scattering domains appear to depend strongly on the PEG content and therefore the T_g of the polymer. Scattering data obtained while the polymer was heated *in situ* from three non-iodinated polymers

with 13, 24 and 41% PEG_{1k} are shown in Figure 3.9a, 3.9b, and 3.9c, respectively. The results are summarized in Table 3.6. Even after heating the DTE-13% PEG_{1k} polymer to 37 and 60° C, no scattering was observed, and hence these results are not listed in Table 3.6. These results establish DTE-13% PEG_{1k} as a lower limit for phase separation.

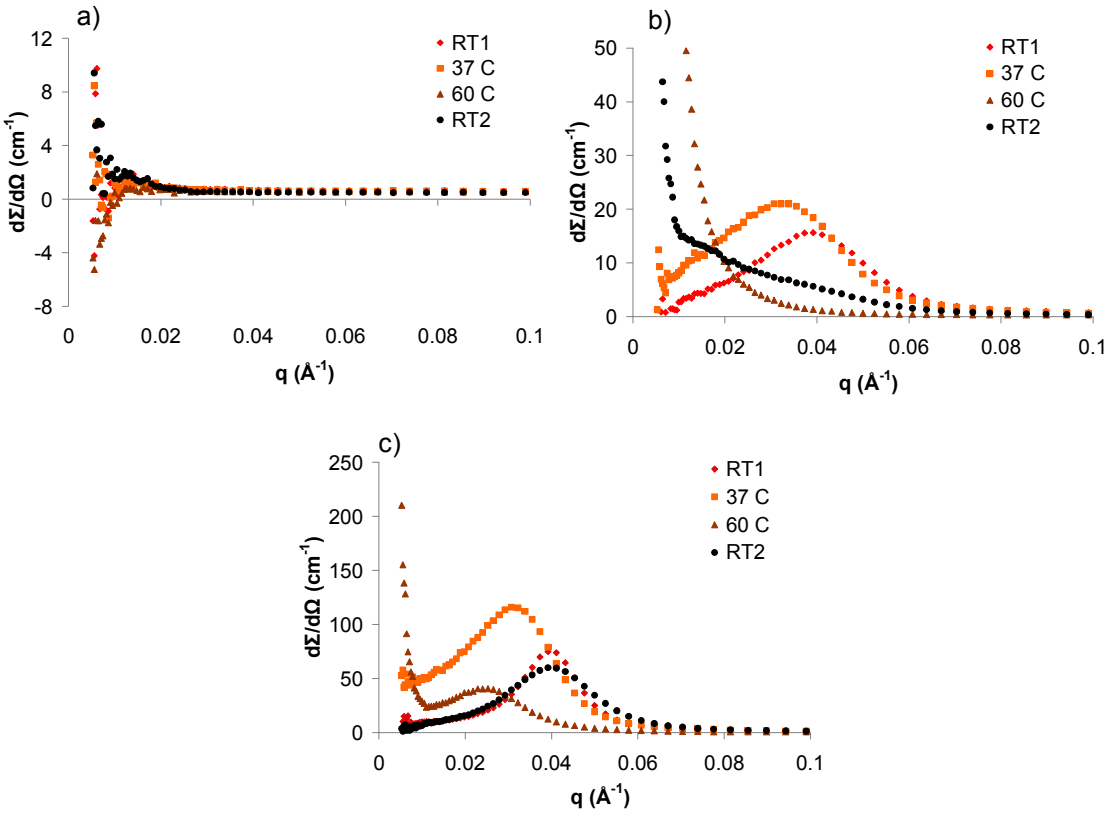

Figure 3.9 – SANS data for a) DTE-11.5% PEG_{1k}, b) DTE-24% PEG_{1k}, and c) DTE-41% PEG_{1k} at different temperatures. RT1 = initial scan at room temperature, RT2 = scan at room temperature after heating

Table 3.5 – Effect of temperature on Z-P parameters for selected DTE-PEG polymers

Sample (with wt% PEG)	*d*-spacing (Å)	Fractional deviation (f_d)	Domain radius (Å)	Zero-angle scattering domains (Å)
DTE-41% PEG_{1k} 23° C initial	148	0.26	51.4	
DTE-41% PEG_{1k} 37° C	161	0.44	57.7	
DTE-41% PEG_{1k} 60° C	192	0.44	71.5	311
DTE-41% PEG_{1k} 23° C final	141	0.31	47.3	
DTE-24% PEG_{1k} 23° C initial	138	0.37	45.7	
DTE-24% PEG_{1k} 37° C	142	0.47	53.0	
DTE-24% PEG_{1k} 60° C	394	0.28	93.1	
DTE-24% PEG_{1k} 23° C final	-	0.28	57.4	328

In the DTE-24% PEG_{1k} polymer, which has well-defined interference peak, the *d*-spacing increased from 138 to 142 Å when the sample was heated from room temperature (23° C) to 37° C, and then to ~ 400 Å upon further heating to 60° C (peak maximum shifts from 0.04 to 0.034 Å and then to ~ 0.004 $Å^{-1}$). The large changes in scattering at 60° C, well above the T_g, arise from the coalescence of the smaller domains into larger domains as the temperature is increased. However, even as the radius and the separation of the domains increases, a decrease in the fractional deviation suggests a more uniform distribution of these domains. Scans obtained at room temperature after cooling from 60° C show partial recovery of the starting structure. We note that the rescan at room temperature was done 4 h after the 60° C scan. Our experience with these polymers suggests that given more time, the structure would have fully recovered. The sample was semitransparent at room temperature and became white and opaque after cooling from 60 to 23 ºC. After 12 h, however, the sample returned to its original semitransparent state.

This observation is consistent with the suggestion that a polymer with faster relaxation (i.e. lower T_g) would exhibit complete reversibility within the time scale of our experiment.

The scans from the DTE-41% PEG_{1k} polymer show that the *d*-spacing increases from 148 to 161 Å upon heating to 37 °C from room temperature (the interference peak shifts to a smaller *q*). There are other significant changes upon further heating to 60 ºC: the distance between the water-domains increases from 161 to 192 Å. This is accompanied by a broader distribution of these distances (Table 3.6); and some of these domains merge to form larger (~ 300 Å radius) domains, as indicated by the large zero-*q* scattering. Unlike the DTE-24% PEG_{1k} polymer, this DTE-41% PEG_{1k} polymer showed almost complete reversibility as indicated by the almost complete recovery of the original scattering curve upon cooling the sample back to room temperature, verifying our previous assumption.

3.2.4.3. Effect of Iodine

Polymers can be made radio-opaque by iodination so that they can be used in applications such as vascular stents and aneurysm coils [98, 160]. Iodination also has been reported to affect water uptake behavior [103] and chain stiffness [161]. These effects on the hydration behavior were investigated in our polymers by comparing polymers in which the tyrosine rings were iodinated with non-iodinated poly(DTE-*co*-PEG carbonates)s. One effect of iodination is it increases T_g compared to non-iodinated

polymers (Table 3.6). The influence of iodine on the phase behavior is shown in Figure 3.10 in which the scattering from iodinated and non-iodinated polymers with 41% PEG_{1k}, 50% PEG_{2k} and the 71% PEG_{2k} polymers are compared. Iodinated polymers with 0 and 8% PEG_{1k}, like their non-iodinated counterparts, showed no significant interference peak (data not shown). The interference peak first appears between approximately 10 and 25% PEG. Thus, despite molecular differences caused by the incorporation of iodine, the threshold for phase separation is comparable to the non-iodinated polymers.

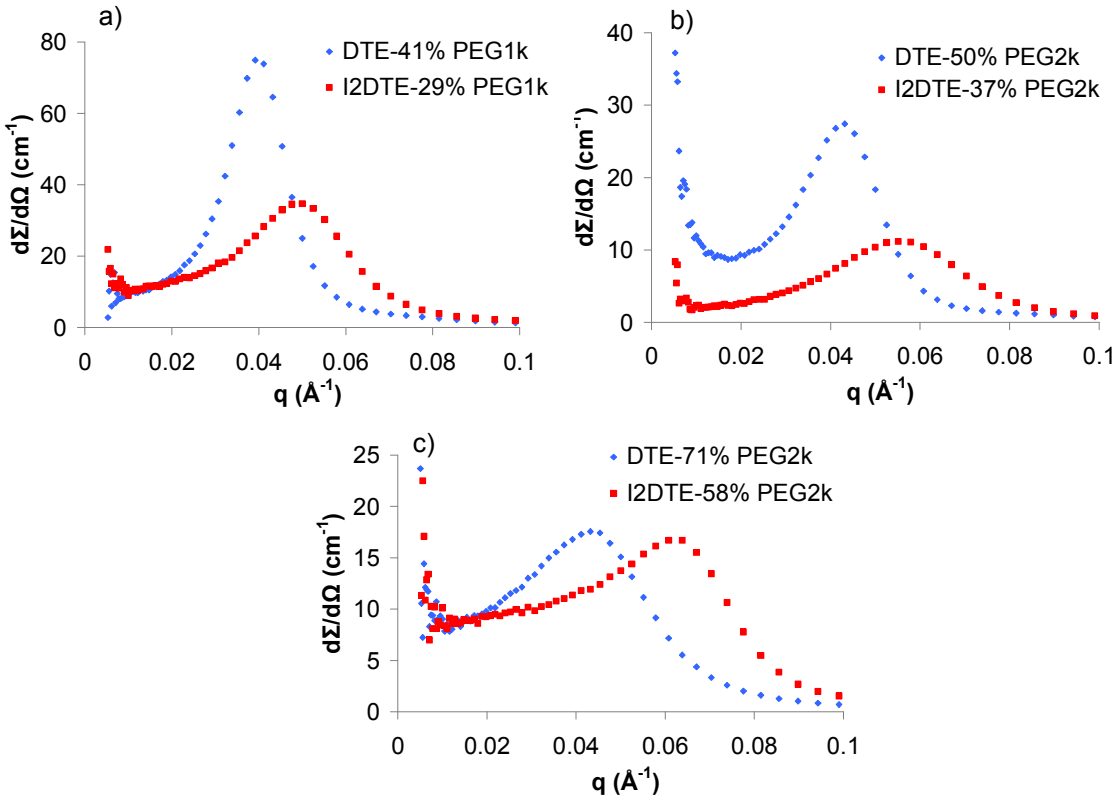

Figure 3.10 – Comparisons in SANS interference peaks between DTE (blue squares) and I_2DTE (red squares) polymers containing (a) 41% and 29% PEG_{1k}, (b) 50% and 37% PEG_{2k}, and (c) 71% and 58% PEG_{2k}. The three polymer pairs contain 20mol%, 15mol%, and 30mol% PEG, respectively.

The main difference in the hydration behavior between the iodinated and the non-iodinated counterparts is that the hydrated domains in the iodinated polymers are smaller and closer together while the fractional deviations remain unchanged (see Table 3.3 and Table 3.6). For instance, even though both the 37% PEG_{2k} iodinated polymer and 70% PEG_{2k} non-iodinated polymer absorb about the same amount of water (63 wt%), the hydrated domains in the two polymers are 75 and 125 Å apart, respectively. This difference in domain size occurs even though the iodinated 58% PEG_{2k} has a lower T_g than iodinated 50% PEG_{2k}. It could be that the iodinated DTE segments, which are stiffer, are able to confine PEG domains more than the non-iodinated segments.

Table 3.6 – Effect of PEG in I_2DTE-PEG polymers

Sample	*d*-spacing (Å)	Fractional deviation (f_d)	Domain radius (Å)	Zero-angle scattering domains (Å)
I_2DTE	62.2	1.6	5.96	
I_2DTE-8% PEG_{1k}	38.3	2.5	6.94	
I_2DTE-29% PEG_{1k}	106	0.36	41.3	348
I_2DTE-37% PEG_{2k}	98.8	0.34	34.7	
I_2DTE-58% PEG_{2k}	75.8	0.40	37.2	346

For each pair of polymers (same mole % PEG) examined, the peak is weaker in the iodinated polymer, which is due to lower wt % of PEG (and hence smaller water uptake). As the PEG content increases from 40 to 70 wt%, the difference in peak intensity becomes less pronounced. This correlates with the smaller difference in water content within the pair at these PEG concentrations (Table 3.1). In contrast, the difference in *d*-spacing becomes larger (Figure 3.10). This suggests that while the water content is

determined simply by the PEG content, the morphology is determined by the complex interactions between the stiff DTE and I_2DTE segments and PEG domains.

3.2.4.4. Evolution of hydrated structures

The total volume of the scattering units, which for instance are the hydrated domains at < 50 wt% PEG, can be estimated by calculating a parameter known as the invariant (Q) from the SANS curve using the expression:

$$Q = \int q^2 I(q) dq \tag{3.1}$$

Q is also the product of the total irradiated volume and the square of the difference in scattering-length density, and is independent of domain shape. The expectation was that the invariant would be correlated with the water content, as described in other polymer-solvent systems [109]. However, no such correlation was found in our samples (data not shown). To understand this unexpected result, we examine the peak intensity of each series of SANS data. Figure 3.11 shows that as PEG increases from 24 to 41 wt%, corresponding to an increase in water content from 13 to 42 wt%, the SANS intensity increases as expected. However, a further increase in PEG from 50 to 71 wt%, corresponding to a water content increase from 63 and 85 wt%, causes the scattered intensity to decreases.

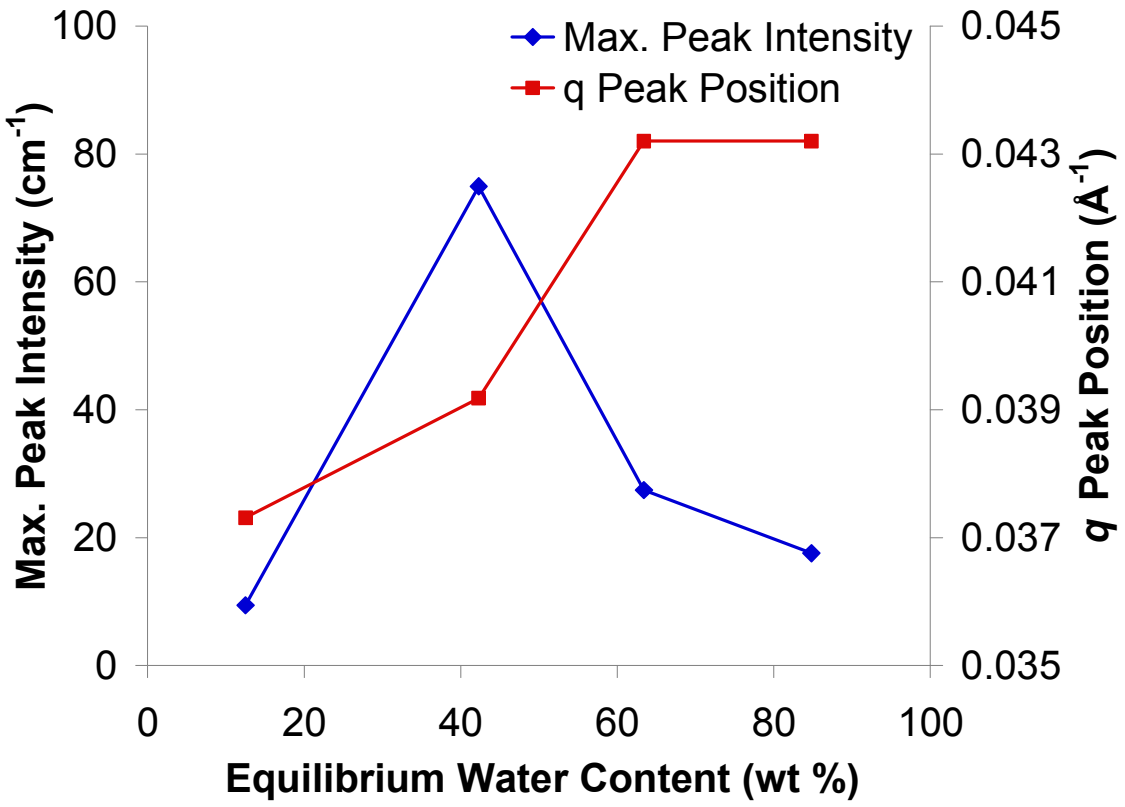

Figure 3.11 – Plot of the changes in the position and the intensity of the interference peak maximum in the non-iodinated series as a function of the equilibrium water uptake.

One explanation for this change beyond about 45 wt% water uptake is that there is inhomogeneous swelling. An example of inhomogeneous swelling in our samples is clearly seen in the variable temperature data (Figure 3.9). The interference peak first increases with temperature from 22 to 37 ºC due to enhanced water content, but then decreases at higher temperatures (60 ºC). It is possible that the hydrated domains coalesce to form large islands and contribute to the central diffuse scattering at q= 0 $Å^{-1}$ instead of the interference peak. This change results in isolated large domains as well clusters of smaller domains. However, for the data with increasing PEG contents (Figure 3.6a and Figure 3.11), it is more likely that phase inversion occurs at ~ 50 wt% PEG (Figure 3.12).

Below this value, discrete water domains exist in a continuous DTE matrix, and the intensity increases with hydration. Above this value of 50 wt% PEG, the DTE domains can be considered as islands in a continuous PEG/water matrix. With increased PEG contents, the scattered intensity decreases as the number of DTE domains decreases.

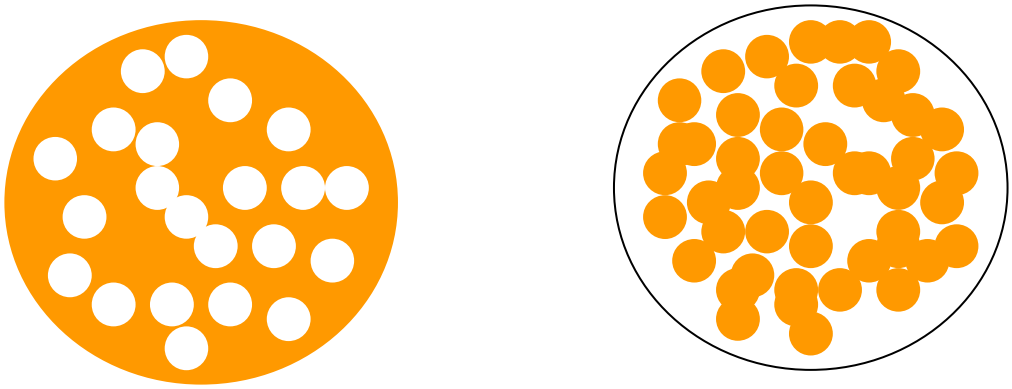

Figure 3.12 – A graphic representation of phase inversion, where orange represents DTE and white represents PEG. At low PEG contents, PEG is present as small domains within a DTE matrix. When PEG content increases above ~50 wt%, PEG becomes the matrix, and DTE becomes the minor component. This results in a lowered scattering intensity, and the invariant is no longer indicative of water content.

3.3. Physical and biological implications

The hydrated PEG domains that we identify in the SANS data could influence many of the bulk and surface properties of these polymers. We have found that at very low PEG concentration, (<13 wt%) water softens the polymer. At significantly higher PEG contents (>40 wt%) the hydrated material behaves like a gel [104]. Between these two extremes, under certain PEG contents and molecular weights, water has been shown to increase the modulus of the polymer [162]. The critical mass of water required to form phase separated domains is ~ 13%. Above this EWC, it appears that PEG segments phase separate as hydrated domains in PEG-containing polycarbonates. The changes in the

interactions between these phase separated soft segments and the hard DTE segments are speculated to be the cause of enhanced modulus observed within a narrow range of hydration [163].

Both increases in water uptake and increases in temperature are expected to enhance erosion. Based on TEM analysis of a DTE-20 wt% PEG_{1k} non-iodinated polymer (8 mol% PEG_{1k}, as referenced in the paper), Sousa et al. found that at 2 days, water and PEG appear to be homogeneously distributed at a resolution of 150 Å [146]. At 12 months, erosion of PEG-rich fragments results in interconnected network pathway high diffusivity channels with characteristic length scales of 500-1000 Å. SANS data show that in the DTE-24 wt% PEG_{1k} polymer, the closest in our set to the 20 wt% PEG_{1k} polymer used for TEM, even after a few hours of hydration, the distribution of water is not homogeneous at a length scale of 100 Å. Instead, domains of water 50 Å in radius appear to be separated by about 150 Å. Our results suggest that isolated hydrated domains are formed at low water contents. As PEG content increases, water content will also increase, leading to domains that are larger in number and packed more closely together. After a critical water content is reached, these ~10nm size domains could merge to form larger ~ 100 nm islands that eventually from hydration channels and facilitate degradation of the polymers. These channels could be the precursor of μm-sized channels that form during erosion, including the interconnected channels reported by Sousa and coworkers [146].

SANS results thus provide insight not only about how materials may phase-separate, but also how their diffusion properties may change upon hydrolytic degradation and erosion. By controlling the PEG content, PEG molecular weight, and the stiffness of

the main chain, it is possible to control the formation and evolution of hydration domains and channels and thus the degradation characteristics of the polymer. Similarly, in polylactide/polyglycolide-based materials, the evolution of fractal structures or changes in spacing between crystalline and amorphous regions may provide insight into the erosion and drug delivery properties of these polymers.

Cima et al. have previously reported that cells cultured on PLLA behave differently based on the crystalline structure of the polymer [164]. Because polymer degradation and erosion occur over time, it then becomes reasonable to assume that for crystalline polylactide/polyglycolide-based materials, cell behavior may also change dynamically over time. The data seen for PGA in this study shows a gradual change in the size of the crystalline domains with water uptake, further reinforcing this argument.

3.4. Initial protein adsorption studies

Protein adsorption is one of the first events that occur upon implantation of a biomaterial into the body [1]. The surface-adsorbed proteins mediate the attachment of larger biological agents such as cells and bacteria [165]. Hydrophilic polymers such as PEG have well-documented protein resistant properties because of their ability to form a repellant hydration shell [56, 98, 166-167]. It has been previously known that in graft copolymers, sparsely grafted PEG can still allow proteins to adsorb to a surface [70, 168]. An analogous effect was produced in random multiblock copolymers by concentrating PEG into regions with high PEG molecular weights. As shown in Table 3.4, increasing

the PEG molecular weight increases the *d*-spacing between hydrated domains. It is hypothesized that in random multiblock copolymers, the size and spacing of these protein-repellent hydrated regions correlate with protein adsorption such that closely spaced PEG regions are able to repel most proteins. Conversely, polymers with widely separated hydration domains, namely polymers copolymerized with high molecular weight PEG and low PEG content, may support protein adsorption due to the presence of large, phase separated, hydrophobic regions. To test this theory, fibrinogen adsorption was studied on select DTE-PEG polymers containing identical amounts of PEG but different PEG molecular weights.

Initial fibrinogen adsorption studies with DTE-41% PEG_{100}, DTE-41% PEG_{1k}, and DTE-41% PEG_{35k} support the idea that PEG molecular weight may modulate protein adsorption by spatially-mediated means (Figure 3.13). Fibrinogen adsorption for DTE-41% PEG_{100} was high, comparable to the homopolymer poly(DTE carbonate). DTE-41% PEG_{1k}, shows complete repellence on all surfaces measured. Upon increasing the PEG molecular weight to 35k, protein adsorption increased again, back to levels seen with 41% PEG_{100} and poly(DTE carbonate).

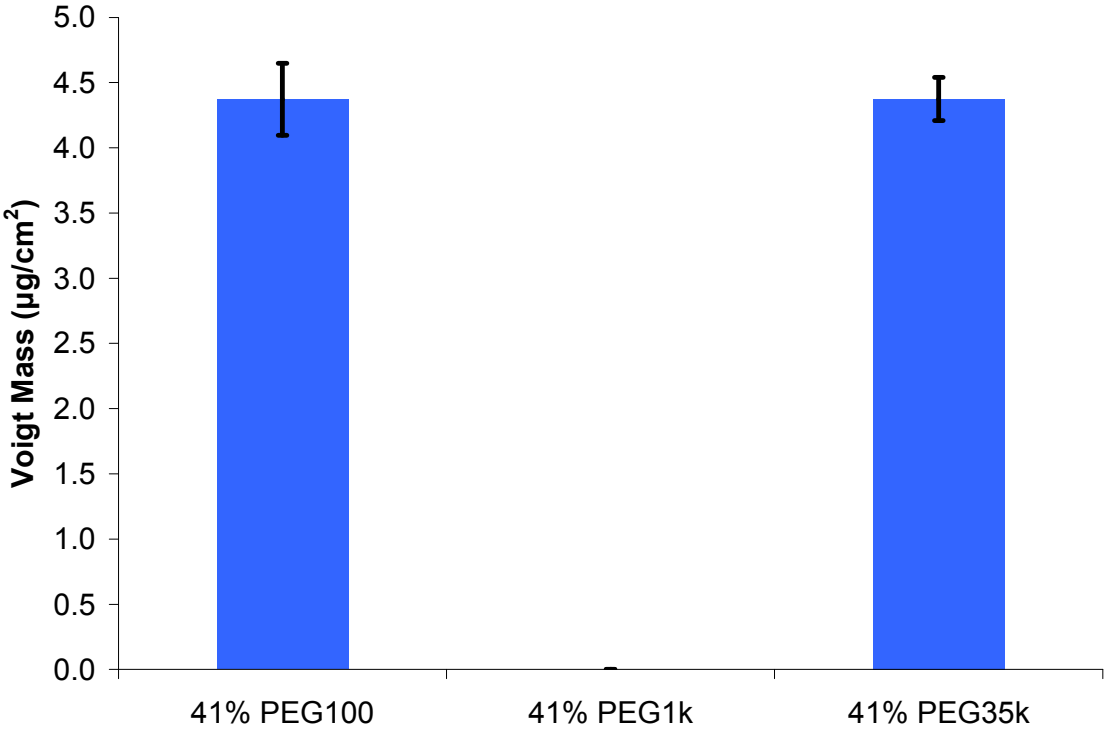

Figure 3.13 – Fibrinogen adsorption results for DTE-41% PEG_{100}, DTE-41% PEG_{1k}, and DTE-41% PEG_{35k}. Complete repellence was observed for the PEG_{1k}-containing material, while the PEG_{100} and PEG35k-containing materials both showed substantial adsorption.

While DTE-41% PEG_{100} was not measured by SANS in this study, one can rationalize the large amount of protein adsorption observed by considering the number of ether oxygens in the PEG chain. The fact that the values are about the same as in the DTE homopolymer suggest that the polymers with PEG_{100} segments do not have the typical characteristics of a hydrophilic polymer. The lack of protein repellence in low molecular weight PEG copolymers has been reported previously [91, 169]. This can be explained by the fact that lower molecular weight PEGs have fewer ether oxygens per unit molecular weight than higher molecular weight PEGs. The graph in Figure 3.14 depicts how the

number of ether oxygens per molecular weight of PEG change as PEG molecular weight is increased.

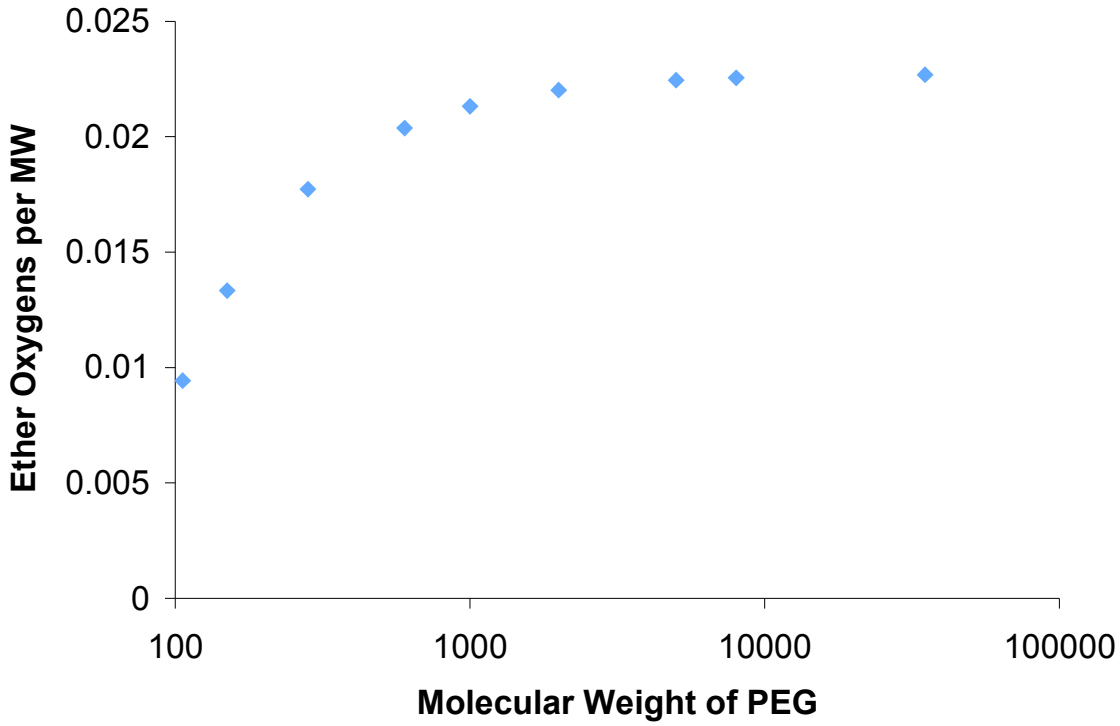

Figure 3.14 – Number of ether oxygens per PEG molecule as a function of PEG molecular weight. The number of ether oxygens per molecular weight of PEG is the number of repeat units minus 1, e.g. PEG_{100} has 2 repeat units and 1 ether oxygen, while PEG_{1000} has 23 repeat units and 22 ether oxygens.

SANS data from Table 3.4 can be used to determine the dimensions of PEG regions and DTE regions for a given space to see if this data correlates with the previous assertion that high molecular weight PEG polymers are less able to adsorb protein. An equilateral triangle is constructed from the *d*-spacing value, and the area is calculated using the standard relationship A=bh/2. PEG-rich regions are subtracted from the corners of this triangle, amounting to 1/6 of the circle area for each corner, or $\pi r^2/2$. The dimensions of fibrinogen have been described at 470 Å x 45 Å x 45 Å [26], and by

approximating fibrinogen as a rectangle, the number of fibrinogen molecules adsorbed in either the end-on or side-on conformation can be calculated. Fractional deviation was discounted to provide a general idea of the average surface area available for adsorption.

Sample	*d*-Spacing (Å)	Fractional Deviation	Radius (Å)
DTE-41% PEG_{1k}	148	0.26	51.4
DTE-41% PEG_{35k}	325	0.66	101

470 Å x 45 Å x 45 Å

Side on: 21,000 $Å^2$

End on: 2,000 $Å^2$

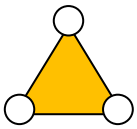

DTE-41% PEG_{1k}

Base = 148 Å, height = 128 Å
Area = bh/2= 9500 $Å^2$
9500 – $(51^2*\pi)/2$= 5400 $Å^2$

Side on = 5400/21,000 = 0
End on = 5400/2,000 = 2

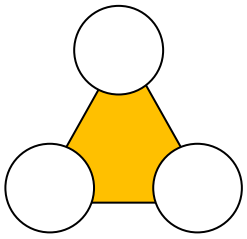

DTE-41% PEG_{35k}

Base = 325 Å, height = 281 Å
Area = bh/2 = 45,700 $Å^2$
45.700 – $(101^2*\pi)/2$=30.000 $Å^2$

Side on = 30,000/21,000 = 1
End on = 30,000/2,000 = 14

Figure 3.15 – Quantification of DTE-rich and PEG-rich areas based on SANS data. Dimensions for fibrinogen based on [26].

The results from Figure 3.13 suggest that this model may be initially sufficient to describe protein adsorption behavior in PEG-containing polymers. Several months after synthesis, however, the protein adsorption capabilities of DTE-41% PEG_{35k} became less pronounced, and eventually disappeared entirely. In examining possible changes in the polymer properties, a change in M_w from 185 kDa to 76 kDa was observed after 6 months of storage. The polymer was resynthesized, but these new batches of polymer did not reproduce the protein adsorption capabilities of the original material. This observation indicates that it is not only chemistry that dictates protein adsorption capabilities, but also

molecular characteristics such as molecular weight, polydispersity, and chain configuration.

3.5. Conclusions

SANS is a useful technique to characterize the distribution of hydrated domains in polymers, although it has so far rarely been used to study the distribution of water in biodegradable polymers. The water uptake and scattering properties of three types of polymers were studied: semicrystalline polymers, amorphous polymers with homogeneous water distribution, and amorphous, phase separated polymers with heterogeneous water distribution. This study is one of the first to quantify the phase-separation morphology and nanoscale dimensions of random, PEG-containing multiblock copolymers. The relationships between phase separation and protein adsorption and erosion illustrate the importance of morphological characterization in biodegradable polymer design.

In PGA, scattering was observed even for dry samples as a result of contrast between amorphous and crystalline regions. Hydration of this polymer for intermediate time periods resulted in contrast matching and as a result the SANS intensity decreased. Further hydration increased the intensity above that of the dry polymer. No clear relationships could be derived between PLA and scattering behavior because of the negligible water uptake of PLA. In PDLLA and PLGA, hydration results in a fractal

structure, and surface fractals transform into mass fractals as the polymers absorb more water.

In DTE-PEG polymers, three distinct regimes of hydration were established. Below certain PEG composition (<24 wt% PEG_{1k}) water is homogeneously distributed at 10 Å length scales in. A similar threshold value may exist in other PEG copolymer systems. Beyond this first critical hydration level, water exists as domains of 30-50 Å size which are separated by ~ 100 Å. Increases in either the amount of PEG or the PEG molecular weight increases the domain size and spacing until a second critical hydration level at water contents of approximately 50 wt% when domain sizes begin to shrink despite increases in PEG concentration (Figure 3.10).

Upon heating, small, closely packed domains merged into large, widely separated domains. These changes were reversible as a function of polymer chain flexibility, with more flexible polymers (i.e. more PEGylated) reverting to their original morphology faster. Increased rigidity of the polymer chain, in this instance by adding iodine to the main chain, results in smaller and closer packed water domains. It is likely that these structured domains are precursors to the formation of a network of channels that facilitate erosion. The PEG-rich selective degradation noted in this system previously [146] and in other systems [147-148] implies that the insights into the behavior of tyrosine-derived polycarbonates obtained in these studies are applicable to other hydrophobic-hydrophilic copolymer systems. The use of two backbone monomers with different stiffnesses, DTE and I_2DTE, illustrate how molecular mobility can affect domain size and spacing.

Initial protein adsorption studies indicated that spatial arrangements of PEG in random multiblock copolymers could potentially modulate protein adsorption. However,

inconsistent data and a seemingly time and molecular weight dependent relationship between protein adsorption and molecular weight of certain polymers appeared to also play a role in adsorption capabilities. To further understand the effect of these chemical and physical changes on biological properties, protein adsorption studies on a systematic DTE-PEG library, with variations in PEG concentration and molecular weight, were performed. These studies, as well as an extension of morphological work, are described in the next chapter.

4. Parallel synthesis and characterization of poly(DTE-*co*-PEG carbonate) polymers

Based on the manuscript: "Examination of physicochemical factors that cause polymeric substrates to transition between protein adsorption and repellence" by Arnold Luk, Ramiro Rojas-Escontrillas, Sanjeeva Murthy, Durgadas Bolikal, Joachim Kohn, in preparation.

4.1. Background

In Chapter 3, preliminary work was performed that suggested a possible trend in phase-separated spatial dimensions and protein adsorption in DTE-PEG polymers containing high PEG molecular weights. However, these results were transient, and the exact mechanism by which protein adsorption occurred still remains to be discovered. To convincingly draw conclusions about general phenomena that occur in PEG-containing samples, a sufficiently large library with systematic variations in PEG molecular weight and PEG content must be synthesized.

As described in Chapter 3, DTE-PEG polymers with 24 wt% PEG represent the approximate threshold where phase separation can be quantified by SANS. Therefore, a library of DTE-PEG containing 20, 30, and 40 wt% PEG and six different PEG molecular weights ranging from 100 to 35k was proposed as the investigative library to present sufficiently large chemical and morphological variation. PEG_{100}-containing polymers were chosen as the low PEG molecular weight polymers because PEG_{100} is the lowest molecular weight of PEG that still contains the ether oxygen moiety responsible for

hydrogen bonding with water. It is important to realize that these low PEG molecular weight polymers only serve as research tools, and would likely make poor degradable biomaterials because of the reported toxicity of PEGs with molecular weights below 400 [170]. PEG_{35k} is chosen for the upper limit of PEG molecular weights because molecules with molecular weights of 35k approach the limits renal clearance [171]. The breadth of the proposed library can provide insight into the hydration and protein adsorption mechanisms of a wide range of different PEG characteristics.

Clearly, the synthesis of 18 different polymer compositions in a reproducible fashion presents a significant technical challenge. For DTE-PEG polymers, the required amount of time for synthesis and work-up of a single polymer is approximately eight hours. To aid in the development of such a library, automated parallel synthesis was employed to prepare a large number of polymers in a comparatively small amount of time. The development of automated parallel synthesis methods for high-throughput materials discovery has greatly improved the rate at which discoveries can be made in the biomaterials field [172]. After initial investments in time and resources are made to solve technical issues, a method for repeated syntheses of a given polymer system using automated equipment can be developed. Automation can significantly reduce the amount of time needed for the synthesis of many different polymers at a single time, and can also eliminate human error and variation that can occur between operators [173]. Optimal procedures for the automated synthesis of tyrosine-derived polycarbonates had been previously described [137] and were capitalized upon for this study to synthesize a large polymer library in a far shorter period of time than could be accomplished with manual synthesis.

The synthesized library allowed for systematic characterization of the phase-separation behavior of PEG-containing polymers. The trends observed from Chapter 3 could therefore be more deeply explored and generalized to the different PEG concentrations and molecular weights. Protein adsorption studies provided insight into the potential effects of phase separation on the organization of different sized proteins on the surface of the polymers. The validity of the spatial organization hypothesis proposed previously was then determined. Other potential mechanisms and methodologies for examining the effects of phase separation on protein adsorption were explored if the hypothesis was invalidated.

The nomenclature used to identify individual polymers is the same as the previous chapter, except that names are further abbreviated to only describe the PEG weight % and PEG molecular weight because all polymers described in this chapter contain only DTE and PEG. For example, 20-20k = poly(DTE-*co*-20wt% PEG_{20k} carbonate). Again, generalized poly(DTE carbonate)s are referred to simply as DTE-PEG polymers. GPC-measured molecular weight will be discussed in terms of weight average molecular weight (M_w) and polydispersity, with the number average molecular weight (M_n) implied in the polydispersity value.

4.2. Results and Discussion

4.2.1. Automated parallel polymer synthesis

A total of 50 of the 72 polymers were successfully synthesized, representing a success rate of about 70%. Importantly, the total amount of time required for synthesis and work-up for the 72 individual polymers was only 48 hours, compared to approximately 144 hours (18 compositions * 8 hours) for theoretical manual synthesis. Success was defined as the polymers having a M_w higher than 100 kDa, a polydispersity less than 1.5, and a confirmed composition by NMR. A lower M_w or higher polydispersity would indicate the existence of large amounts of unreacted monomer or PEG. Because of the complexity of the device used and the multitude of steps required for each individual synthesis, lag times between phosgenations, and potential solvent evaporation, a 70% success rate represents an average result (Dr. Ramiro Rojas, personal communications). At least one sample for each composition was successfully prepared, and the molecular weight, T_g, and EWC for each polymer was characterized. Polymers with the highest molecular weights and lowest polydispersities for each of the 18 individual compositions and with yields of at least 150 mg were selected for film compression molding for SANS (Table 4.1). The multiple T_gs present for the polymers containing PEG_{35k} illustrate that a high concentration of long, continuous chains of PEG can produce phase separation that is observable through DSC (Table 4.2).

Table 4.1 – Characteristics of polymers synthesized by automated parallel synthesis. PS = phase separated, i.e. multiple T_gs present on 2nd heat.

composition	M_w (kDa)	Pd	dry T_g (ºC)	EWC (wt%)
20%-100	234	1.38	56.8	11.8
30%-100	196	1.43	44.2	11.1
40%-100	246	1.34	31.9	16.6
20%-1k	332	1.36	40.7	10.7
30%-1k	325	1.25	15.7	29.9
40%-1k	237	1.22	6.76	31.5

20%-2k	326	1.29	40.0	15.8
30%-2k	207	1.34	-0.96	34.7
40%-2k	268	1.28	3.65	43.2
20%-8k	431	1.20	22.0	23.9
30% 8k	397	1.24	16.5	33.6
40%-8k	404	1.19	-6.99	42.2
20%-20k	431	1.23	20.8	24.5
30%-20k	364	1.23	6.14	47.3
40%-20k	416	1.20	-8.53	54.1
20%-35k	373	1.21	PS	28.8
30%-35k	395	1.27	PS	28.0
40%-35k	329	1.26	PS	50.1

Table 4.2 – Glass transition data for polymers containing PEG_{35k}.

	T_g1 (°C)	T_g2 (°C)	Tm (°C)
20-35k	-9.8	84.2	N/A
30-35k	-15.4	83.8	N/A
40-35k	-22.3	83.2	55.7

4.2.2. Small angle neutron scattering (SANS)

SANS is one of a handful of techniques that can determine the nanoscale morphology of bulk materials. Upon hydration with DPBS, contrast between phases develops from the inherent scattering differences that exist between deuterium and hydrogen [158, 174]. A scattering peak in the q vs. I(q) data is indicative of phase separation (Figure 4.1a), while a lack of a peak suggests that PEG domains are evenly distributed and homogeneous throughout the sample (Figure 4.1b). Despite the fact that the Z-P model is a rather simplistic model for describing SANS data, the polymer data were fit well, with most least squares fit values occurring at $R^2 > 0.9$ and many at $R^2 > 0.95$ (Table 4.3).

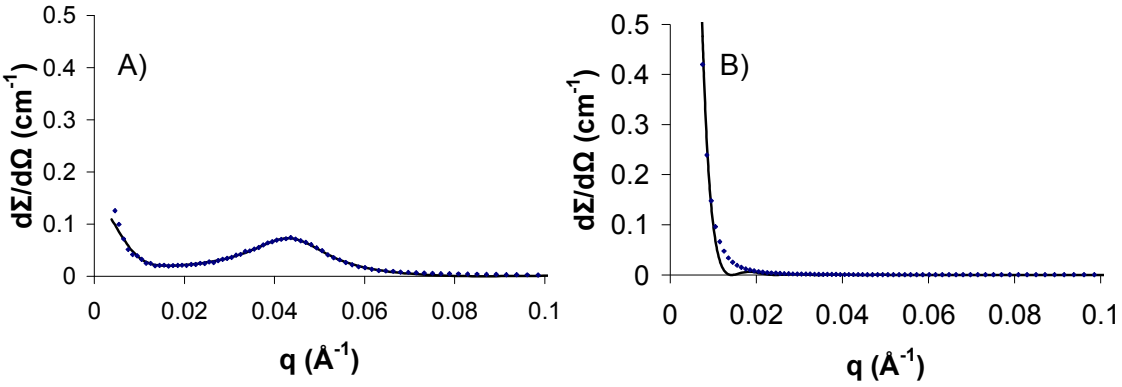

Figure 4.1 – Raw scattering data (blue dots) and Z-P fit (solid black line) for DTE-PEG polymers. Panel A shows a material with a scattering peak (30-1k), indicating the formation of discrete hydrated regions. Panel B shows a material with no scattering peak (30-100), showing that water is homogeneously distributed within the sample.

Table 4.3 – Fitted Z-P dimensions and R^2 correlation coefficient for DTE-PEG library.

Polymer	radius (Å)	*d*-spacing (Å)	fractional deviation	R^2 value
20-100	318	62.1	2.3	0.970
30-100	315	31.9	6.0	0.988
40-100	313	32.5	4.6	0.980
20-1k	53.2	133	0.43	0.995
30-1k	51.6	127	0.30	0.967
40-1k	51.9	127	0.26	0.796
20-2k	45.7	133	0.34	0.780
30-2k	60.2	130	0.27	0.975
40-2k	50.0	122	0.28	0.968
20-8k	76.6	217	0.34	0.966
30-8k	73.7	188	0.36	0.780
40-8k	72.9	189	0.36	0.997
20-20k	118	291	0.44	0.948
30-20k	92.9	245	0.39	0.977
40-20k	87.7	245	0.38	0.976
20-35k	145	343	0.73	0.995
30-35k	114	282	0.52	0.892
40-35k	119	311	0.56	0.980

Overall trends indicate that the domain radii increase as the PEG molecular weight increases (Figure 4.2). As domain radius increases, the *d*-spacing also increases.

Upon increasing the PEG concentration, PEG domains decrease in radius, but also have reduced *d*-spacing. Also notable is the fact that the short range order increases as PEG molecular weight increases. For polymers containing PEG_{100}, radius values tended to be much higher than the rest of the series, while *d*-spacing values were less than the radius of the domains. This information suggests that these materials are homogeneous, a conclusion supported by the fact that no notable scattering peak appears in these samples. The similar values between the PEG_{1k} and PEG_{2k} series suggest that the phase-separated microstructures that occur between these two polymers are similar, and that they are interchangeable during the polymerization process for the purposes of protein repellence. Similarities between the properties of PEG_{1k} and PEG_{2k} have also been described by other groups [47].

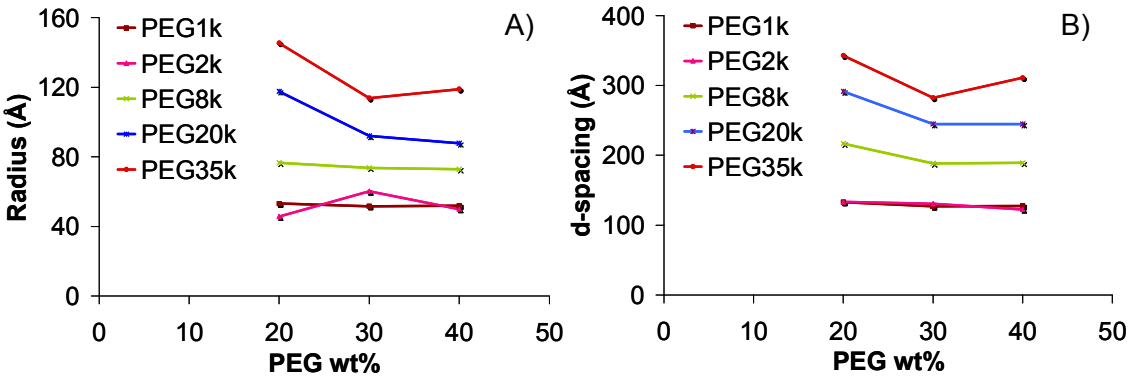

Figure 4.2 – *d*-spacing (Panel A) and radius (Panel B) of the DTE-PEG library. *d*-spacing and radius both increase as PEG molecular weight is increased. *d*-spacing and radius initially decrease, then remain constant from 20% to 40% PEG, indicating that domains become smaller, closer together, and more numerous. PEG_{100}-containing polymers are omitted from the graphs because of their lack of scattering as described previously.

4.2.3. Protein adsorption:

Fg and BSA adsorption as measured by QCM-D for the series of DTE-PEG polymers is presented in Figure 4.3. Protein adsorption is consistently high for PEG_{100} polymers for both BSA and Fg, regardless of the weight % of PEG. The explanation for this phenomenon is described in Figure 3.14. The lowest amount of protein adsorption for both BSA and Fg was observed in polymers containing PEG with intermediate molecular weights of 1k, 2k, and 8k. On the other hand, polymers with high PEG molecular weights of 20k and 35k showed inconsistent protein adsorption behavior. For example, 20-20k and 30-35k showed higher protein adsorption than that seen by the polymers with intermediate block lengths, while others such as 30-20k and 40-35k were repellent. Trends between BSA and Fg were identical among the different polymers in the set, suggesting that the adsorption properties of the polymers are not sensitive to protein dimensions. In other words, the smaller protein, BSA, did not exhibit a higher affinity for materials with larger phase separation features, i.e. the PEG_{20k} and PEG_{35k}-containing polymers. Fg and BSA show differences in adsorbed Voigt mass on each surface because of the disparity in molecular weight between the two proteins (340 kDa for Fg, 65 kDa for BSA).

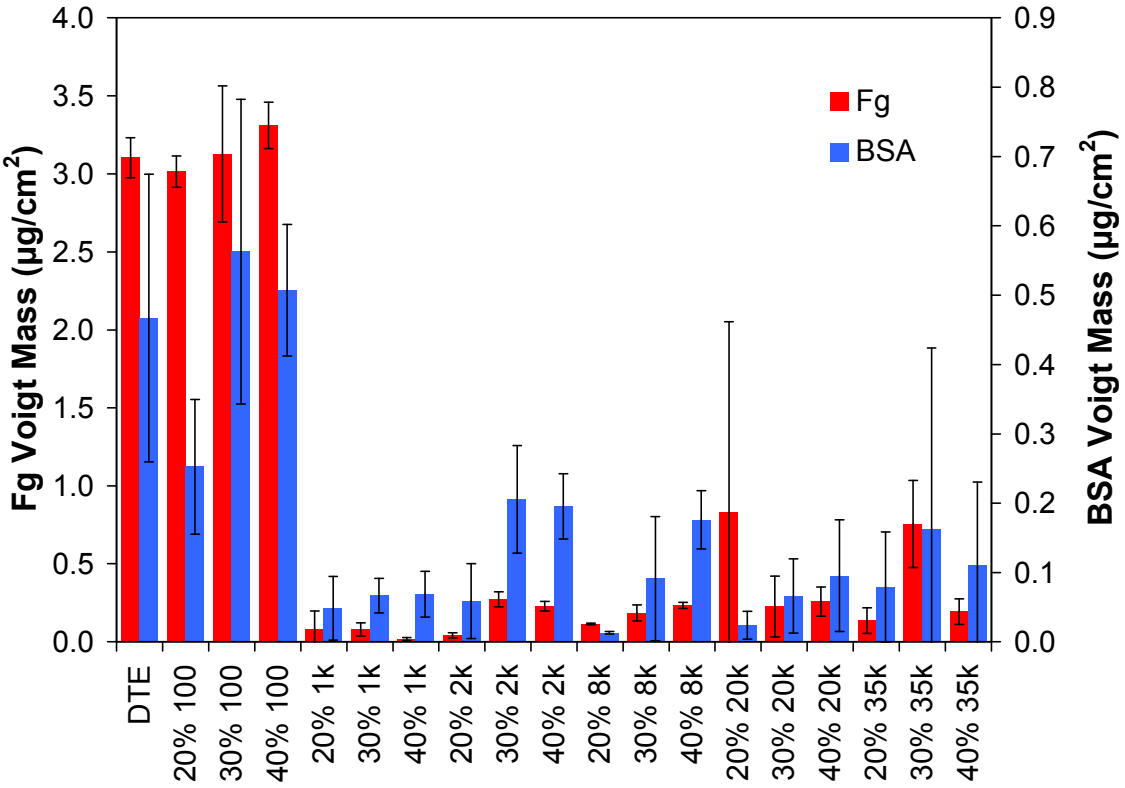

Figure 4.3 – Voigt mass-measured protein adsorption for fibrinogen (red bars) and BSA (blue bars) on a series of DTE-PEG polymers. Error bars represent standard deviation. Polymers are named by wt% PEG-MW PEG, e.g. Poly(DTE-*co*-20wt% PEG_{2k} carbonate) = 20-2k. The DTE carbonate homopolymer and PEG_{100}-containing polymers show high protein adsorption, polymers with PEG_{1k}, PEG_{2k}, and PEG_{8k} show overall protein repellence, while polymers with PEG_{20k} and PEG_{35k} show inconsistent protein adsorption. No relationship between phase separation and protein dimensions was observed.

In particular, 20-20k showed significantly different behavior between experiments. Shortly after synthesis, this polymer adsorbed large amounts of protein, as evidenced by large frequency and dissipation shifts (Figure 4.4a). However, after approximately 30 days, the sample was measured again, and showed much smaller shifts (Figure 4.4b). BSA adsorption was also performed for 20-20k after this 30 day period, and also showed negligible amounts of protein adsorbed to the surface. No notable changes in polymer structure were observed by NMR, though a slight decrease in molecular weight was seen (432 kDa after synthesis vs. 369 kDa after 1 month, M_w).

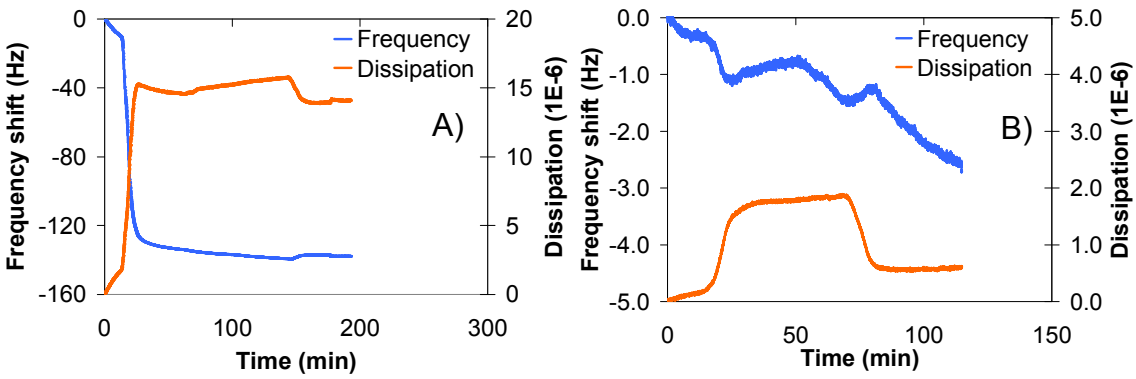

Figure 4.4 – Raw QCM-D data for 20% PEG_{20k}, shortly after synthesis (Panel A), and after 1 month in storage (Panel B). Note differences in scale of frequency shift and dissipation axes. Panel A represents an adsorbed Voigt mass of approximately 2800 ng/cm^2 (modeled as described in Section 2.6.1), while Panel B shows adsorption of about 96 ng/cm^2.

4.2.4. Fractionation and characterization of 20-20k

To investigate the possibility that polymer molecular weight could affect protein adsorption, polymers were fractionated to separate high molecular weight portions of the polymer from lower molecular weight chains that may serve as potential plasticizers. During fractionation, a non-solvent is added to a concentrated polymer solution to precipitate the polymer. High molecular weight polymer chains will precipitate first while lower molecular weight chains stay in solution. By decanting the unprecipitated supernatant and repeating the process, one can obtain a series of polymers that are separated by molecular weight and polydispersity. Early, high molecular weight fractions were assumed to be similar to the starting as-synthesized polymers. Eight fractions were generated as described in Section 2.4.3. Briefly reviewing the method, polymers were dissolved in THF, then reprecipitated with IPA. The first fraction generated is named F1, the second fraction F2, etc. The F1 fraction was then fractionated into four other "subfractions," F1-1, F1-2, F1-3, and F1-4.

Figure 4.5 shows the weight average molecular weight of fractions for 20-20k. F1 and F3 were not tested due to a lack of material. Therefore, no clear trend can be established for F1 through F4. However, F1-1 through F1-4 show that molecular weight decreases as additional polymer chains are precipitated. Polydispersity is relatively constant from F1-1 to F1-3, but increases dramatically for F1-4, indicating that this fraction contains a large amount of low molecular weight oligomers along with some longer chains.

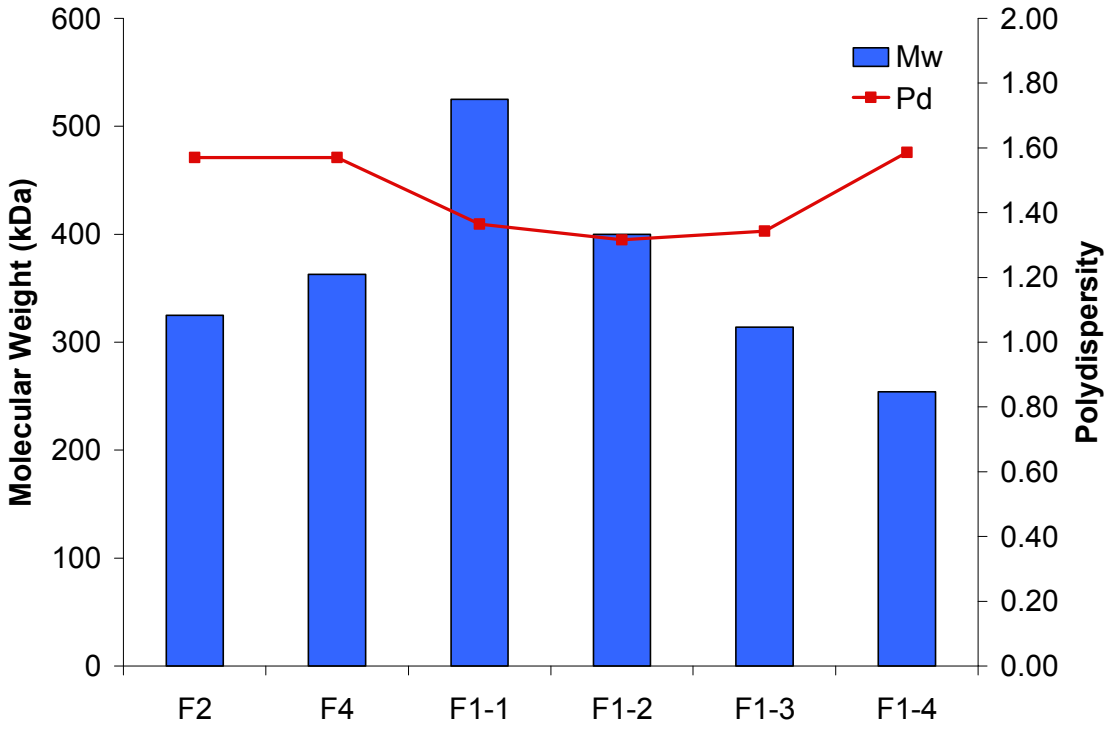

Figure 4.5 – Weight average molecular weight and polydispersity of the 20-20k series of polymers. F1 and F3 were not run because a sufficient amount of sample could not be recovered from the fractionation process.

Fibrinogen adsorption for the first four fractions of polymer, shown in Figure 4.6, was relatively low, with results comparable to most of the 1k, 2k, and 8k samples seen in Figure 4.3. However, after further fractionation, samples F1-1 and F1-2 showed

significantly larger amounts of adsorption relative to both the first set of fractions and the F1 "parent" sample. Surprisingly, the PEG concentration of the 20-20k series varied greatly as additional fractions were prepared. F1 contained only 9.5wt% PEG, whereas F2, F3, and F4 contained 18%, 39%, and 21% by weight, respectively. Similarly, the additional fractions derived from F1 showed weight % compositions of 8.3%, 11%, 16%, and 29%, respectively. Despite having identical amounts of PEG compared to F1, the F1-1 and F1-2 fractions adsorbed much larger amounts of protein, showing that protein adsorption is not a function of PEG content alone.

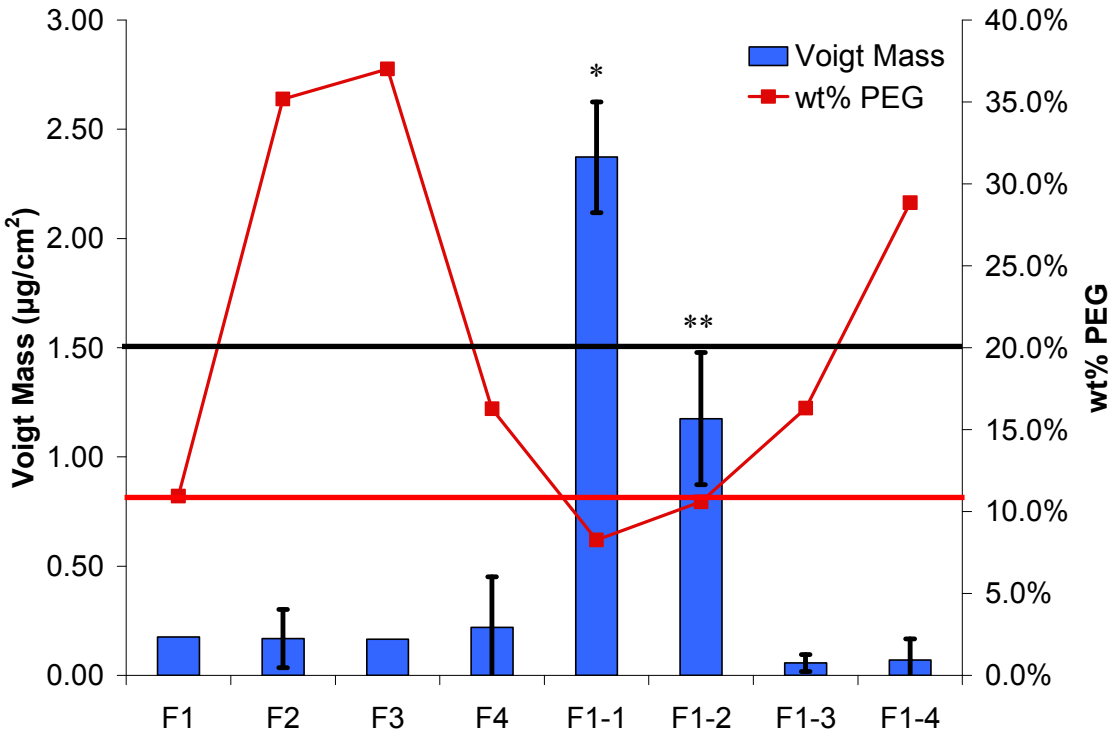

Figure 4.6 – Protein adsorption and weight % PEG for 20-20k. Error bars represent standard deviation. n < 3 for F1 and F3 due to small amounts of sample after fractionation. *: $p < 0.05$ for all other samples. **: $p < 0.05$ for all other samples except F2 and F4. Black line – expected weight % PEG across all fractions. Red line – drawn to guide the eye between F1 and F1-2. Protein adsorption is similar for F1 and F1-2 despite the similar amount of PEG in each fraction.

Figure 4.6 indicates that earlier fractions contain DTE-rich polymer chains, while later chains are PEG-rich. The following explanation is proposed for the composition discrepancies: assuming identical affinities for hydroxyl groups during polymerization, high molecular weight PEGs are present in extremely small molar ratios in solution. For example, in DTE-PEGs, 20 wt% of PEG_{20k} is equivalent to only 0.44 mol% of PEG_{20k}. Therefore, for a hypothetical 100 kDa chain, one can expect there to be on average only a single PEG_{20k} molecule in 20-20k. Because of the random copolymerization scheme, several polymer chains will be without a PEG molecule altogether, and an extremely small percentage will have multiple PEG molecules.

Table 4.4 shows the amount of PEG for each fraction normalized to the weight average molecular weight as measured by GPC. The PEG weight of the average chain was determined by multiplying the M_w with the %PEG. The number of PEG_{20k} molecules per chain is then the PEG content divided by the molecular weight of PEG_{20k}. It can be immediately seen that F1-1 and F1-2 show fewer PEG_{20k} molecules per chain, even though they have higher molecular weights compared to the other fractions. This information provides a clearer picture as to why these two fractions adsorb protein, while the other fractions do not. The 2.1 PEG_{20k} molecules per chain may serve as a threshold value to determine protein repellence or protein adsorption.

Table 4.4 – Average amount of PEG present per polymer chain as determined by measured composition and molecular weight of 20-20k fractions.

Fraction	Weight avg. MW (kDa)	% PEG	PEG wt. of average chain (kDa)	# PEG_{20k} molecules per chain
F2	325	35.2%	114	5.7
F4	363	16.3%	59.1	3.0
F1-1	525	8.27%	43.4	2.2
F1-2	400	10.6%	42.4	2.1
F1-3	314	16.3%	51.2	2.6
F1-4	254	28.9%	73.3	3.7

4.2.5. Fractionation and characterization of 11.5-1k

To further prove that factors other than PEG content may drive protein adsorption, a polymer outside of the original library, 11.5-1k, was synthesized separately and characterized. 11.5-1k (5 mol% PEG_{1k}) is a material that has previously been shown to repel proteins and cells [108, 149]. Additionally, the polymer had been previously characterized through SANS as described in Section 3.2.4.1 and was shown to exhibit no phase separation. Because the molar ratio of PEG_{1k} to DTE would be significantly more than with PEG_{20k} (5 mol% vs. 0.44 mol%, respectively), the variation in PEG content should be lessened between fractions. Furthermore, the similarity in wt% between the 11.5-1k sample and some fractions of the 20-20k sample were identical (11.5 wt% PEG vs. 10.6 wt% PEG in F1-2, a protein-adsorptive fraction of 20-20k), allowing for direct comparisons. The 11.5-1k polymer was fractionated in the same way as the 20-20k sample, with four fractions precipitated first (F1, F2, F3, F4), and an additional four fractions precipitated from the F1 fraction (F1-1, F1-2, F1-3, F1-4).

Figure 4.7 shows the M_w and polydispersity of the 11.5-1k fractions. As expected, fractions that precipitated first showed higher M_w, with M_w steadily decreasing as additional polymer chains were precipitated out of solution. Polydispersity showed no clear trends between fractions, with the first set of fractions (F1 to F4) showing decreasing polydispersity at later fractions, and the second set of fractions (F1-1 to F1-4) showing a higher polydispersity at later fractions. The higher polydispersity for the higher M_w polymers (i.e. F1-1 and F1-4) suggests that a small number of low molecular weight chains may become entangled with the high molecular weight chains, causing them to precipitate sooner than normal.

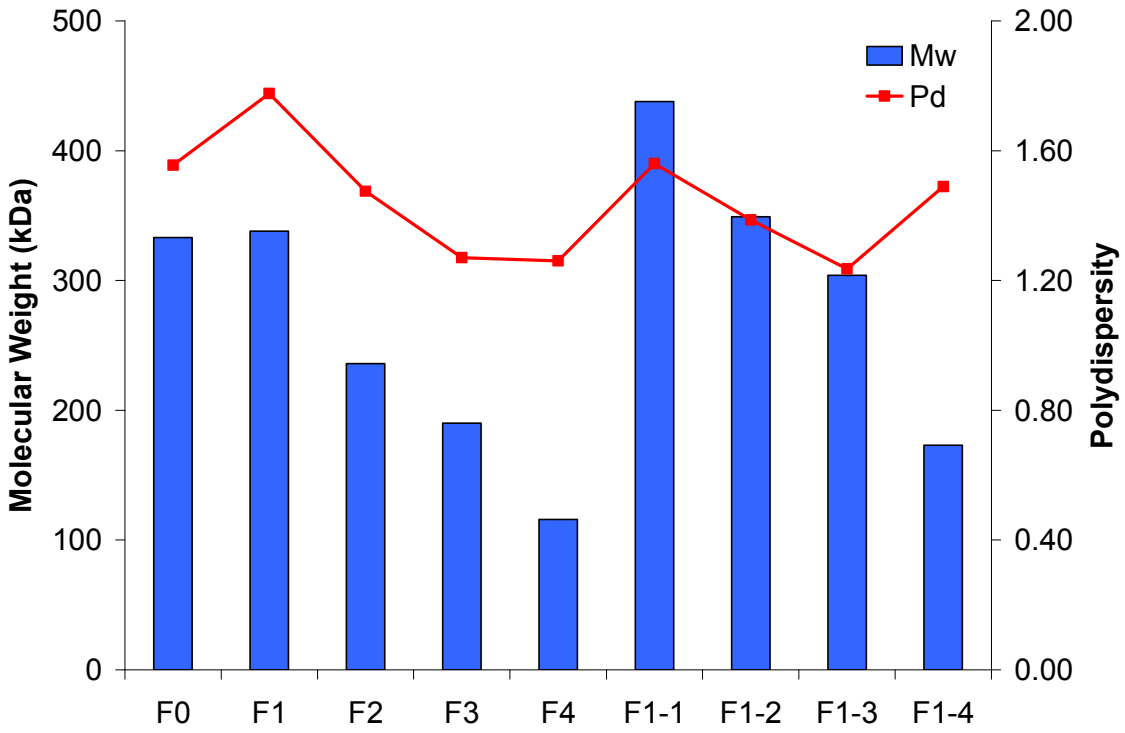

Figure 4.7 – Weight average molecular weight (blue bars) and polydispersity (red line) of fractions from 11.5-1k. F0 indicates the unfractionated as-is material.

Similar to the 20-20k fractions, the earlier fractions in the 11.5-1k series (i.e. F1, F1-1) tended to adsorb more protein than later fractions. Composition analysis by NMR showed that the eight different fractions of 11.5-1k varied in composition between 11.1% and 11.8% PEG by weight, confirming that the use of PEG_{1k} did indeed lead to less variation in PEG distribution among polymer chains (Figure 4.8). Slight variations in peak integration and normalization essentially render these differences insignificant. Despite their compositional uniformity, large variations in protein adsorption still exist between these fractions, though they do not exhibit the "all-or-nothing" behavior seen in the 20-20k fractions. In general, fractions with higher M_w showed higher protein adsorption than those with lower M_w.

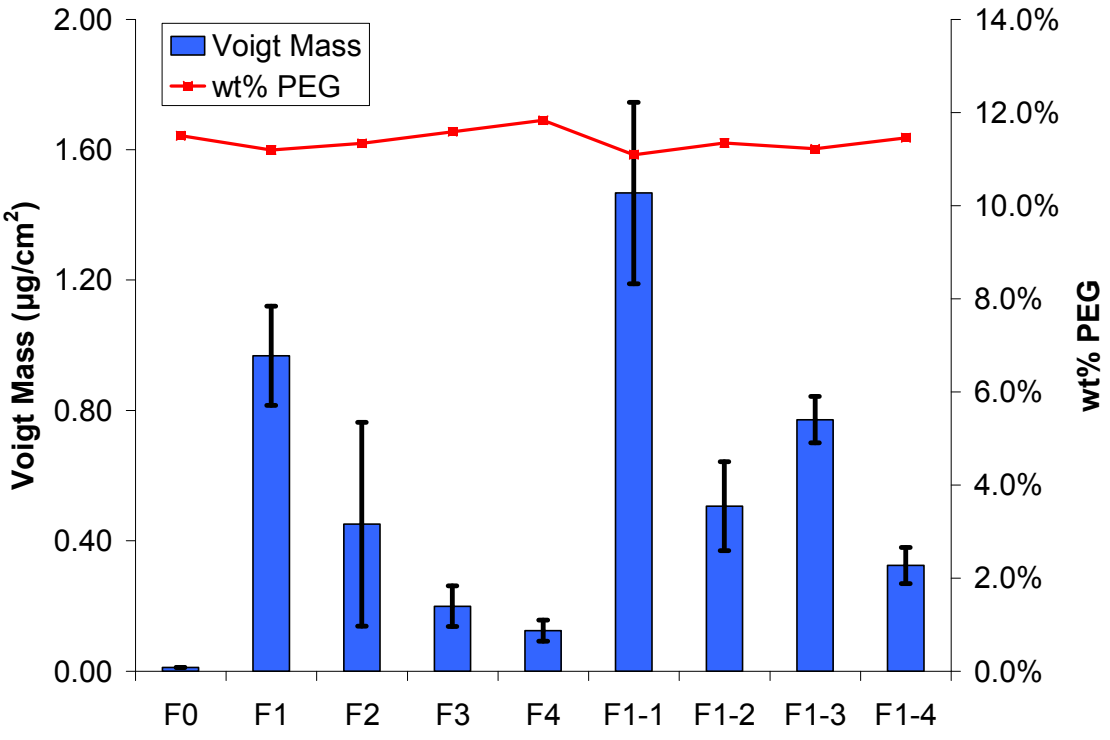

Figure 4.8 – Fibrinogen adsorption and weight % PEG in fractions of 11.5-1k. Error bars represent standard deviation. *: $p < 0.05$ for all samples except F2 and F3. **: $p < 0.05$ for all samples except for F1.

The correlation between adsorbed protein and M_w was relatively high, with R^2 = 0.82 (Figure 4.9). The correlation between adsorbed protein and M_n is weaker at R^2 = 0.63, perhaps because the smaller numbers involved increase the sensitivity of the correlation. Interestingly, fractions F1-2 and F1-3 did not follow the overall trend that higher M_w materials adsorb more protein, with F1-3 showing a higher, though insignificant, amount of protein adsorption than F1-2 on average. One main difference between the two fractions appeared to be that F1-2 had a higher polydispersity than F1-3, indicating a larger distribution of polymer chain lengths in F1-2. The results suggest that polydispersity as well as M_w may play a role in modulating protein adsorption, with high molecular weight, relatively monodisperse polymers being more capable of adsorbing proteins than low molecular weight, highly polydisperse polymers.

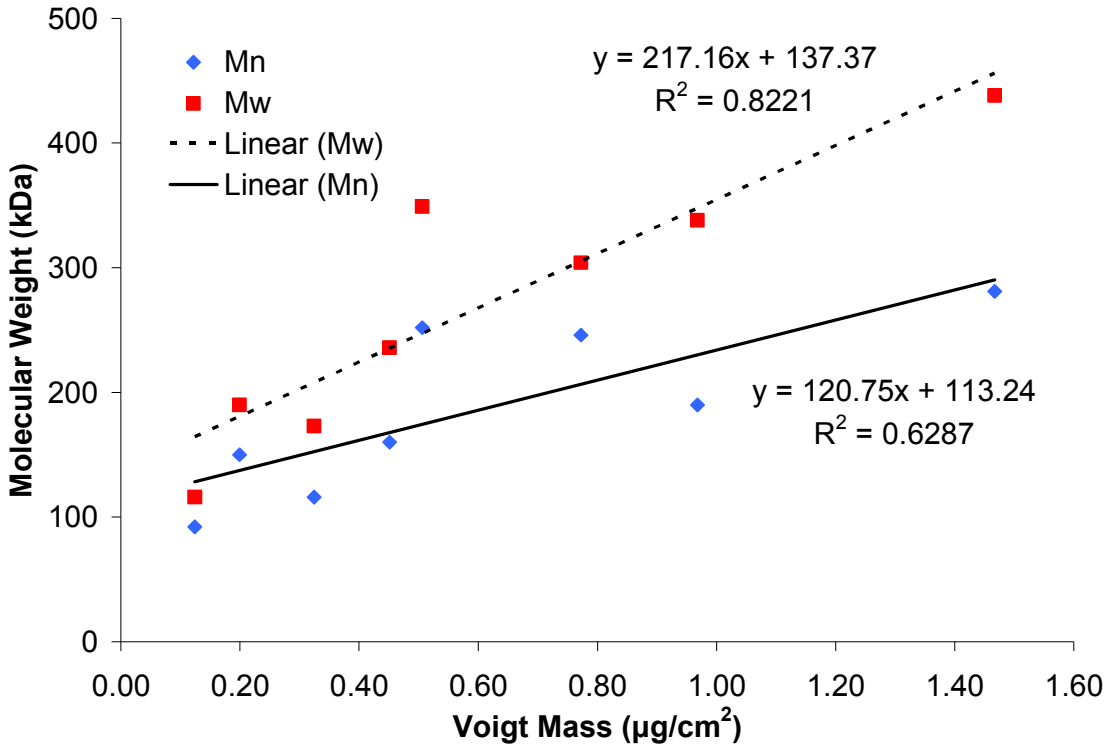

Figure 4.9 – Correlation plot between weight average molecular weight (M_w) (red squares, dotted line), number average molecular weight (M_n) (blue diamonds, solid line), and fibrinogen adsorption for 11.5-1k. Correlations between Mw and adsorbed fibrinogen are strong, with an R^2 value of 0.82.

To clearly the demonstrate the effect of polydispersity and M_w on protein adsorption, polymer fractions of 11.5-1k were blended in different ratios. These blends were first characterized by GPC to determine their general properties. The GPC chromatograms show additive properties of the two components of the blends (Figure 4.10). When compared to the values for the individual fractions, molecular weight and polydispersity show a bimodal distribution of peaks when F1-1 and F4 with polydispersities of 1.56 and 1.49, respectively, are blended at a 50/50 ratio, the polydispersity of the blend increases to 2.04, while overall M_w is approximately an average of the two fractions, with a value of 291 kDa. A 50/50 blend of F1-1 and F1-2 shows the same "averaging" effect with its M_w at 371 kDa, from 438 kDa and 349 kDa. Polydispersity averages to 1.43 for the blend, compared to 1.56 and 1.39 for F1-1 and F1-2, respectively (Figure 4.7).

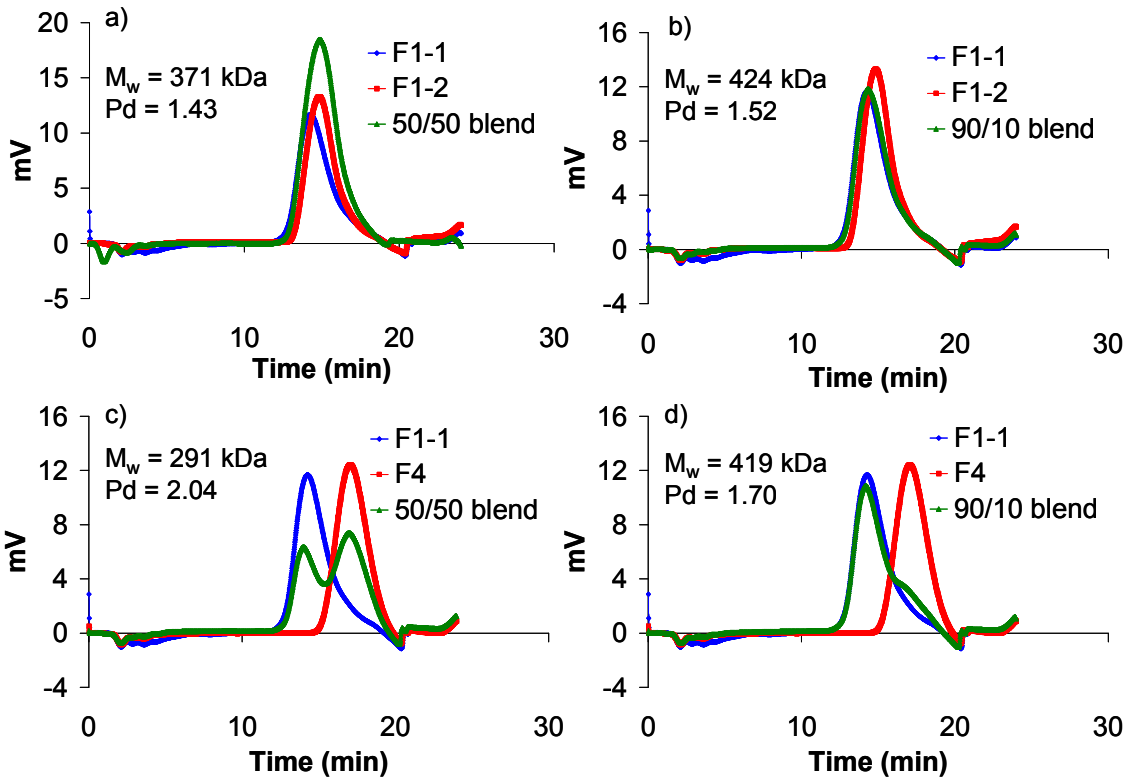

Figure 4.10 – GPC chromatograms of blends with 11.5-1k fractions. a) 50/50 blend of F1-1 and F1-2, b) 90/10 blend of F1-1 and F1-2, c) 50/50 blend of F1-1 and F4, d) 90/10 blend of F1-1 and F4. M_ws show a weighted averaging effect. Polydispersity (Pd) shows a weighted averaging effect for blends of F1-1 and F1-2, while Pd is increased when F1-1 is blended with F4 due to the appearance of multiple peaks or a shoulder for the 50/50 blend and the 90/10 blend, respectively.

QCM-D was then used to measure the protein adsorption capabilities of these polymer blends, with Fg used as the test protein. Figure 4.11 displays the results of blending various fractions on fibrinogen adsorption. A 50/50 blend of a highly adsorptive fraction, F1-1, and a non-adsorptive fraction, F4, resulted in almost complete protein repellence. Blending F1-1 and F4 in a 90/10 ratio resulted in an approximately 50% decrease in fibrinogen adsorption compared to F1-1 alone. To see what the sensitivity of the system to these perturbations in molecular weight and polydispersity were examined by blending two relatively highly adsorptive fractions. Surprisingly, even a 50/50 blend of F1-1 and F1-2 resulted in a large amount of protein repellence. The amount of protein

adsorbed for the blend was only 0.28 μg/cm^2, well below both the 0.51 μg/cm^2 adsorbed by F1-2 alone and the 1.47 μg/cm2 adsorbed by F1-1 alone (Figure 10). Even blending F1-1 and F1-2 in a 90/10 ratio resulted in a similar (≈50%) amount of protein adsorption reduction as blending F1-1 and F4.

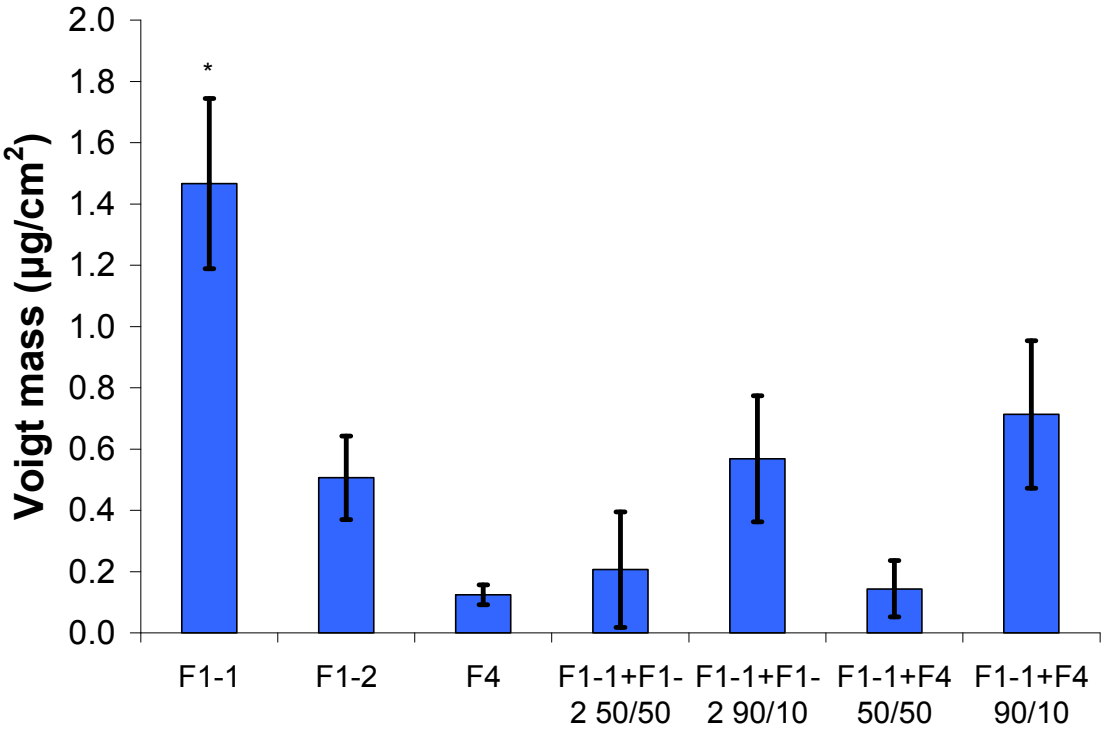

Figure 4.11 – QCM-D results of Fg adsorption onto blends of fractions of 11.5-1k. Error bars represent standard deviation. * - p > 0.05 compared to all other samples. Fg adsorption does not show a weighted average between blends, as blending with just 10% of another fraction reduces protein adsorption by 50% compared to F1-1, regardless of the fraction used. Blending with a 50/50 ratio further decreases Fg adsorption

One possible explanation for the observed protein repellence observed upon blending different fractions is that the introduction of new chains with different sizes disrupts the phase separation behavior. Having a large number of chains with high molecular weight gives a higher chance for phase separation, as long chains are better

suited to forming microdomains than shorter chains [80]. The results suggest that the introduction of a portion of shorter chains disrupts this domain formation, and instead PEG becomes uniformly distributed along the surface, thereby reducing protein adsorption. Attempts to determine protein adsorption behavior through direct comparisons with molecular weight and polydispersity may apply when the polymers are as-is, but become less reliable as these parameters are perturbed through the introduction of new polymer chains with different physical (but not necessarily compositional) characteristics. For example, the 90/10 blends of F1-1 with F1-2 and F4 for 11.5% PEG_{1k} each have M_ws that should correspond to 1.1-1.3 μg/cm^2 as seen in Figure 4.9, but this is not the case.

Polydispersity also appears to have a role in protein adsorption behavior based on results for F1-2 and F1-3 in Figure 4.8. However, polydispersity alone does not tell the whole story, as 90/10 blends of F1-1 with both F1-2 and F4 both show almost complete protein repellence, despite relatively similar numbers reported through GPC (Figure 4.10). It appears that that the actual molecular chain distribution is also a contributing factor to protein repellence than simply the measurement of polydispersity alone. The polydispersity reading from GPC does not necessarily provide this information. For example, in the case of a polymer blend, if the chains from one polymer are within the distribution of the other polymer, polydispersity does not appear to change much, i.e. the GPC chromatogram will still give a reading of a material with a single, relatively undisturbed peak (see Figure 4.10a). However, there now exists essentially a bimodal distribution of polymer chains: ones containing predominantly the original molecular weight, and ones containing predominantly the blended molecular weight. Protein

adsorption results seem to indicate that this disruption of chain distribution is capable of reducing protein adsorption (Figure 4.11). It is possible that the mechanism for protein adsorption is based in the morphology of the polymer. As described in Chapter 3, SANS cannot detect distinct clusters of water in the bulk of a material for DTE-PEG polymers containing 11.5 wt% PEG or less, but contact angle measurements are sensitive to the uniformity of the surface.

4.2.6. Contact angle and surface energy analysis

Contact angle measurements are typically used to gauge the hydrophobicity, hydrophilicity, and surface energy of a material surface [43, 139-141, 175-177]. By placing a drop of liquid, usually water, onto a surface, the angle made by the drop provides information about the affinity of the liquid for the surface (Figure 4.12).

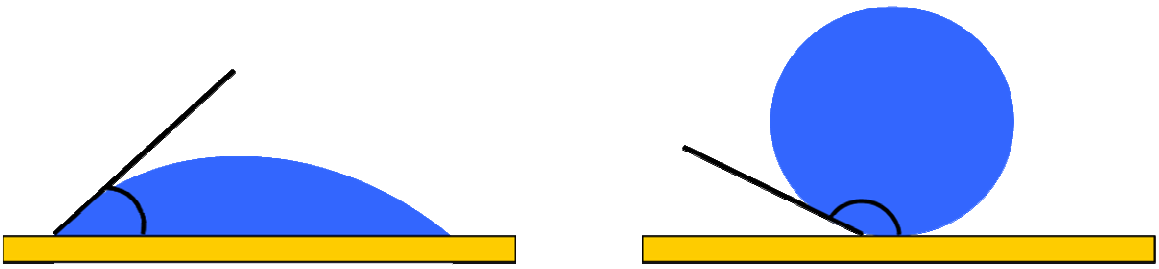

Figure 4.12 – A schematic of contact angle measurements of wetting (left) and non-wetting (right) surfaces.

As a drop is deposited, its edges advance along the surface. Measurement of the contact angle during this process is known as the advancing contact angle, θ_a. The drop can also be retracted, which will cause the liquid to retreat along the surface. A contact angle measurement during this process is known as the receding contact angle, θ_r. Under

ideal conditions, the advancing and receding contact angles should be exactly the same. However, surface roughness, contaminants, and "patchiness" from morphological features can all affect the lateral movement of the drop across the surface. In particular, phase separation can generate features on the surface of a material that can cause droplets to deviate from ideal behavior [139, 176]. This concept is illustrated in Figure 4.13.

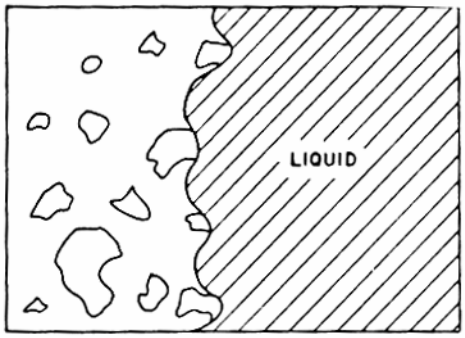

Figure 4.13 – A schematic of how liquid spreading is affected by morphological features. The movement of the drop along the surface can be impeded by high or low energy features during its advancing or receding motion. Image reproduced from with permission from [139]. Copyright owners: Springer Science and Business Media.

The results from Section 4.2.5 suggest that a morphological mechanism may play a role in modulating protein adsorption, even when the composition between fractions is similar. Based on the low amount of material needed (3-5 mg for spin coating solutions) and possible sensitivity towards surface features, contact angle hysteresis measurements were used to determine the presence of phase separation.

Contact angle measurement is also a simple, straightforward method of determining the surface energy of a substrate. Surface energy has been linked to relevant biological properties such as protein adsorption and cell spreading [43, 178]. Several methods exist for determining surface energy, and the reader is directed towards [140] and [141] for excellent reviews on each method. The Fowkes approximation is chosen for this study because of its relative ease-of-use and ability to generate surface energy values

based on characteristics of several different probe liquids. The method for determining surface energy is described in Section 2.8.

A sample graph showing the trendline for the three probe liquids is shown in Figure 4.14. The tabulated results for all contact angle analyses are given in Table 4.5. Not all samples could be tested due to the low amounts of polymer remaining after previous characterization. While the R^2 correlation between the three probe liquids is not ideal, it should be noted that the resulting surface energy for each sample varies very little. This was the result of the individual probe liquid contact angles varying indistinguishably between samples, rather than the numbers coming together through coincidence. The identical surface energy for each substrate is likely a function of the overall composition of the surface, because the drop area is large enough that it can "sample" the composition of the substrate sufficiently. Because the composition of the DTE and PEG are relatively similar between fractions (see Figure 4.8), surface energy remains constant.

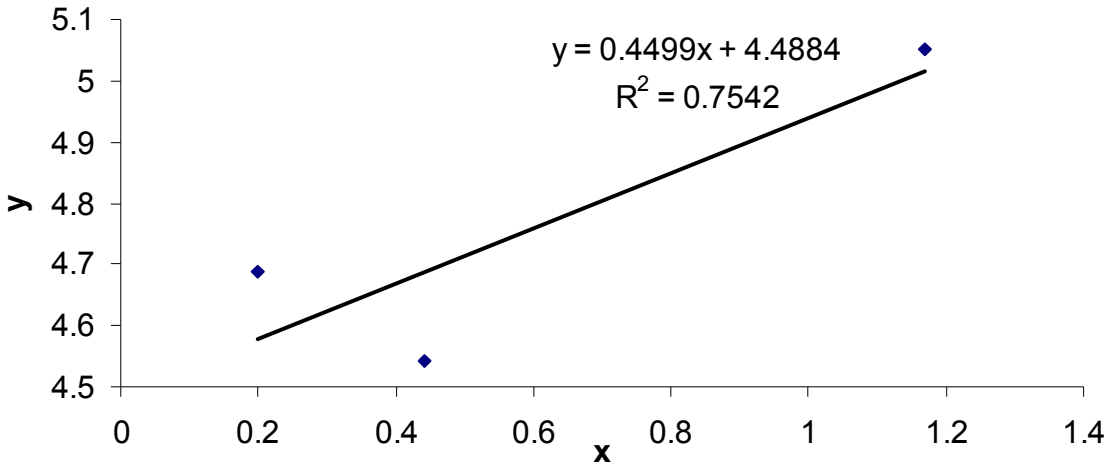

Figure 4.14 – A sample fit of the x and y parameters for the Fowkes approximation in determining surface energy. The slope and intercept of the linear fit are used to calculate the surface energy.

Table 4.5 – Contact angle measurement results for fractions of 11.5-1k and poly(DTE carbonate). Surface energy of poly(DTE carbonate) was not measured.

	DTE	F0	F2	F3	F4	F1-1	F1-2	F1-4
Water Hysteresis (°)	16.3	17.0	24.5	24.1	26.2	24.3	25.1	24.8
Hysteresis st. dev. (°)	3.05	4.59	2.89	1.97	2.36	2.02	1.98	1.79
Slope		0.48	0.44	0.45	0.44	0.41	0.41	0.47
Intercept		4.55	4.48	4.49	4.48	4.51	4.55	4.49
Free Energy (mJ/m^2)		20.9	20.3	20.4	20.3	20.5	20.8	20.3

By comparison, contact angle hysteresis, shown in Figure 4.15, is significantly lower for the as-is 11.5-1k material (F0) when compared to the other fractions. This result shows that the surface for the as-is material is more homogeneous compared to the fractionated materials. It should be noted that the advancing angles for all the samples were very identical, but the receding angle for the as-is material was greater on average. This indicates that the high-energy regions, i.e. wetting regions, prevent the drop from receding once they have been wetted [176]. A uniform distribution of these high-energy phases would be better-suited to prevent receding than patchy domains of high-energy and (predominantly) low-energy regions. The morphological uniformity of the 11.5-1k as-is surface is further reinforced when compared to poly(DTE carbonate).

When the contact angle hysteresis data is compared alongside the fibrinogen adsorption data, it appears that the relative uniformity of the as-is material presents a surface such that proteins are unable to adsorb. Once the materials become fractionated, however, the hysteresis between the fractions is not significantly different, even though their protein adsorption capabilities are clearly different. In short, contact angle hysteresis measurements can identify the non-adsorptive material, but cannot determine how much protein an adsorptive material will adsorb.

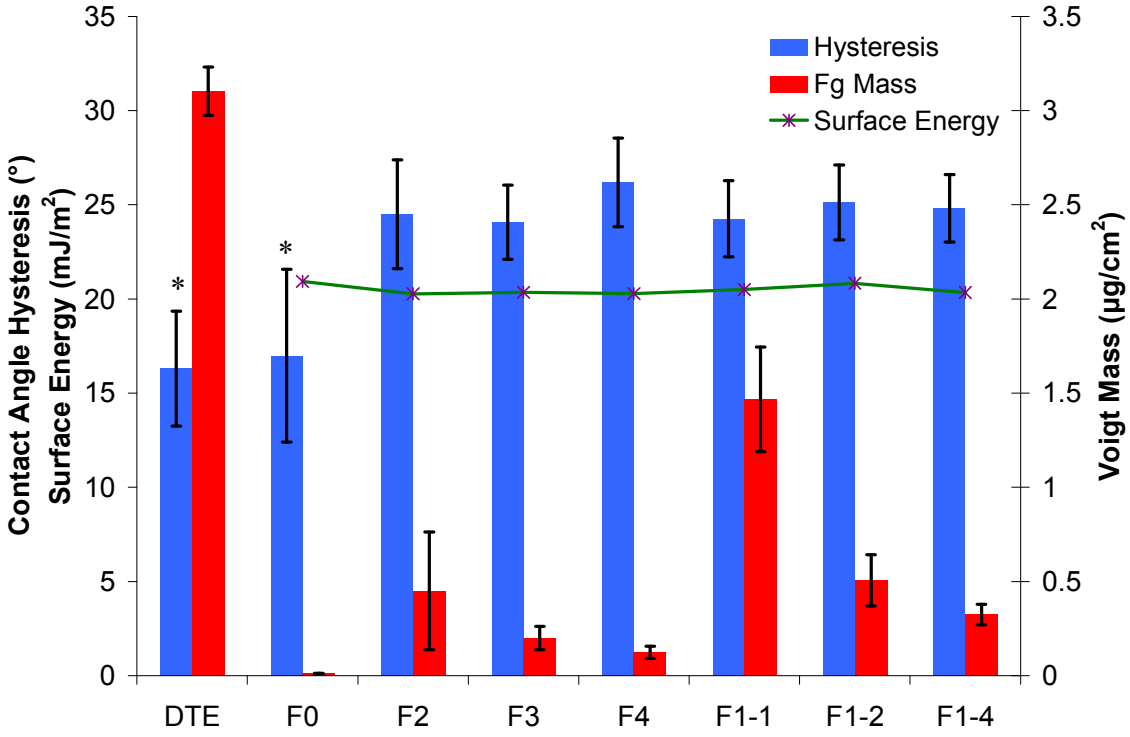

Figure 4.15 – Contact angle hysteresis, surface energy, and fibrinogen adsorption for poly(DTE carbonate) and fractions of 11.5-1k. Error bars represent standard deviation. *: $p < 0.05$ vs. all other samples for contact angle hysteresis. Surface energy was not measured for poly(DTE carbonate). While surface energy is relatively constant between each 11.5-1k material, hysteresis varies significantly between the "as is" polymer and the fractions, suggesting that PEG is more homogeneously distributed on the surface of the "as is" polymer.

4.3. Conclusions

The general relationships between PEG molecular weight, weight % of PEG, phase separation, and protein adsorption were examined in a series of random multiblock DTE-PEG polymers. This work represents one of the first attempts to investigate how these macromolecular factors may affect protein adsorption. The following conclusions were reached: at high PEG wt% (40% or greater), surfaces are protein-repellent,

regardless of the PEG molecular weight. For low PEG molecular weights (~ 100 Da), protein adsorption occurs even at high PEG contents, because low molecular weight PEG lacks the water association properties of their higher molecular weight counterparts. For PEG_{1k}, the transition point for protein adsorption appears to occur at around 10-18wt% PEG_{1k}, as PEG concentrations above this value will be able to consistently repel proteins. For polymers with PEG molecular weights of 20 kDa or greater, protein adsorption may still occur at slightly higher PEG concentrations due to larger separation of PEG domains, i.e. greater amounts of phase separation. At these transition compositions, other currently unknown factors, such as material processing and humidity, may greatly affect the results obtained for protein adsorption. Fractionation of polymers with low PEG wt% and large PEG molecular weights can result in fractions that have high variation in composition.

It is also demonstrated that for the 11.5-1k polymer, protein adsorption can be modulated by manipulating molecular weight, polydispersity, and PEG block size. Fractions of 11.5-1k displayed large variability in protein adsorption, despite the fact that compositions were relatively similar. Contact angle hysteresis measurements showed that the fractions of 11.5-1k had significantly more hysteresis than the as-is sample, suggesting that surface heterogeneity and phase separation may be occurring with the fractionated polymers. These results provide additional insight into control parameters for the design of biomedical devices, and should be taken into account when manufacturing materials that come in contact with proteinaceous fluids.

5. Cell response on phase-separated, DTE-PEG polymers

Based on the manuscript: "Poly(ethylene glycol) as a sensitive regulator of cell survival fate on polymeric biomaterials: The interplay of cell adhesion- and pro-oxidant signaling mechanisms" by Hak-Joon Sung*, Arnold Luk*, Sanjeeva Murthy, Er Liu, Malasa Jois, Abraham Joy, Jared Bushman, Prabhas V. Moghe, and Joachim Kohn. * - Equal first authors. Submitted to Soft Matter.

5.1. Background

Protein adsorption dictates future cellular response by providing ligands for cells. Cell surface receptors known as integrins associate with surface proteins to form focal adhesions [95]. These associations play a role in cell signaling that govern behavior such as cell attachment, proliferation, and differentiation [96]. The integrin α5β1 complex has been specifically implicated in interactions with RGD (arginine-glycine-aspartic acid) amino acid sequences in adhesive extracellular matrix proteins such as fibronectin and fibrinogen [95, 179]. The interactions of integrin α5β1 with appropriate substrates have been specifically implicated in supporting cell survival in several cell types [180]. Conversely, cells that are unable to adhere to a substrate and remain suspended tend to undergo apoptosis, or programmed cell death [181-185].

Results shown in Chapter 4 illustrate that proteins are mostly repelled from surfaces containing both 20-40% PEG and intermediate PEG molecular weights. It then follows that these highly repellent surfaces should be more likely to prevent cell

attachment and therefore induce apoptosis. To confirm this hypothesis, SaOS-2 osteosarcoma cells were cultured onto DTE-PEG substrates containing 0-41 wt% PEG_{1k} (0-20 mol%). Both the extracellular interactions with proteins and the intracellular expression of integrin α5 was quantified to determine the affinity of cells for the substrates and the viability of the cells over time. Protein adsorption of serum components using 10% fetal bovine serum (FBS) in PBS were also studied to determine whether the amount of protein adsorption and cell attachment and survival are correlated for each substrate. The translocation of GAPDH has been previously shown to be a common indicator of apoptosis among different cell lines, and was quantified in this study to measure apoptosis in SaOS-2 cells [144].

In this chapter, all substrates are random multiblock copolymers of DTE and PEG_{1k} with the exception of control surfaces PLLA and poly(DTE carbonate). Therefore, DTE-PEG copolymers will simply be referred to by their weight % of PEG for brevity. Concentrations of PEG will be specified by weight percent instead of mol percent unless explicitly stated.

5.2. Results

5.2.1. Adsorption of serum components

QCM-D results for serum protein adsorption are shown in Figure 5.1. At 24% and 41% PEG, complete repellence is observed. The results are consistent with the known repellent properties of PEG [56-57] and with protein adsorption data in Chapter 4. Also

noteworthy is that when compared to fibrinogen adsorption in Figure 4.3, the adsorbed Voigt mass is less for FBS. Serum contains smaller proteins, such as albumin, that will compete for the surface to form a monolayer. As a result, monolayer formation of these smaller, lighter proteins results in a lower Voigt mass.

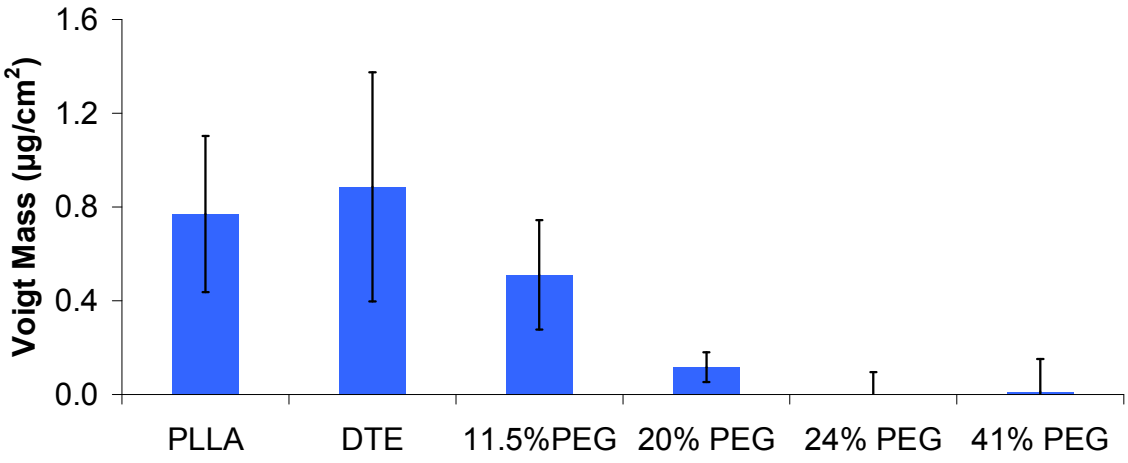

Figure 5.1 – Fetal bovine serum adsorption for DTE homopolymer, PLLA, and DTE-PEG polymers (n=3). Error bars represent standard error. Increases in PEG lower protein adsorption to negligible levels at greater than 24% PEG.

5.2.2. Cell attachment on DTE-PEG substrates

SaOS-2 cells were cultured onto spin-coated glass cover slips. After 24 hours, cells were stained with blue fluorescent Hoechst stain and imaged with fluorescence microscopy to determine the number of live cells on the surface. Cell attachment followed trends similar to serum adsorption, with fewer cells attaching to more highly PEGylated substrates, and DTE and PLLA showing identical levels of attachment (Figure 5.2).

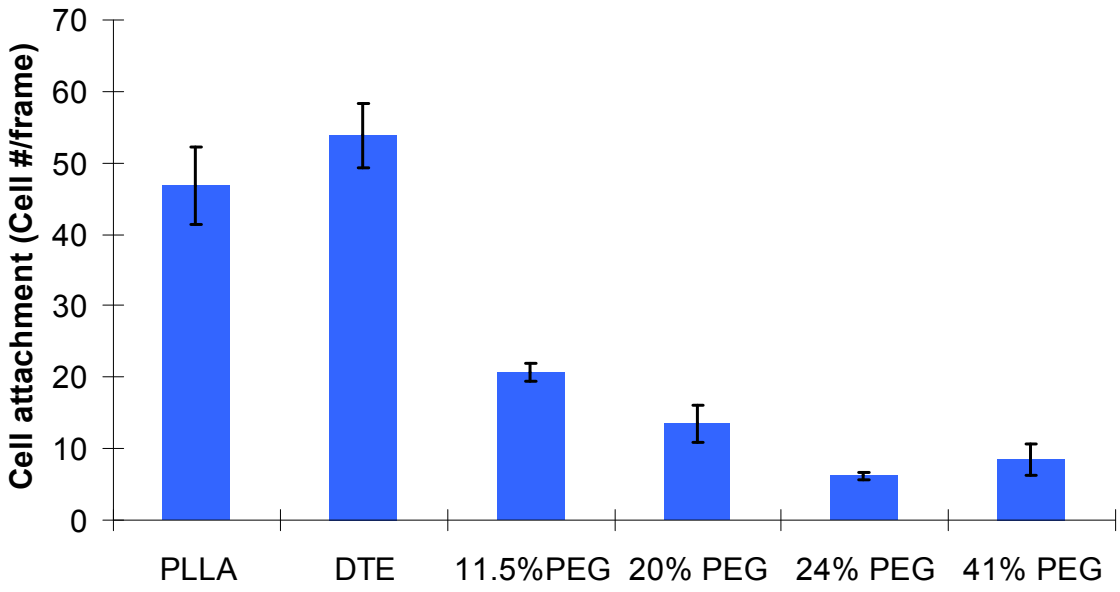

Figure 5.2 – Cell attachment of SaOS-2 cells on DTE homopolymers, PLLA, and DTE-PEG substrates (n=4). Error bars represent standard error.

5.2.3. GAPDH nuclear translocation as a measure of apoptosis on DTE-PEG substrates

While GAPDH is typically an enzyme involved in glycolysis and energy production, Dastoor et al. have shown that during apoptosis, GAPDH serves as a potential molecular chaperone during the apoptosis signaling cascade [144]. Several studies have reported that GAPDH translocalization to the nucleus is a reliable marker of apoptosis [143, 145, 186]. To determine whether cells on DTE-PEG substrates underwent apoptosis, GFP-GAPDH SaOS-2 cells were cultured onto selected spin-coated polymers. After 24 hours, green fluorescence intensity for the nucleus and cytoplasm was measured through multiphoton confocal microscopy and the ratio was calculated. The results in Figure 5.3 show that higher amounts of PEG cause GAPDH to increasingly migrate to the nucleus of the cell, indicating higher apoptotic potential for those substrates.

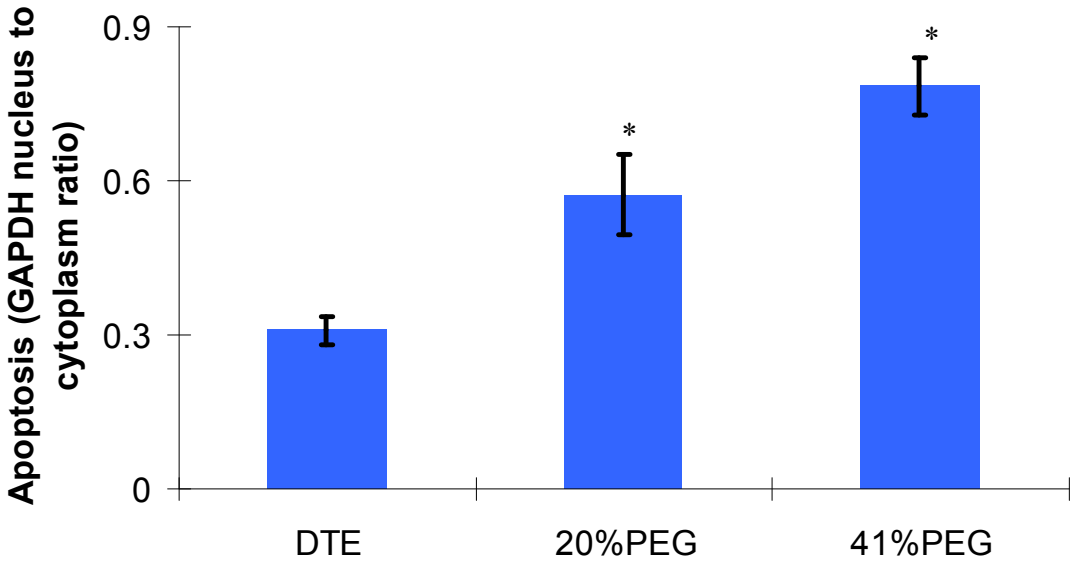

Figure 5.3 – GAPDH green fluorescence nucleus-to-cytoplasm ratio as a marker for apoptosis. Increasing amounts of PEG result in higher GAPDH nuclear translocation. Error bars represent standard error. *: $p < 0.05$ vs. DTE homopolymers.

5.2.4. Cell spreading on DTE-PEG substrates

SaOS-2 cell spreading was measured by identifying Hoechst-positive cells and determining the cell borders through a combination of fluorescent and phase contrast microscopy. In general, cell area decreased on more highly PEGylated substrates (Figure 5.4). Surprisingly, cell area was increased on the 41% PEG substrate. Even though identically few cells attach to both the 24% PEG and the 41% PEG substrate, cells that are attached to the 41% PEG substrate spread approximately three times more. These results are unexpected based on phase separation data reported in Table 3.3. The increased radius of the hydrated domains between 24% PEG and 41% PEG (4.6 nm vs. 5.1 nm) suggests that cell integrin receptors would be less likely to locate a protein-laden adhesive domain to attach onto for the 41% PEG region. Furthermore, the two surfaces

show an equal amount of protein repellence, which indicates that there are no additional ligands for the cell receptors. A possible explanation for this behavior is that a cellular compensation mechanism allows cells on the 41% PEG substrate to increase spreading.

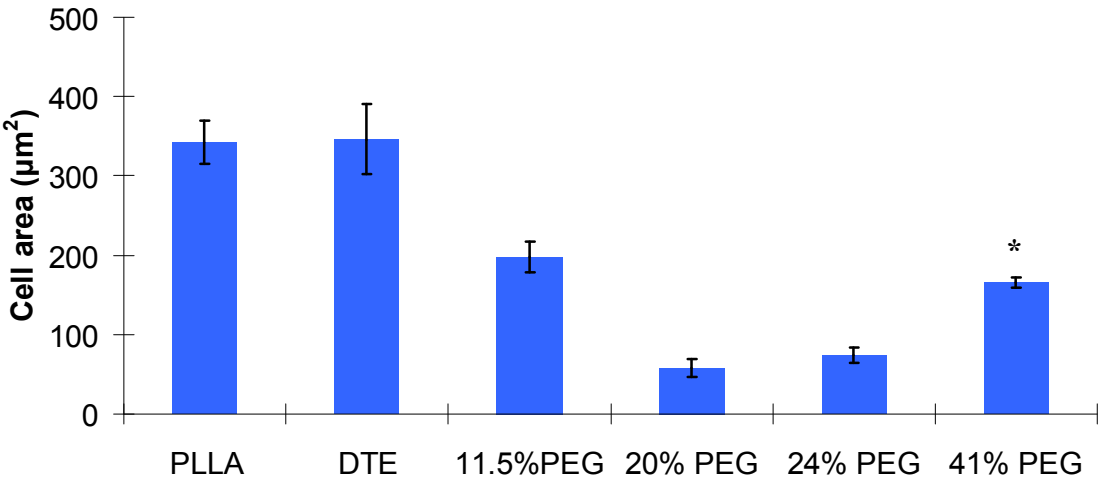

Figure 5.4 – Cell spreading of SaOS-2 cells on PEG-containing DTE polymers, DTE homopolymer, and PLLA. Error bars represent standard error. *: $p < 0.05$ vs. 20% and 24% PEG (n=16)

5.2.5. Integrin α5 spatial features and expression

To visualize the spatial distribution of integrin-α5 on phase separated surfaces, GFP-integrin-α5 SaOS-2 cells were cultured for 24 hours and imaged using a fluorescent microscope. For 20% PEG, cells are relatively confined, and integrin-α5 is concentrated by the center of the cell. However, for 41% PEG, integrin-α5 is located both in the center and along the periphery of the cell, allowing the cell to spread on the substrate (Figure 5.5). The phase separation dimensions for 20% PEG1k are given in Table 4.3 as 13.3 nm *d*-spacing, 5.32 nm domain radius, and 0.43 fractional deviation. On the other hand, 41% PEG shows a 14.8 nm *d*-spacing, 5.14 nm radius, and a 0.26 fractional deviation (Table

3.3). The fact that the domains are smaller and farther apart for 41% PEG suggests that ligands may occasionally find a hydrophobic patch onto which they can adsorb, as described in Figure 3.15. The overall high concentration of PEG, however, may cause these ligands to be fairly remote, causing cells to spread out to find appropriate integrin binding sites. The system may bear some similarities to systems previously designed by Chen et al., where posts of ligands increase the surface area for cells, while keeping the overall ligand density relatively constant [187].

The idea that a polymer with higher amounts of PEG has larger hydrophobic patches to allow protein binding runs counter to the SANS figures. However, one must also consider that the fractional deviation for 41% PEG is much lower than that seen for 20% PEG, which suggests that the domain spacings occur much more regularly for 41% PEG. The higher fractional deviation for 20% PEG indicates an "all-or-nothing" behavior for adsorbed proteins, where a large hydrophobic patch may open up and allow proteins to adsorb, while other regions may have a high concentration of repellent, PEGylated domains. The large hydrophobic patches in conjunction with highly PEGylated regions may be the cause of localization of integrin α5 around the nucleus of the cell, in conjunction with the relatively poor spreading seen on the 20% PEG surface.

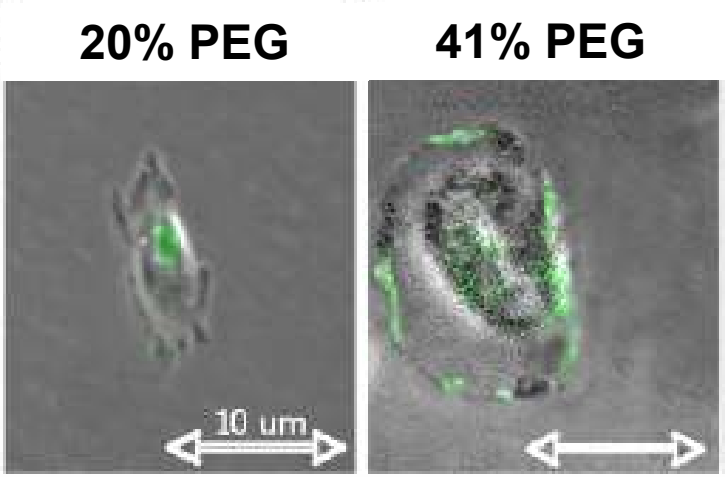

Figure 5.5 – Representative samples of cell spreading and integrin α5 localization of GFP-integrin α5 SaOS-2 cells.

To quantify extracellular expression, integrin α5 proteins were immunostained and imaged with fluorescent microscopy. When normalized to cell area, integrin α5 expression on the "nonadhesive" surfaces, 20%, 24%, and 41% PEG show similar amounts of integrin α5 (Figure 5.6). However, the normalized value for 41% PEG indicates that the amount of integrin α5 expressed for those cells was approximately three times higher than the values for 20% and 24% PEG because of the larger cell area reported in Figure 5.4.

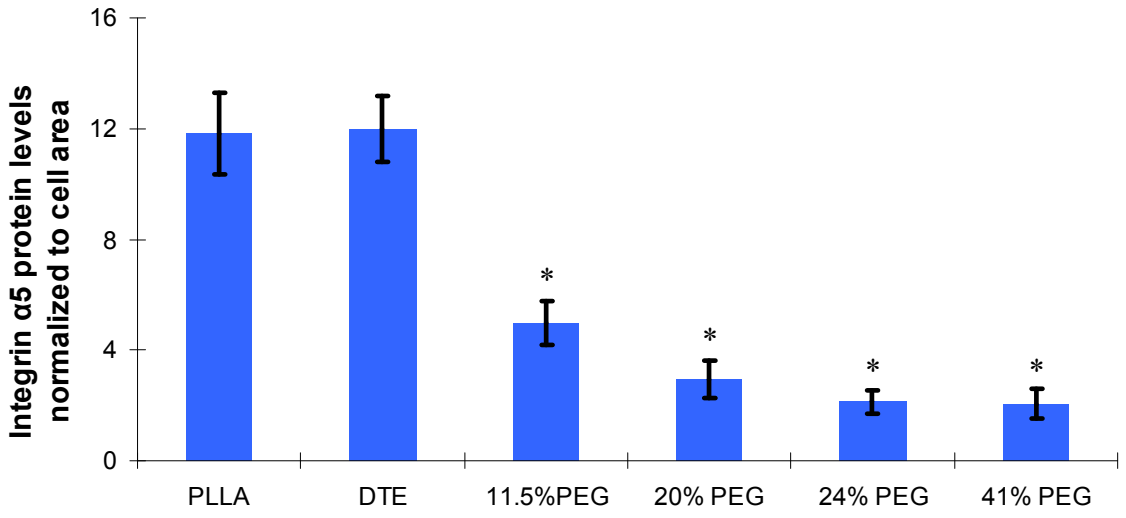

Figure 5.6 – Immunostained integrin α5 protein levels normalized to cell area. (n=25). Error bars represent standard error. *: p <0.05 vs. DTE homopolymers.

5.2.6. Detection of intracellular integrin α5 mRNA through fluorescence in situ hybridization (FISH)

The data presented above strongly suggest that anchorage-dependent cells compensate for their substrates by upregulating adhesive proteins such as integrins. Additionally, a threshold amount of PEG appears to be required before this response is initiated. To further reinforce this point, two experiments were performed by Er Liu and Dr. Jared Bushman that focused on upstream production and signaling for the expression of integrin α5 on the cell surface.

Fluorescence in situ hybridization (FISH) was performed to determine the level of integrin α5 mRNA expression in SaOS-2 cells. A higher amount of mRNA expression indicates that a cell is attempting to produce greater amounts of the integrin α5 protein, regardless of the amount of actual protein that may be expressed on the cell membrane or in the cytoplasm. A fish sperm mRNA probe specific for integrin α5 was incubated with

the cells for 16 hours and imaged using fluorescence microscopy. The results in Figure 5.7 show that the amount of integrin α5 mRNA expressed is highest for the DTE homopolymers, but is greatly decreased for 20% PEG. However, the amount of integrin α5 transcribed in 41% PEG is higher than that seen for 20% PEG, confirming the upregulation of the adhesive protein.

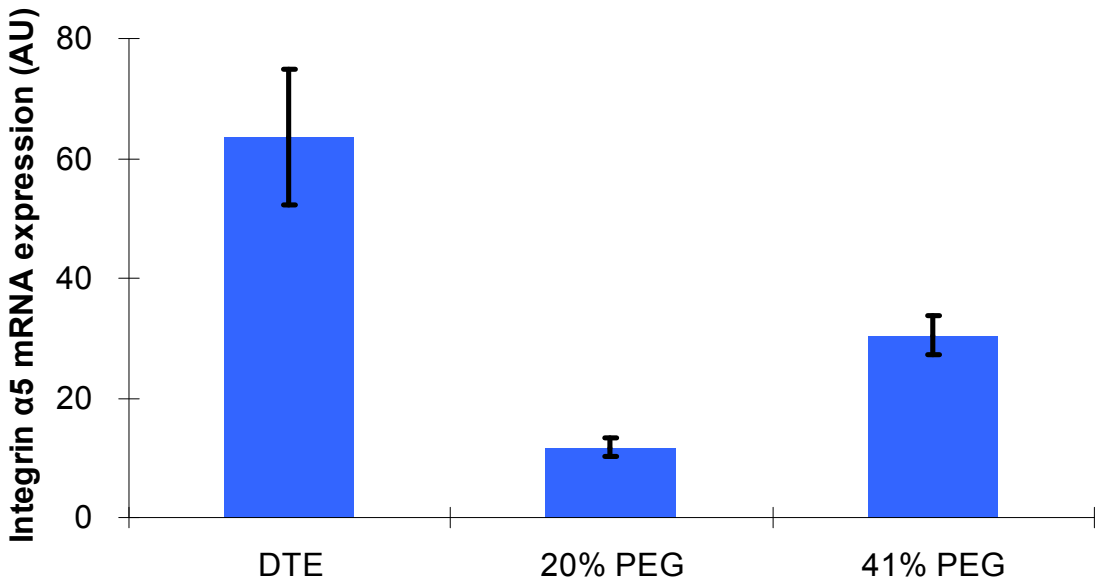

Figure 5.7 – In situ hybridization for expression of mRNA. Error bars represent standard error. All polymers are significantly different from each other, $p < 0.05$.

5.2.7. Dynamic upregulation of integrin α5 measured through quantitative polymerase chain reaction (QPCR)

The integrin α5 quantification experiments performed in the previous three sections examined attached cells at a single 24 hour time point. However, with those experiments alone, it is possible that upregulation was due to selection imposed by the substrate for abnormally adherent cells within the population, rather than cell-substrate interactions. To rule out this possibility, mRNA expression of integrin α5 was compared

for SaOS-2 cells at 4 hours and 24 hours using quantitative polymerase chain reaction (QPCR). If abnormally adherent cells were attached at 4 hours, they would already express a relatively high level of integrin α5, and at 24 hours, additional expression would be comparatively minimal. Conversely, if cells adapt to surfaces over time, a higher amount of integrin α5 should be observed.

At each time point, RNA was harvested from cultured cells and amplified. GAPDH was selected as a housekeeping gene. The ratios between 24 hour and 4 hour integrin α5 expression are shown in Figure 5.8. Integrin α5 expression was actually downregulated at 24 hours for the DTE homopolymer and 11.5% PEG. For 20% PEG, integrin α5 levels for the cells remained relatively constant at both time points. By comparison, cells on the 24% and 41% PEG substrates significantly upregulated integrin α5 relative to their 4 hour timepoint. Therefore, cells on surfaces with higher amounts of PEG responded dynamically to the surface, and the increased amount of PEG directly caused them to increase production of integrin α5. While few cells attached initially, the ones that remain attached increased integrin α5 expression, allowing them to produce excess integrin receptors, find scarce ligands more easily, and spread significantly more on highly PEGylated substrates.

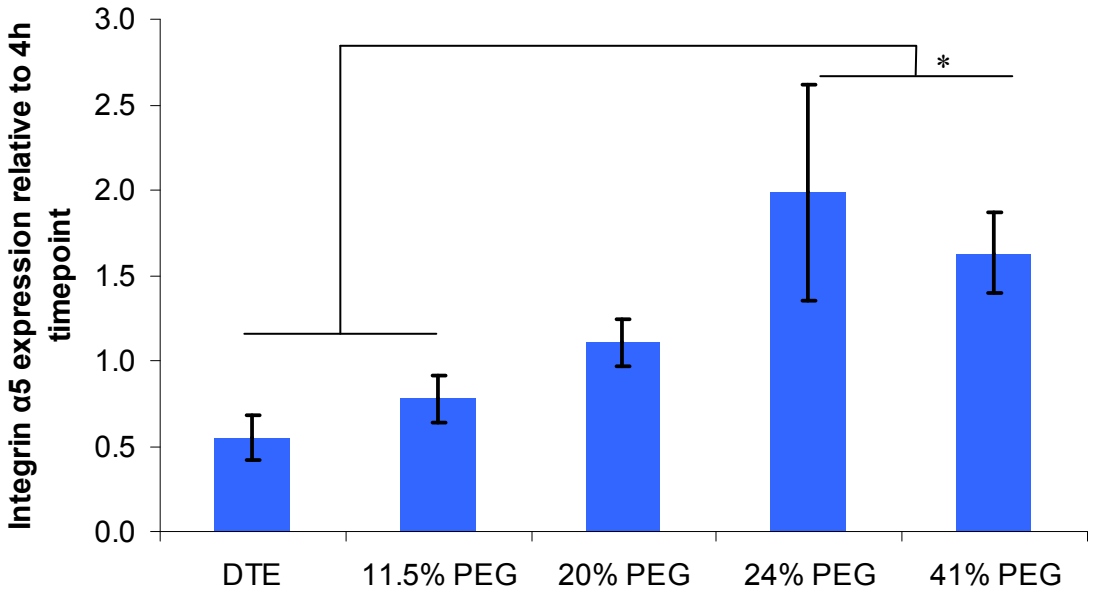

Figure 5.8 – QPCR of integrin α5 RNA at 24 hours relative to 4 hours. Error bars represent standard error. *: $p < 0.05$ for 24% PEG and 41% PEG vs. DTE and 11.5% PEG

5.3. Conclusions

Attachment of SaOS-2 cells to DTE-PEG polymers was investigated. Increasing amounts of PEG reduced protein adsorption and cell attachment, but interestingly, cell spreading increased on the highest concentration of PEG studied, 41%. This was contrary to the assumption that increases in phase-separated, PEG-rich domains would inhibit the ability of cells to spread. However, closer analysis of the phase separation dimensions measured by SANS indicate that increased spreading on 41% PEG may be driven by regularly spaced hydrophobic patches that are slightly larger in size than other polymers with less PEG, such as the 20% PEG substrate. Additionally, cells on the 41% PEG substrate compensated by dynamically upregulating the expression of integrin α5 to overcome the anti-adhesive surface and spread even more on highly PEGylated surfaces.

By contrast, intermediately PEGylated surfaces did not induce an increase in integrin α5 expression, and cells remained poorly spread. The results seem to suggest that the straightforward incorporation of large amounts of PEG may not be enough to develop anti-adhesive surfaces. Instead, an optimization process is needed to both prevent cells from attaching and to keep them from adjusting to the surface, which can be accomplished by using an intermediate amount of PEG.

6. Conclusions and Future Work

6.1. Thesis summary

A library of DTE-PEG random multiblock copolymers with PEG contents ranging from 20-40 wt% PEG and PEG molecular weights of 100 to 35000 were successfully synthesized using automated parallel synthesis. SANS was used to identify possible phase separation in amorphous DTE-PEG polymers as well as other amorphous polymers, such as PDLLA and PLGA, and semicrystalline polymers, such as PGA and PLA. DTE-PEG polymers were amorphous, yet showed different scattering properties compared to other amorphous polymers, such as PDLLA and PLGA, because of phase separation between DTE and PEG.

Scattering from DTE-PEG polymers was described as the formation of spherical, PEG-rich regions through the Z-P model. As PEG molecular weight was increased, domains became larger and farther apart. As the amount of PEG was increased, domains became smaller, closer together, and more numerous. In all instances, phase separation occurred on the 10-30 nm length scale, smaller than the 50-100 nm scale that is observed for block copolymers with fixed architectures (i.e. diblock, triblock, etc.).

Protein adsorption studies showed high protein adsorption for PEG_{100}-containing materials, low protein adsorption on intermediate PEG molecular weight polymers, and inconsistent protein adsorption for high PEG molecular weight polymers. Fractionation of high PEG molecular weight polymers yielded fractions that had large variation in the PEG content between fractions. Fractions of poly(DTE-*co*-11.5wt% PEG_{1k} carbonate)

showed no significant compositional variation between fractions due to the higher PEG:DTE molar. Nevertheless, these fractions showed large differences in protein adsorption. Contact angle hysteresis measurements confirmed that the surface properties of the polymer fractions were significantly more heterogeneous than the unfractionated polymer, suggesting that phase separation plays a role in protein adsorption behavior.

Studies with SaOS-2 osteosarcoma cells indicated that cell attachment decreased with increasing amounts of PEG, but surprisingly, cells spread significantly more on surfaces containing high amounts of PEG, compared to intermediate amounts of PEG. When related to phase separation experiments, adhesive ligands could be slightly closer and more evenly spaced on high PEG-containing materials compared to intermediate PEG-containing materials, perhaps facilitating the increased spreading of the cells. Studies on the expression of the integrin α5 cell surface adhesive protein showed that integrin α5 was upregulated both intracellularly and extracellularly. Intracellular upregulation was found to occur dynamically over time with adhered cells, showing that cells reacted to the hostile surface as opposed to the surface selecting for potentially mutated cells.

6.2. Novelty and significance

The SANS work performed in this thesis represents some of the first experimental quantitative data reported in the literature about the dimensions of phase-separated domains in random multiblock copolymers. The data may also have important ramifications with regards to how erosion progresses over time in PEG-containing

polymers as described in Section 3.3. The study by Sousa et al. serves as the end-point of polymer erosion in DTE-PEG polymers [146], while the work described here serves as the initial description point of how PEG-rich domains form.

While spatial feature variations produced by increases in PEG molecular weight and PEG content do not conclusively show protein adsorption modulation, fractionation of certain DTE-PEG compositions shows differences in protein adsorption even for materials with the same composition. Several studies have shown that molecular weight and polydispersity affect polymer morphology [93, 188-189]. However, the direct relationship between molecular weight, polydispersity, polymer morphology, and protein adsorption, has not yet been clearly demonstrated. Contact angle hysteresis measurements performed in this thesis show that fractionated polymers are more heterogeneous than their unfractionated counterparts. This heterogeneity appears to confer the fractionated polymers with adsorptive capabilities, even with materials that have identical compositions. Few studies have shown that polymer fractionation can be used as a processing method to provide materials with different protein adsorption capabilities. The potential correlation between polymer molecular weight, chain uniformity, and biological properties implies that quality control during synthesis and fabrication for biomedical polymers must be extremely well-controlled to avoid unwanted complications. Conversely, the potential to modulate biological properties, while keeping composition other polymer properties constant can be a very powerful tool for developing biomaterials for different applications without requiring specialized fabrication techniques.

The discovery that SaOS-2 cells are able to adjust to highly PEGylated surfaces by increasing spreading has not been shown previously. In fact, using a rat fibroblast cell

line, the exact opposite was previously observed by Ryan et al. with the same polymer system [190]. However, their substrates were only examined up to poly(DTE-*co*-11.5 wt% PEG_{1k} carbonate), suggesting that extreme amounts of PEG cause cells to react dynamically. Other relevant reasons for this increased spreading, such as the effect of exogenous reactive oxygen species formed from PEG auto-oxidation, is addressed in the manuscript that was submitted to Soft Matter, but discussion of this topic is outside of the scope of this thesis. The results by both Ryan et al. and the work presented in Chapter 5 suggest that polymers with intermediate amounts of PEG may be better suited for producing non-adhesive, non-fouling surfaces, instead of very highly PEGylated materials.

6.3. Future work

To clearly understand the ramifications of PEG and phase separation on erosion, a library of polymers could be studied over a longer period of time to determine how hydrated domains evolve. Sousa et al. report that erosion channels form after one year in PBS [146]. By incubating a collection of films at two-week intervals, SANS could be used to provide a continuous snapshot of how PEG-rich domains form over time, as well as how the erosion mechanism occurs. Such a study would provide significant insight into the use of erodible biomedical polymers for drug delivery and tissue regeneration purposes.

Two main drawbacks in the fractionation studies were that material was limited and that the fractionation was done in a simplistic fashion. It would be interesting to

know whether how the mechanical properties of the fractionated polymers compared to the as-is polymer, but the amount of polymer yielded per fraction was not enough to study this. Furthermore, simply using a larger amount of polymer to start would probably reduce the distinctiveness between fractions, as larger amounts of low molecular weight polymer would be precipitated during each fractionation step. A size exclusion column would be ideal for separating polymer chains based on weight. Large amounts of polymer could then be extracted and tested to determine whether other properties, such as mechanical strength and ease of fabrication, are affected by fractionation.

Extension of the cell work to examine how other cell types behave may also be desirable. While SaOS-2 cells showed novel behavior on the tested substrates, other cell types could also be examined that have relevance to cardiovascular, nervous, or respiratory systems, for example. It could then be determined whether the cellular compensation mechanisms observed with the SaOS-2 cells are conserved between cell types or exclusive to bone or load-bearing cells.

7. Appendix

7.1. Spin-coating optimization for QCM-D studies

Spin-coated substrates were used for protein adsorption and cell studies. To ensure that surface roughness would not be a factor in these measurements, validation studies were performed to examine the effectiveness of the spin-coating procedure in developing thin, fault-free films. Polymer solutions were dissolved in a volatile solvent, such as methylene chloride or tetrahydrofuran (THF). Initial spin-coating experiments were performed using THF as-received from suppliers, with spin-coating parameters as described in Section 2.4.2. Poly(DTE carbonate) was used as a test polymer. Coating quality was measured by AFM to determine the presence of surface defects. A schematic of the physical events that occur during spin-coating are shown in Figure 7.1.

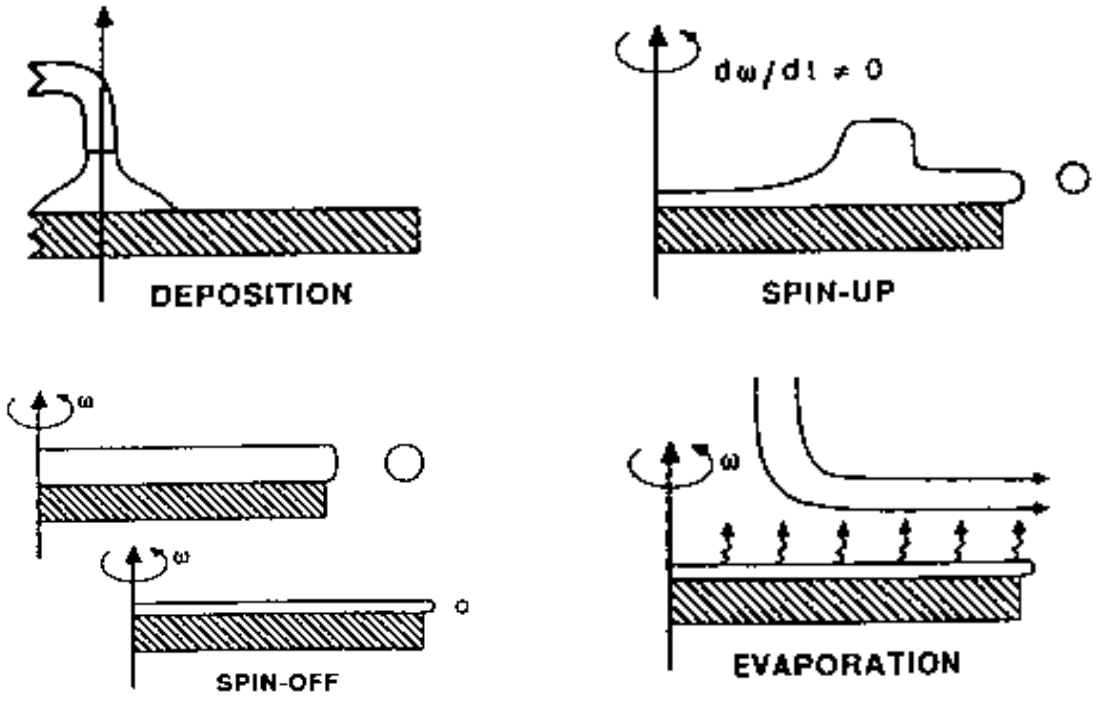

Figure 7.1 – General spin-coating procedure [191]. Image reproduced with permission from copyright owners, The Society for Imaging Science and Technology.

The large number of surface defects present in Figure 7.2 indicates that one of the events during the spin coating process is causing either uneven evaporation of the solvent or another liquid is present that evaporates at a different rate. Because the relative humidity of the system was at an acceptably low level, it was assumed that water may be present in the THF. To remediate this issue, molecular sieves were added to the solvent to aid in the removal of water. After sieving the solvent, polymers were again dissolved and spin-coated using standard parameters.

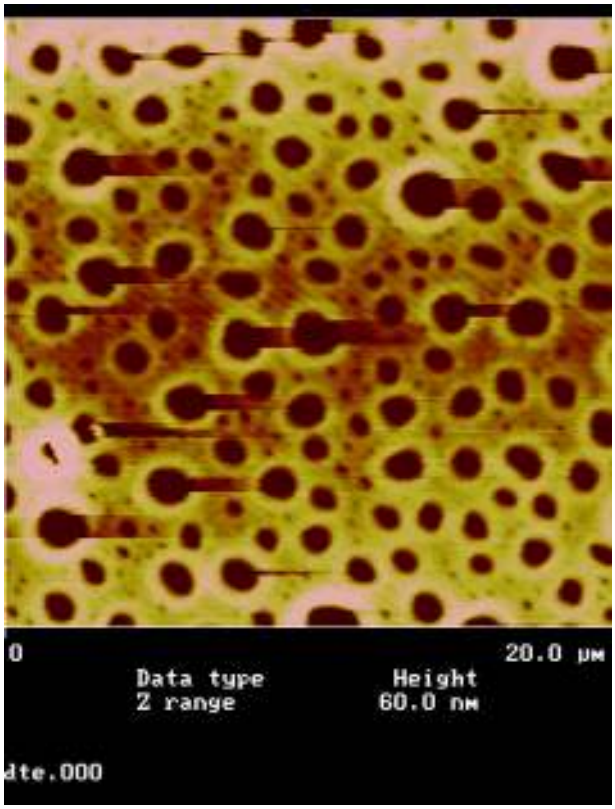

Figure 7.2 – AFM image from poly(DTE carbonate) spin-coated from a 1% w/v solution in THF. Large holes are present on the surface.

The large reduction in pinholes shows that solvent "dryness" can play a large role in spin-coated film quality, as seen in Figure 7.3. However, small "nanoholes" are still visible, despite the marked improvement in surface quality. To further improve coating quality, a less volatile, more viscous solvent was used, 1, 4-dioxane (referred to as dioxane for the remainder of the text).

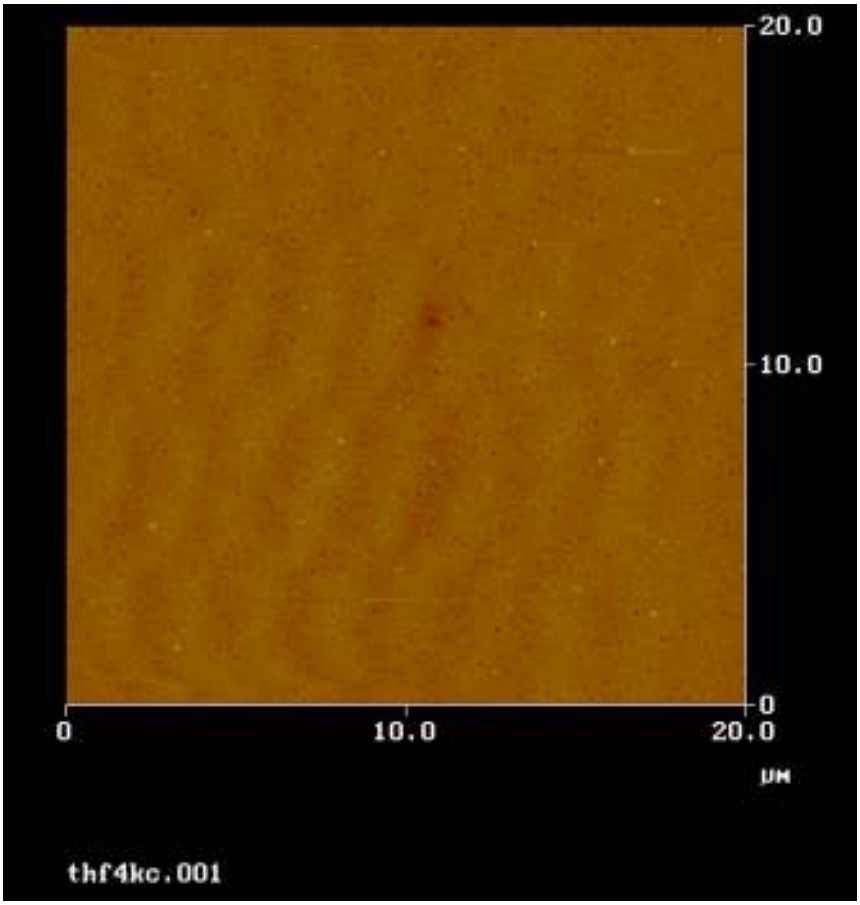

Figure 7.3 - AFM image for poly(DTE carbonate) spin-coated from a 1% w/v solution in sieved THF. Small holes are still present, even after using molecular sieves.

The dioxane-coated polymer further improves the surface quality by eliminating the appearance of the "nanoholes." Therefore, dioxane was used as a spin-coating solvent for the remaining protein adsorption studies. While some concern that residual dioxane may affect studies due to its relatively high boiling point (101 °C vs. 66 °C for THF), the solvent is still quite volatile and can readily evaporate both in a standard laboratory fume hood and under ambient conditions. Additionally, equilibration steps during QCM-D measurements involve placing the crystal under flow with copious amounts of PBS, thereby heavily diluting the solvent and minimizing its impact on proteins during QCM-

D studies. Other internal studies have shown that SaOS-2 cells grown on polymers spin-coated with dioxane and THF perform comparably (data not shown).

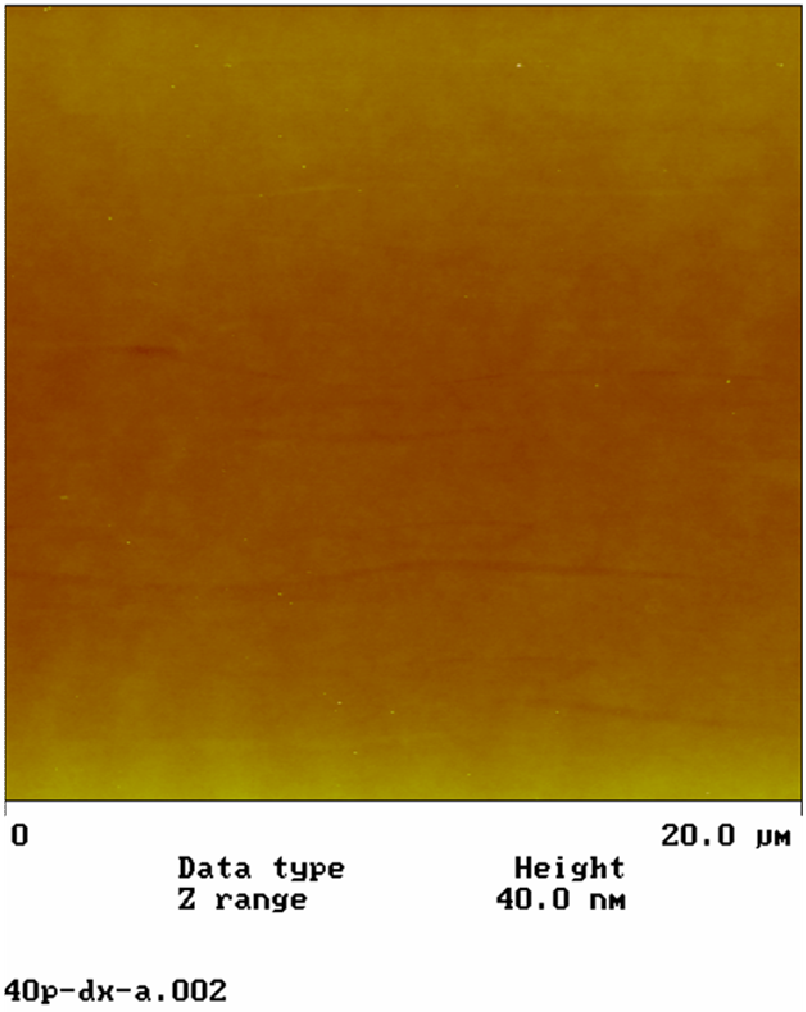

Figure 7.4 – AFM image from poly(DTE carbonate) spin-coated from a 1% w/v solution in sieved dioxane. Surfaces appear to be smooth and pinhole-free.

7.2. Sample NMRs for polymers with varying PEG molecular weights

Peak assignments for DTE-PEG polymers, previously discussed by Yu et al., are described in Figure 2.1. Calculations for the PEG wt% were previously described in Section 2.3.2. For all DTE-PEG polymers, NMR spectra were normalized about the peak

at 4.8 ppm, corresponding to the single CH group in the DTE molecule. For polymers containing similar weight percentages of PEG and different PEG molecular weights, NMR spectra contained some notable differences. An NMR with poly(DTE-*co*-41wt% PEG_{100} carbonate), poly(DTE-*co*-41wt% PEG_{1k} carbonate), and poly(DTE-*co*-41wt% PEG_{35k} carbonate) is shown in Figure 7.5. The main differences seen between the polymers can be observed from the 3.3-4.6 ppm region, which are magnified in Figure 7.6. The peaks seen for poly(DTE-*co*-41wt% PEG_{100} carbonate) (red) are much larger between 4.2-4.5 ppm, while these peaks are much smaller for poly(DTE-*co*-41wt% PEG_{1k} carbonate) (green), and nonexistent for poly(DTE-*co*-41wt% PEG_{35k} carbonate) (black). This suggests that the peaks are the product of PEG-CH2-carbonate groups, which would be in very high concentration for the PEG_{100} material. Conversely, the peak at 3.65 ppm is very large for the PEG35k-containing polymer, medium for the PEG1k-containing polymer, and nonexistent for the PEG100 polymer. In this case, this peak refers to the $(CH_2\text{-}CH_2\text{-}O\text{-})_n$ PEG structure, which is incomplete for PEG100, which contains only a $CH_2\text{-}CH_2\text{-}O\text{-}CH_2\text{-}CH_2$-carbonate linkage for every PEG repeat unit. An additional point of emphasis is that the PEG_{100} polymers have a larger peak at around 7.1 ppm. This peak corresponds to the hydrogens in the tyrosine ring structure seen in Figure 2.1. The presence of this peak indicates that the chain structures are indeed random, because it would not exist if the PEG molecules formed long chains of PEG carbonate.

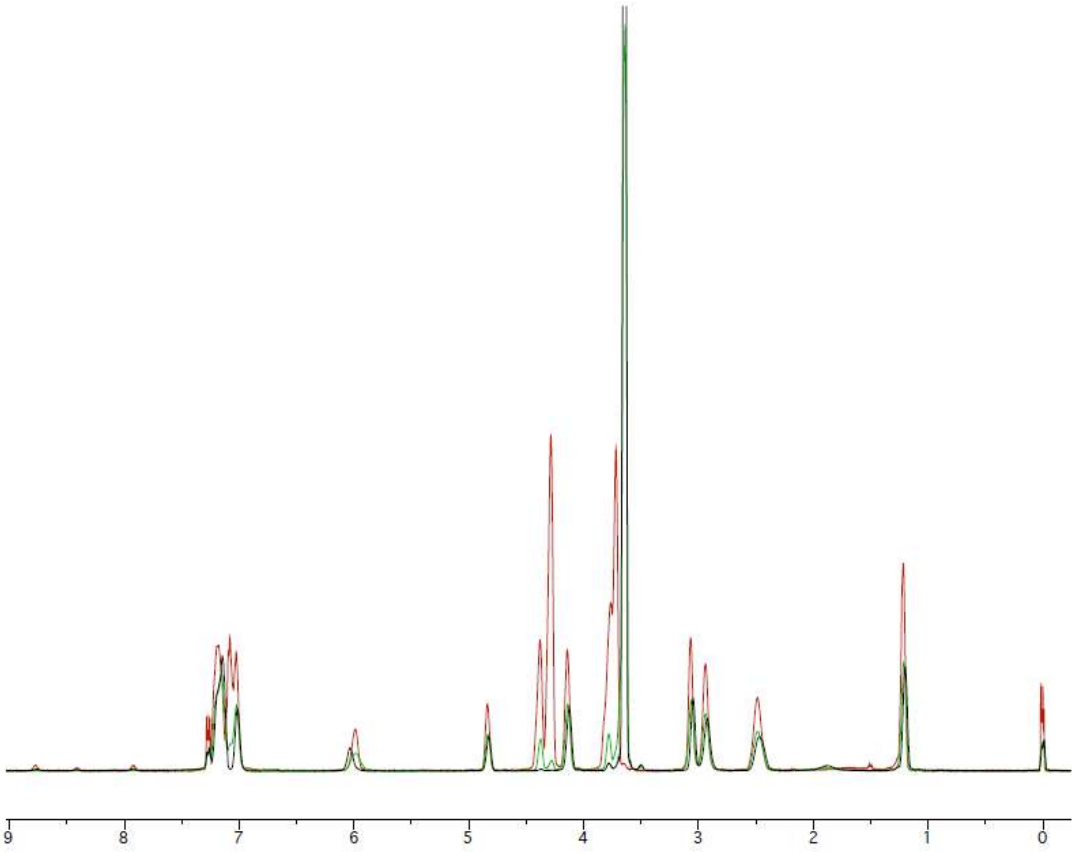

Figure 7.5 – NMR overlay of poly(DTE-co-41wt% PEG_{100} carbonate) (red), poly(DTE-co-41wt% PEG_{1k} carbonate) (green), and poly(DTE-co-41wt% PEG_{35k} carbonate) (black).

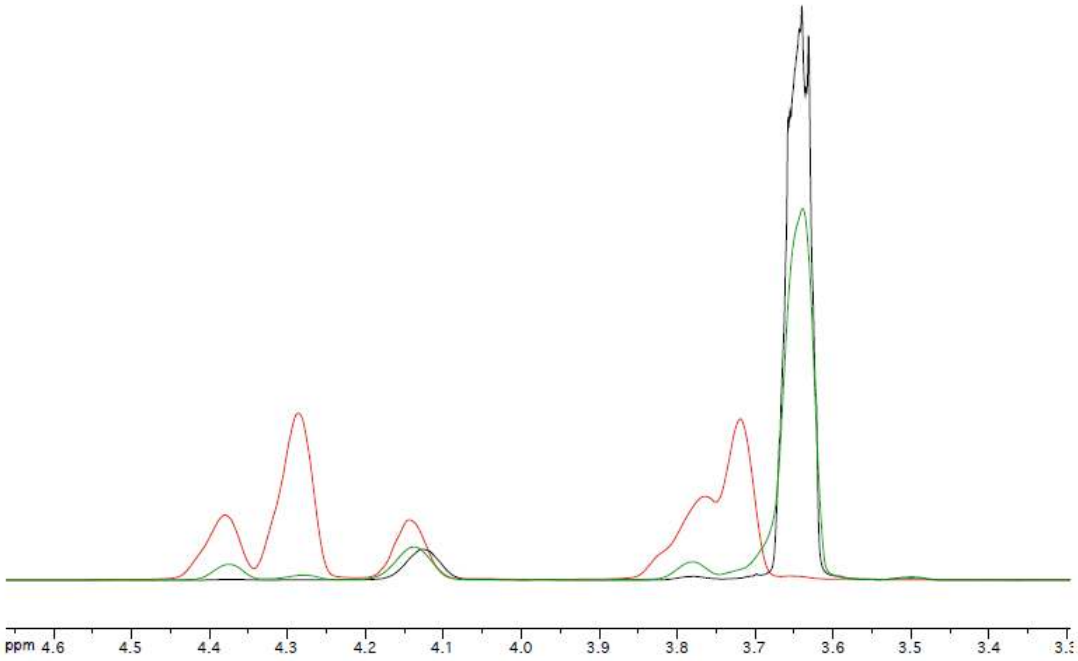

Figure 7.6 – NMR overlay of poly(DTE-co-41wt% PEG_{100} carbonate) (red), poly(DTE-co-41wt% PEG_{1k} carbonate) (green), and poly(DTE-co-41wt% PEG_{35k} carbonate) (black) between 3.3 and 4.6 ppm.

7.3. NMR sample calculations

A sample figure of 20-1k is provided in Figure 7.7. While there are several peaks that can be chosen to represent the DTE segment, two peaks are of interest: the CH peak (letter m in Figure 2.1), which is normalized to 1 hydrogen, and the CH_2 peak (letter b in Figure 2.1) in the ethyl ester. The main peak of interest for PEG is large peak at 3.64 ppm. As seen in Figure 7.7, several sources of error can be present in the integration of this peak, such as spinning side bands and other noise. In the example in Figure 7.7, the

values for the CH2 peak and the PEG peak are 1.98 and 8.52, respectively. Using the calculations described in Section 2.3.2, the PEG composition can be calculated.

In this case, DTE_{norm} = 1.98/2, or 0.99, where 2 is the two hydrogens in the CH_2 group. PEG_{norm} = 8.52/(1000*4/44) = 0.094, where 1000 is the molecular weight of PEG used, 4 is the number of hydrogens in a single repeat unit of PEG (4 hydrogens in CH_2CH_2O), and 44 is the total molecular weight of the PEG repeat unit. These two values represent the number of hydrogen atoms normalized per representative peak for each group in the polymer. From these two values, the PEG wt% can be calculated as a weighted fraction of the total weight for each molecule. In this case: PEGwt% = (0.094*1000)/((0.094*1000)+(0.99+357)) = 0.21, i.e. 21 wt% of the polymer is represented by PEG, which is close to the expected value.

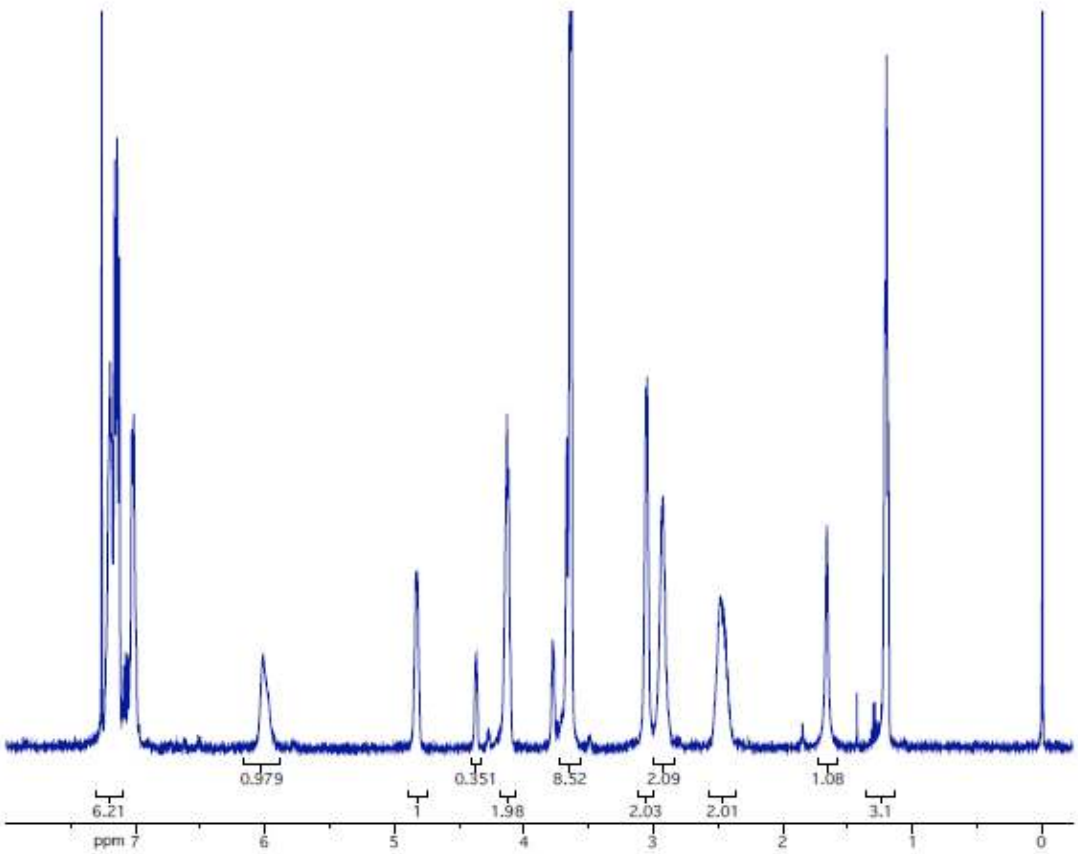

Figure 7.7 – Sample NMR of 20-1k.

7.4. NMR calculation tables

Table 7.1 – NMR calculations of manually synthesized (I_2)DTE-PEG polymers

Sample	4.1 ppm	3.6 ppm	ratio 4.1/3.6	PEG MW	PEG mol%	PEG wt%
DTE-24% PEG_{1k}	2.21	9.93	4.49	1000	9.00%	21.7%
DTE-50% PEG_{2k}	1.64	22.6	13.8	2000	13.2%	45.9%
DTE-41% PEG_{1k}	1.93	17.8	9.22	1000	16.9%	36.2%
DTE-71% PEG_{2k}	1.89	64.9	34.3	2000	27.4%	67.9%
DTE-41% PEG_{35k}	1.99	25.5	12.8	35000	0.799%	44.1%
DTE-41% PEG_{100}	2.09	75.1	35.9	100	88.2%	68.9%
I_2DTE-7.9% PEG_{1k}	1.59	5.60	3.52	1000	7.19%	17.8%
I_2DTE-29% PEG_{1k}	0.837	50.5	60.3	1000	57.0%	78.8%

Most manually synthesized polymers were reasonably close to their expected value. Inaccuracies with the PEG_{100}-containing polymers stemmed from issues seen in Figure 7.6, where the PEG peak may not be as well-defined as in higher molecular weight PEG-containing polymers. I_2DTE-PEG materials were difficult to monitor as well, though T_g values in Table 3.1 suggests that the PEG contents are correct, i.e., T_g decreases as more PEG is incorporated.

Table 7.2 – NMR calculations for DTE-PEG polymers prepared by automated parallel synthesis

composition	4.1 ppm	3.6 ppm	ratio 4.1/3.6	PEG MW	PEG wt%
20% 100	1.96	3.41	1.74	100	9.68%
30% 100	2.02	5.25	2.60	100	13.8%
40% 100	1.9	7.7	4.05	100	20.0%
20% 1k	1.98	8.52	4.30	1000	21.0%
30% 1k	2.05	14.5	7.07	1000	30.4%
40% 1k	1.98	19	9.60	1000	37.2%
20% 2k	1.99	8.92	4.48	2000	21.6%
30% 2k	2.05	24.7	12.05	2000	42.6%
40% 2k	1.98	21	10.61	2000	39.5%
20% 8k	1.83	9.27	5.07	8000	23.8%
30% 8k	2.02	14.6	7.23	8000	30.8%
40% 8k	2.04	20.2	9.90	8000	37.9%
20% 20k	2.04	11.3	5.54	20000	25.4%
30% 20k	2.15	14.2	6.60	20000	28.9%
40% 20k	2.01	5.14	2.56	20000	13.6%
20% 35k	1.97	15	7.61	35000	31.9%
30% 35k	2.03	19.3	9.51	35000	36.9%
40% 35k	2.04	19	9.31	35000	36.5%

The PEG_{1k}, PEG_{2k}, and PEG_{8k} polymers all appeared to have accurate compositions based on NMR. However, the PEG_{100}, PEG_{20k}, and PEG_{35k} polymers did not appear as accurate. Issues with PEG_{100} polymers were described previously. No clear issues were seen with the DTE-PEG_{20k} and DTE-PEG_{35k} NMRs, except for 40-20k,

which may have been too dilute in DMSO to give a proper signal. Again, any potential doubts about compositions being inaccurate can be alleviated by comparing the PEG content with the T_g from Table 4.1 and Table 4.2, where T_g mainly decreases as PEG content increases. The only polymer where this trend did not hold was with 30-2k, where PEG content was higher than expected, and the T_g was lower than expected. SANS results on this polymer also did not follow the expected trend, suggesting that the composition for this polymer did in fact deviate from expected values.

Table 7.3 – NMR calculations for fractionated 20-20k polymers

Sample	4.1 ppm	3.6 ppm	ratio 4.1/3.6	PEG MW	PEG mol%	PEG wt%
20% 20k F1-1	2.03	2.97	1.46	20000	0.16%	8.27%
20% 20k F1-2	1.98	3.81	1.92	20000	0.21%	10.6%
20% 20k F1-3	2.00	6.33	3.17	20000	0.35%	16.3%
20% 20k F1-4	1.96	12.90	6.58	20000	0.72%	28.9%
20% 20k F1	1.97	3.93	1.99	20000	0.22%	10.9%
20% 20k F2	1.76	15.50	8.81	20000	0.96%	35.2%
20% 20k F3	1.96	18.70	9.54	20000	1.04%	37.0%
20% 20k F4	1.67	5.27	3.16	20000	0.35%	16.3%

Table 7.4 – NMR calculations for fractionated 11.5-1k polymers

Sample	4.1 ppm	3.6 ppm	ratio 4.1/3.6	PEG MW	PEG mol%	PEG wt%
11.5% PEG1k F1	1.99	4.07	0.489	1000	4.31%	11.2%
11.5% PEG1k F2	1.60	3.32	0.482	1000	4.37%	11.3%
11.5% PEG1k F3	1.98	4.21	0.470	1000	4.47%	11.6%
11.5% PEG1k F4	1.97	4.29	0.459	1000	4.57%	11.8%
11.5% PEG1k F1-1	2.00	4.05	0.494	1000	4.26%	11.1%
11.5% PEG1k F1-2	1.96	4.07	0.482	1000	4.37%	11.3%
11.5% PEG1k F1-3	1.99	4.08	0.488	1000	4.32%	11.2%
11.5% PEG1k F1-4	2.00	4.20	0.476	1000	4.42%	11.5%

References

1. Andrade, J.D. and V. Hlady, *Protein Adsorption and Materials Biocompatibility - a Tutorial Review and Suggested Hypotheses.* Advances in Polymer Science, 1986. **79**: p. 1-63.
2. Fant, C., H. Elwing, and F. Hook, *The influence of cross-linking on protein-protein interactions in a marine adhesive: the case of two byssus plaque proteins from the blue mussel.* Biomacromolecules, 2002. **3**(4): p. 732-41.
3. Schultz, M.P., *Frictional resistance of antifouling coating systems.* Journal of Fluids Engineering-Transactions of the Asme, 2004. **126**(6): p. 1039-1047.
4. Fukuzaki, S., H. Urano, and K. Nagata, *Adsorption of bovine serum albumin onto metal oxide surfaces.* Journal of Fermentation and Bioengineering, 1996. **81**(2): p. 163-167.
5. Grainger, D.W., et al., *Invitro and Exvivo Platelet Interactions with Hydrophilic Hydrophobic Poly(Ethylene Oxide)-Polystyrene Multiblock Copolymers.* Journal of Biomedical Materials Research, 1989. **23**(9): p. 979-1005.
6. Anderson, J.M., T.L. Bonfield, and N.P. Ziats, *Protein Adsorption and Cellular Adhesion and Activation on Biomedical Polymers.* International Journal of Artificial Organs, 1990. **13**(6): p. 375-382.
7. Armstrong, J., et al., *Interfacial adsorption of fibrinogen and its inhibition by RGD peptide: a combined physical study.* Journal of Physics-Condensed Matter, 2004. **16**(26): p. S2483-S2491.
8. Kilpadi, K.L., P.L. Chang, and S.L. Bellis, *Hydroxylapatite binds more serum proteins, purified integrins, and osteoblast precursor cells than titanium or steel.* Journal of Biomedical Materials Research, 2001. **57**(2): p. 258-267.
9. Ratner, B.D. and S.J. Bryant, *Biomaterials: Where we have been and where we are going.* Annual Review of Biomedical Engineering, 2004. **6**: p. 41-75.
10. Horbett, T.A. and J.L. Brash, *Proteins at Interfaces II: Fundamentals and Applications*, ed. T.A. Horbett and J.L. Brash. 1995, Washington, DC: American Chemical Society. 561.
11. Bohnert, J.L. and T.A. Horbett, *Changes in Adsorbed Fibrinogen and Albumin Interactions with Polymers Indicated by Decreases in Detergent Elutability.* Journal of Colloid and Interface Science, 1986. **111**(2): p. 363-378.
12. Kim, J. and G.A. Somorjai, *Molecular packing of lysozyme, fibrinogen, and bovine serum albumin on hydrophilic and hydrophobic surfaces studied by infrared-visible sum frequency generation and fluorescence microscopy.* Journal of the American Chemical Society, 2003. **125**(10): p. 3150-3158.
13. Kondo, A., S. Oku, and K. Higashitani, *Structural-Changes in Protein Molecules Adsorbed on Ultrafine Silica Particles.* Journal of Colloid and Interface Science, 1991. **143**(1): p. 214-221.
14. Andrade, J.D., *Principles of Protein Adsorption*, in *Surface and Interfacial Aspects of Biomedical Polymers, Volume 2: Protein Adsorption*, J.D. Andrade, Editor. 1985, Plenum Press: New York. p. 63-66.
15. Horbett, T.A., *Protein Adsorption on Biomaterials*, in *Biomaterials: Interfacial Phenomena and Applications*, S.L. Cooper, et al., Editors. 1982, American Chemical Society: Washington, D.C. p. 233-244.

16. Slack, S.M. and T.A. Horbett, *Changes in the Strength of Fibrinogen Attachment to Solid-Surfaces - an Explanation of the Influence of Surface-Chemistry on the Vroman Effect.* Journal of Colloid and Interface Science, 1989. **133**(1): p. 148-165.
17. Balasubramanian, V., et al., *Residence-time dependent changes in fibrinogen adsorbed to polymeric biomaterials.* J Biomed Mater Res, 1999. **44**(3): p. 253-60.
18. Horbett, T.A., et al., *Rapid postadsorptive changes in fibrinogen adsorbed from plasma to segmented polyurethanes.* J Biomater Sci Polym Ed, 1998. **9**(10): p. 1071-87.
19. Goda, T., et al., *Protein Adsorption Resistance and Oxygen Permeability of Chemically Crosslinked Phospholipid Polymer Hydrogel for Ophthalmologic Biomaterials.* Journal of Biomedical Materials Research Part B-Applied Biomaterials, 2009. **89B**(1): p. 184-190.
20. Gorbet, M.B. and M.V. Sefton, *Biomaterial-associated thrombosis: roles of coagulation factors, complement, platelets and leukocytes.* Biomaterials, 2004. **25**(26): p. 5681-5703.
21. Fattori, R. and T. Piva, *Drug-eluting stents in vascular intervention.* The Lancet, 2003. **361**(9353): p. 247-249.
22. Woo, K.M., V.J. Chen, and P.X. Ma, *Nano-fibrous scaffolding architecture selectively enhances protein adsorption contributing to cell attachment.* Journal of Biomedical Materials Research Part A, 2003. **67A**(2): p. 531-537.
23. Anderson, J.M., *BIOLOGICAL RESPONSES TO MATERIALS.* Annual Review of Materials Research, 2001. **31**(1): p. 81-110.
24. Ohyama, T., et al., *ProNectin F-grafted-ethylene vinyl alcohol copolymer (EVAL) as a liquid type material for treating cerebral aneurysm--an in vivo and in vitro study.* Biomaterials, 2004. **25**(17): p. 3845-52.
25. Fuss, C., J.C. Palmaz, and E.A. Sprague, *Fibrinogen: Structure, function, and surface interactions.* Journal of Vascular and Interventional Radiology, 2001. **12**(6): p. 677-682.
26. Toscano, A. and M.M. Santore, *Fibrinogen adsorption on three silica-based surfaces: conformation and kinetics.* Langmuir, 2006. **22**(6): p. 2588-97.
27. Farrell, D.H., et al., *Role of fibrinogen alpha and gamma chain sites in platelet aggregation.* Proc Natl Acad Sci U S A, 1992. **89**(22): p. 10729-32.
28. Kam, P.C. and M.K. Egan, *Platelet glycoprotein IIb/IIIa antagonists: pharmacology and clinical developments.* Anesthesiology, 2002. **96**(5): p. 1237-49.
29. Tang, L.P. and J.W. Eaton, *Fibrin(Ogen) Mediates Acute Inflammatory Responses to Biomaterials.* Journal of Experimental Medicine, 1993. **178**(6): p. 2147-2156.
30. Tsai, W.B., J.M. Grunkemeier, and T.A. Horbett, *Human plasma fibrinogen adsorption and platelet adhesion to polystyrene.* J Biomed Mater Res, 1999. **44**(2): p. 130-9.
31. Kragh-Hansen, U., *Molecular aspects of ligand binding to serum albumin.* Pharmacol Rev, 1981. **33**(1): p. 17-53.
32. Squire, P.G., P. Moser, and C.T. O'Konski, *Hydrodynamic properties of bovine serum albumin monomer and dimer.* Biochemistry, 1968. **7**(12): p. 4261-4272.

33. Michel, R., et al., *Influence of PEG architecture on protein adsorption and conformation.* Langmuir, 2005. **21**(26): p. 12327-12332.
34. Kubota, Y. and H. Ueki, *Determination of the isoelectric point of bovine plasma albumin by cellulose acetate paper electrophoresis.* J Biochem, 1968. **64**(3): p. 405-6.
35. Triantaphyllopoulos, E. and D.C. Triantaphyllopoulos, *Amino acid composition of human fibrinogen and anticoagulant derivatives.* Biochem J, 1967. **105**(1): p. 393-400.
36. Rodrigues, S.N., et al., *Fibrinogen adsorption, platelet adhesion and activation on mixed hydroxyl-/methyl-terminated self-assembled monolayers.* Biomaterials, 2006. **27**(31): p. 5357-5367.
37. Kottke-Marchant, K., et al., *Effect of albumin coating on the in vitro blood compatibility of Dacron arterial prostheses.* Biomaterials, 1989. **10**(3): p. 147-55.
38. Ostuni, E., et al., *A survey of structure-property relationships of surfaces that resist the adsorption of protein.* Langmuir, 2001. **17**(18): p. 5605-5620.
39. Ostuni, E., L. Yan, and G.M. Whitesides, *The interaction of proteins and cells with self-assembled monolayers of alkanethiolates on gold and silver.* Colloids and Surfaces B-Biointerfaces, 1999. **15**(1): p. 3-30.
40. Okano, T., et al., *Effect of hydrophilic and hydrophobic microdomains on mode of interaction between block polymer and blood platelets.* J Biomed Mater Res, 1981. **15**(3): p. 393-402.
41. Childs, M.A., et al., *Surface morphology of poly(caprolactone)-b-poly(dimethylsiloxane)-b-poly(caprolactone) copolymers: Effects on protein adsorption.* Biomacromolecules, 2001. **2**(2): p. 526-537.
42. Kumar, N. and J.I. Hahm, *Nanoscale protein patterning using self-assembled diblock copolymers.* Langmuir, 2005. **21**(15): p. 6652-6655.
43. Baszkin, A. and D.J. Lyman, *The interaction of plasma proteins with polymers. I. Relationship between polymer surface energy and protein adsorption/desorption.* Journal of Biomedical Materials Research, 1980. **14**(4): p. 393-403.
44. Rechendorff, K., et al., *Enhancement of Protein Adsorption Induced by Surface Roughness.* Langmuir, 2006. **22**(26): p. 10885-10888.
45. Ge, S.R., et al., *Bovine serum albumin adsorption onto immobilized organotrichlorosilane surface: Influence of the phase separation on protein adsorption patterns.* Journal of Biomaterials Science-Polymer Edition, 1998. **9**(2): p. 131-150.
46. Kim, D.K. and S.B. Lee, *Comparison of surface properties of random, block, and graft copolymers having perfluoroalkyl and silicone-containing side chains.* Journal of Colloid and Interface Science, 2002. **247**(2): p. 490-493.
47. Satulovsky, J., M.A. Carignano, and I. Szleifer, *Kinetic and thermodynamic control of protein adsorption.* Proceedings of the National Academy of Sciences of the United States of America, 2000. **97**(16): p. 9037-9041.
48. Khor, H.L., et al., *Response of cells on surface-induced nanopatterns: fibroblasts and mesenchymal progenitor cells.* Biomacromolecules, 2007. **8**(5): p. 1530-40.
49. Seo, J.H., et al., *Cell adhesion on phase-separated surface of block copolymer composed of poly(2-methacryloyloxyethyl phosphorylcholine) and poly(dimethylsiloxane).* Biomaterials, 2009. **30**(29): p. 5330-40.

50. Sousa, A., et al., *Selective protein adsorption on a phase-separated solvent-cast polymer blend.* Langmuir, 2006. **22**(14): p. 6286-6292.
51. Okano, T., et al., *Interaction between Plasma Protein and Microphase Separated Structure of Copolymers.* Polymer, 1978. **10**(2): p. 223-228.
52. Abuchowski, A., et al., *Alteration of immunological properties of bovine serum albumin by covalent attachment of polyethylene glycol.* J Biol Chem, 1977. **252**(11): p. 3578-81.
53. Mori, Y., et al., *A new antithrombogenic material with long polyethyleneoxide chains.* Trans Am Soc Artif Intern Organs, 1982. **28**: p. 459-63.
54. Israelachvili, J., *The different faces of poly(ethylene glycol).* Proceedings of the National Academy of Sciences of the United States of America, 1997. **94**(16): p. 8378-8379.
55. Liu, K.-J. and J.L. Parsons, *Solvent Effects on the Preferred Conformation of Poly(ethylene glycols).* Macromolecules, 1969. **2**(5): p. 529-533.
56. Latour, R.A., *Thermodynamic perspectives on the molecular mechanisms providing protein adsorption resistance that include protein-surface interactions.* Journal of Biomedical Materials Research Part A, 2006. **78A**(4): p. 843-854.
57. Bergstrom, K., et al., *Reduction of fibrinogen adsorption on PEG-coated polystyrene surfaces.* J Biomed Mater Res, 1992. **26**(6): p. 779-90.
58. Sharma, S., R.W. Johnson, and T.A. Desai, *XPS and AFM analysis of antifouling PEG interfaces for microfabricated silicon biosensors.* Biosensors & Bioelectronics, 2004. **20**(2): p. 227-239.
59. Leckband, D., S. Sheth, and A. Halperin, *Grafted poly(ethylene oxide) brushes as nonfouling surface coatings.* J Biomater Sci Polym Ed, 1999. **10**(10): p. 1125-47.
60. D'Sa, R.A. and B.J. Meenan, *Chemical Grafting of Poly(ethylene glycol) Methyl Ether Methacrylate onto Polymer Surfaces by Atmospheric Pressure Plasma Processing.* Langmuir, 2009. **26**(3): p. 1894-1903.
61. Park, K., et al., *In vitro and in vivo studies of PEO-grafted blood-contacting cardiovascular prostheses.* J Biomater Sci Polym Ed, 2000. **11**(11): p. 1121-34.
62. Stadler, V., et al., *PEGMA/MMA copolymer graftings: generation, protein resistance, and a hydrophobic domain.* Langmuir, 2008. **24**(15): p. 8151-7.
63. Wagner, V.E., J.T. Koberstein, and J.D. Bryers, *Protein and bacterial fouling characteristics of peptide and antibody decorated surfaces of PEG-poly(acrylic acid) co-polymers.* Biomaterials, 2004. **25**(12): p. 2247-63.
64. Cerruti, M., et al., *Poly(ethylene glycol) monolayer formation and stability on gold and silicon nitride substrates.* Langmuir, 2008. **24**(19): p. 10646-53.
65. Herrwerth, S., et al., *Factors that determine the protein resistance of oligoether self-assembled monolayers --internal hydrophilicity, terminal hydrophilicity, and lateral packing density.* J Am Chem Soc, 2003. **125**(31): p. 9359-66.
66. Kanari, Y., et al., *Protein Adsorption on Self-Assembled Monolayers Induced by Surface Water Molecule.* Japanese Journal of Applied Physics, 2007. **46**(9B): p. 6303-6308.
67. Li, L., S. Chen, and S. Jiang, *Protein interactions with oligo(ethylene glycol) (OEG) self-assembled monolayers: OEG stability, surface packing density and protein adsorption.* J Biomater Sci Polym Ed, 2007. **18**(11): p. 1415-27.

68. Li, L., et al., *Protein adsorption on oligo(ethylene glycol)-terminated alkanethiolate self-assembled monolayers: The molecular basis for nonfouling behavior.* J Phys Chem B, 2005. **109**(7): p. 2934-41.
69. PY, J.Y., et al., *Self-assembled monothiol-terminated hyperbranched polyglycerols on a gold surface: a comparative study on the structure, morphology, and protein adsorption characteristics with linear poly(ethylene glycol)s.* Langmuir, 2008. **24**(9): p. 4907-16.
70. Vanderah, D.J., et al., *Control of protein adsorption: Molecular level structural and spatial variables.* Journal of the American Chemical Society, 2004. **126**(42): p. 13639-13641.
71. George, P.A., B.C. Donose, and J.J. Cooper-White, *Self-assembling polystyrene-block-poly(ethylene oxide) copolymer surface coatings: Resistance to protein and cell adhesion.* Biomaterials, 2009. **30**(13): p. 2449-2456.
72. Lee, J.H., J. Kopecek, and J.D. Andrade, *Protein-resistant surfaces prepared by PEO-containing block copolymer surfactants.* J Biomed Mater Res, 1989. **23**(3): p. 351-68.
73. Malmsten, M. and D. Muller, *Interfacial behaviour of 'new' poly(ethylene oxide)-containing copolymers.* J Biomater Sci Polym Ed, 1999. **10**(10): p. 1075-87.
74. O'Connor S, M., et al., *Adsorption of plasma proteins on to poly(ethylene oxide)/poly(propylene oxide) triblock copolymer films: a focus on fibrinogen.* Biotechnol Appl Biochem, 2000. **31 (Pt 3)**: p. 185-96.
75. Otsuka, H., Y. Nagasaki, and K. Kataoka, *Surface characterization of functionalized polylactide through the coating with heterobifunctional poly(ethylene glycol)/polylactide block copolymers.* Biomacromolecules, 2000. **1**(1): p. 39-48.
76. Pavey, K.D. and C.J. Olliff, *SPR analysis of the total reduction of protein adsorption to surfaces coated with mixtures of long- and short-chain polyethylene oxide block copolymers.* Biomaterials, 1999. **20**(9): p. 885-90.
77. Sit, P.S. and J. Kohn, *Interrelationship of micromechanics and morphology of fibroblasts adhered on different polymeric surfaces.* Acta Biomaterialia, 2009. **5**(8): p. 2823-2831.
78. Lee, J.H., H.B. Lee, and J.D. Andrade, *Blood compatibility of polyethylene oxide surfaces.* Progress in Polymer Science, 1995. **20**(6): p. 1043-1079.
79. Jeon, S.I. and J.D. Andrade, *Protein Surface Interactions in the Presence of Polyethylene Oxide .2. Effect of Protein Size.* Journal of Colloid and Interface Science, 1991. **142**(1): p. 159-166.
80. Leibler, L., *Theory of Microphase Separation in Block Copolymers.* Macromolecules, 1980. **13**: p. 1602-1617.
81. Bates, F.S., *Polymer-Polymer Phase-Behavior.* Science, 1991. **251**(4996): p. 898-905.
82. Park, C., J. Yoon, and E.L. Thomas, *Enabling nanotechnology with self assembled block copolymer patterns.* Polymer, 2003. **44**(22): p. 6725-6760.
83. Ruzette, A.V. and L. Leibler, *Block copolymers in tomorrow's plastics.* Nature Materials, 2005. **4**(1): p. 19-31.

84. Okano, T., et al., *Hydrophilic-Hydrophobic Microdomain Surfaces Having an Ability to Suppress Platelet-Aggregation and Their Invitro Antithrombogenicity.* Journal of Biomedical Materials Research, 1986. **20**(7): p. 919-927.
85. Read, D.J., *Mean field theory for phase separation during polycondensation reactions and calculation of structure factors for copolymers of arbitrary architecture.* Macromolecules, 1998. **31**(3): p. 899-911.
86. Subbotin, A.V. and A.N. Semenov, *Phase equilibria in random multiblock copolymers.* European Physical Journal E, 2002. **7**(1): p. 49-64.
87. Pellegrini, N.N., et al., *Random copolymer/homopolymer interfacial widths as a function of copolymer composition.* Polymer, 2000. **41**(7): p. 2701-2704.
88. Edgecombe, B.D., et al., *The role of polymer architecture in strengthening polymer-polymer interfaces: A comparison of graft, block, and random copolymers containing hydrogen-bonding moieties.* Macromolecules, 1998. **31**(4): p. 1292-1304.
89. Staudinger, U., et al., *Enhancement of mechanical properties of triblock copolymers by random copolymer middle blocks.* European Polymer Journal, 2007. **43**(6): p. 2750-2758.
90. Aoike, T., et al., *Control of tribological properties with a series of random copolymers.* Langmuir, 2002. **18**(7): p. 2949-2951.
91. Nagaoka, S., et al., *Hydrated Dynamic Surfaces.* ASAIO Journal, 1987. **33**(2): p. 76-78.
92. Sofia, S.J., V. Premnath, and E.W. Merrill, *Poly(ethylene oxide) grafted to silicon surfaces: Grafting density and protein adsorption.* Macromolecules, 1998. **31**(15): p. 5059-5070.
93. Lynd, N.A. and M.A. Hillmyer, *Effects of polydispersity on the order-disorder transition in block copolymer melts.* Macromolecules, 2007. **40**(22): p. 8050-8055.
94. Bacakova, L., et al., *Cell adhesion on artificial materials for tissue engineering.* Physiological Research, 2004. **53**: p. S35-S45.
95. Chen, C.S., et al., *Cell shape provides global control of focal adhesion assembly.* Biochem Biophys Res Commun, 2003. **307**(2): p. 355-61.
96. Garcia, A.J., M.D. Vega, and D. Boettiger, *Modulation of cell proliferation and differentiation through substrate-dependent changes in fibronectin conformation.* Mol Biol Cell, 1999. **10**(3): p. 785-98.
97. Ueda, T., et al., *Preparation of 2-Methacryloyloxyethyl Phosphorylcholine Copolymers with Alkyl Methacrylates and Their Blood Compatibility.* Polymer Journal, 1992. **24**(11): p. 1259-1269.
98. Weber, N., et al., *Viscoelastic properties of fibrinogen adsorbed to the surface of biomaterials used in blood-contacting medical devices.* Langmuir, 2007. **23**(6): p. 3298-304.
99. James, K., et al., *Small changes in polymer chemistry have a large effect on the bone-implant interface: evaluation of a series of degradable tyrosine-derived polycarbonates in bone defects.* Biomaterials, 1999. **20**(23-24): p. 2203-2212.
100. Sheihet, L., et al., *Effect of tyrosine-derived triblock copolymer compositions on nanosphere self-assembly and drug delivery.* Biomacromolecules, 2007. **8**(3): p. 998-1003.

101. Ertel, S.I. and J. Kohn, *Evaluation of a Series of Tyrosine-Derived Polycarbonates as Degradable Biomaterials.* Journal of Biomedical Materials Research, 1994. **28**(8): p. 919-930.
102. Hoven, V.P., A. Poopattanapong, and J. Kohn, *Acid-containing tyrosine-derived polycarbonates: Wettability and surface reactivity.* Macromolecular Symposia, 2004. **216**: p. 87-97.
103. Macario, D.K., et al., *Iodine inhibits antiadhesive effect of PEG: Implications for tissue engineering.* Journal of Biomedical Materials Research Part B-Applied Biomaterials, 2008. **86B**(1): p. 237-244.
104. Yu, C. and J. Kohn, *Tyrosine-PEG-derived poly(ether carbonate)s as new biomaterials - Part I: Synthesis and evaluation.* Biomaterials, 1999. **20**(3): p. 253-264.
105. Bourke, S.L. and J. Kohn, *Polymers derived from the amino acid L-tyrosine: polycarbonates, polyarylates and copolymers with poly(ethylene glycol).* Advanced Drug Delivery Reviews, 2003. **55**(4): p. 447-466.
106. Hooper, K.A., N.D. Macon, and J. Kohn, *Comparative histological evaluation of new tyrosine-derived polymers and poly (L-lactic acid) as a function of polymer degradation.* Journal of Biomedical Materials Research, 1998. **41**(3): p. 443-454.
107. Hooper, K.A., et al., *Characterization of the inflammatory response to biomaterials using a rodent air pouch model.* Journal of Biomedical Materials Research, 2000. **50**(3): p. 365-374.
108. Weber, N., H.P. Wendel, and J. Kohn, *Formation of viscoelastic protein layers on polymeric surf aces relevant to platelet adhesion.* Journal of Biomedical Materials Research Part A, 2005. **72A**(4): p. 420-427.
109. Hall, P.J., et al., *Use of contrast-enhanced small-angle neutron scattering to monitor the effects of solvent swelling on the pore structure of styrene-divinylbenzene resins.* Journal of the Chemical Society-Faraday Transactions, 1997. **93**(3): p. 463-466.
110. Murthy, N.S., et al., *Structural-Changes Accompanying Hydration in Nylon-6.* Macromolecules, 1989. **22**(3): p. 1261-1267.
111. Motokawa, R., et al., *Small-angle neutron scattering study on microstructure of poly(N-isopropylacrylamide)-block-poly(ethylene glycol) in water.* Colloids and Surfaces B: Biointerfaces, 2004. **38**(3-4): p. 213-219.
112. Stanley, C., et al., *Protein Structure and Hydration Probed by SANS and Osmotic Stress.* Biophysical Journal, 2008. **94**(7): p. 2777-2789.
113. Matsushita, Y., et al., *Localization of a homopolymer dissolved in a lamellar structure of a block copolymer studied by small-angle neutron scattering.* Macromolecules, 1993. **26**(24): p. 6346-6349.
114. Vaccaro, A., et al., *Structure of an Adsorbed Polyelectrolyte Monolayer on Oppositely Charged Colloidal Particles.* Langmuir, 2009. **25**(9): p. 4864-4867.
115. Hellmann, E.H., G.P. Hellmann, and A.R. Rennie, *Solvent-induced phase separation in polycarbonate blends PC/TMPC.* Colloid & Polymer Science, 1991. **269**(4): p. 343-352.
116. Martin, J.E. and A.J. Hurd, *Scattering from Fractals.* Journal of Applied Crystallography, 1987. **20**: p. 61-78.
117. Porod, G., Kolloid Z., 1951. **124**: p. 83-114.

118. Laity, P.R., et al., *A review of small-angle scattering models for random segmented poly(ether-urethane) copolymers.* Polymer, 2004. **45**(21): p. 7273-7291.
119. Falt, S., L. Wagberg, and E.L. Vesterlind, *Swelling of model films of cellulose having different charge densities and comparison to the swelling behavior of corresponding fibers.* Langmuir, 2003. **19**(19): p. 7895-7903.
120. Hu, X.F. and J. Ji, *Construction of Multifunctional Coatings via Layer-by-Layer Assembly of Sulfonated Hyperbranched Polyether and Chitosan.* Langmuir, 2010. **26**(4): p. 2624-2629.
121. Wittmer, C.R., et al., *Fibronectin terminated multilayer films: Protein adsorption and cell attachment studies.* Biomaterials, 2007. **28**(5): p. 851-860.
122. Xia, H.W., et al., *pH Induced DNA Folding at Interface.* Journal of Physical Chemistry B, 2010. **114**(2): p. 775-779.
123. Zhang, G.Z. and C. Wu, *Quartz Crystal Microbalance Studies on Conformational Change of Polymer Chains at Interface.* Macromolecular Rapid Communications, 2009. **30**(4-5): p. 328-335.
124. Fant, C., H. Elwing, and F. Hook, *The influence of cross-linking on protein-protein interactions in a marine adhesive: The case of two byssus plaque proteins from the blue mussel.* Biomacromolecules, 2002. **3**(4): p. 732-741.
125. Steinmetz, N.F., et al., *Assembly of multilayer arrays of viral nanoparticles via biospecific recognition: A quartz crystal microbalance with dissipation monitoring study.* Biomacromolecules, 2008. **9**(2): p. 456-462.
126. Snabe, T., M.T. Neves-Petersen, and S.B. Petersen, *Enzymatic lipid removal from surfaces-lipid desorption by a pH-induced "electrostatic explosion".* Chemistry and Physics of Lipids, 2005. **133**(1): p. 37-49.
127. Feiler, A.A., et al., *Adsorption and viscoelastic properties of fractionated mucin (BSM) and bovine serum albumin (BSA) studied with quartz crystal microbalance (QCM-D).* Journal of Colloid and Interface Science, 2007. **315**(2): p. 475-481.
128. Lord, M.S., et al., *Lysozyme interaction with poly(HEMA)-based hydrogel.* Biomaterials, 2006. **27**(8): p. 1341-1345.
129. Sauerbrey, G., Zeitschrif für Physik, 1959. **155**: p. 206-222.
130. Vogt, B.D., et al., *Effect of film thickness on the validity of the Sauerbrey equation for hydrated polyelectrolyte films.* Journal of Physical Chemistry B, 2004. **108**(34): p. 12685-12690.
131. Voinova, M.V., et al., *Viscoelastic acoustic response of layered polymer films at fluid-solid interfaces: Continuum mechanics approach.* Physica Scripta, 1999. **59**(5): p. 391-396.
132. Höök, F. and B. Kasemo, *The QCM-D Technique for Probing Biomacromolecular Recognition Reactions*. 2007. p. 425-447.
133. Jaiswal, A., *Introduction to Data Analysis*. 2008, Q-Sense.
134. Hook, F., et al., *Variations in coupled water, viscoelastic properties, and film thickness of a Mefp-1 protein film during adsorption and cross-linking: a quartz crystal microbalance with dissipation monitoring, ellipsometry, and surface plasmon resonance study.* Anal Chem, 2001. **73**(24): p. 5796-804.
135. Hook, F., et al., *A comparative study of protein adsorption on titanium oxide surfaces using in situ ellipsometry, optical waveguide lightmode spectroscopy,*

and quartz crystal microbalance/dissipation. Colloids and Surfaces B-Biointerfaces, 2002. **24**(2): p. 155-170.
136. Pesnell, A., *A Focused Library of Tyrosine-Derived Polycarbonates for the Discovery of Optimal Polymers for Use in Resorbable Stents*, in *Chemistry and Chemical Biology*. 2006, Rutgers University: Piscataway, NJ. p. 130.
137. Rojas, R., et al., *Evaluation of Automated Synthesis for Chain and Step-Growth Polymerizations: Can Robots Replace the Chemists?* Journal of Polymer Science Part a-Polymer Chemistry, 2009. **47**(1): p. 49-58.
138. Gases, B., *Phosgene*, in *Material Safety Data Sheet*. 1996.
139. Johnson, R.E. and R.H. Dettre, *Wettability and Contact Angles*, in *Surface and Colloid Science*, E. Matijevic and F.R. Eirich, Editors. 1969, Wiley Interscience: New York, New York. p. 85-153.
140. Deshmukh, R.R. and A.R. Shetty, *Comparison of surface energies using various approaches and their suitability.* Journal of Applied Polymer Science, 2008. **107**(6): p. 3707-3717.
141. Ozcan, C. and N. Hasirci, *Evaluation of surface free energy for PMMA films.* Journal of Applied Polymer Science, 2008. **108**(1): p. 438-446.
142. Fowkes, F.M., *ADDITIVITY OF INTERMOLECULAR FORCES AT INTERFACES. I. DETERMINATION OF THE CONTRIBUTION TO SURFACE AND INTERFACIAL TENSIONS OF DISPERSION FORCES IN VARIOUS LIQUIDS1.* The Journal of Physical Chemistry, 1963. **67**(12): p. 2538-2541.
143. Hara, M.R., M.B. Cascio, and A. Sawa, *GAPDH as a sensor of NO stress.* Biochim Biophys Acta, 2006. **1762**(5): p. 502-9.
144. Dastoor, Z. and J.L. Dreyer, *Potential role of nuclear translocation of glyceraldehyde-3-phosphate dehydrogenase in apoptosis and oxidative stress.* J Cell Sci, 2001. **114**(Pt 9): p. 1643-53.
145. Sung, H.J., et al., *Synthetic polymeric substrates as potent pro-oxidant versus anti-oxidant regulators of cytoskeletal remodeling and cell apoptosis.* J Cell Physiol, 2009. **218**(3): p. 549-57.
146. Sousa, A., et al., *Nanoscale morphological changes during hydrolytic degradation and erosion of a bioresorbable polymer.* Macromolecules, 2006. **39**(21): p. 7306-7312.
147. Deng, X.M., et al., *Studies on the Block Copolymerization of D,L-Lactide and Poly(Ethylene Glycol) with Aluminum Complex Catalyst.* Journal of Applied Polymer Science, 1995. **55**(8): p. 1193-1196.
148. Deschamps, A.A., et al., *In vivo and in vitro degradation of poly(ether ester) block copolymers based on poly(ethylene glycol) and poly(butylene terephthalate).* Biomaterials, 2004. **25**(2): p. 247-258.
149. Tziampazis, E., J. Kohn, and P.V. Moghe, *PEG-variant biomaterials as selectively adhesive protein templates: model surfaces for controlled cell adhesion and migration.* Biomaterials, 2000. **21**(5): p. 511-520.
150. Kranz, H., et al., *Physicomechanical properties of biodegradable poly(D,L-lactide) and poly(D,L-lactide-co-glycolide) films in the dry and wet states.* Journal of Pharmaceutical Sciences, 2000. **89**(12): p. 1558-1566.
151. Kim, S.H., et al., *Mechanical properties of biodegradable blends of poly(L-lactic acid) and starch.* Korea Polymer Journal, 1998. **6**(5): p. 422-427.

152. Li, S.M. and S. McCarthy, *Influence of crystallinity and stereochemistry on the enzymatic degradation of poly(lactide)s.* Macromolecules, 1999. **32**(13): p. 4454-4456.
153. Hurrell, S. and R.E. Cameron, *Polyglycolide: degradation and drug release. Part I: Changes in morphology during degradation.* Journal of Materials Science: Materials in Medicine, 2001. **12**(9): p. 811-816.
154. Gopferich, A., *Mechanisms of polymer degradation and erosion.* Biomaterials, 1996. **17**(2): p. 103-114.
155. de Oca, H.M., et al., *Structure Development during Crystallization and Solid-State Processing of Poly(glycolic acid).* Journal of Applied Polymer Science, 2009. **111**(2): p. 1013-1018.
156. Murthy, N.S., M.K. Akkapeddi, and W.J. Orts, *Analysis of lamellar structure in semicrystalline polymers by studying the absorption of water and ethylene glycol in nylons using small-angle neutron scattering.* Macromolecules, 1998. **31**(1): p. 142-152.
157. Murthy, N.S. and W.J. Orts, *Hydration in Semicrystalline Polymers - Small-Angle Neutron-Scattering Studies of the Effect of Drawing in Nylon-6 Fibers.* Journal of Polymer Science Part B-Polymer Physics, 1994. **32**(16): p. 2695-2703.
158. Murthy, N.S., et al., *Structural Changes Accompanying Hydration in Nylon 6.* Macromolecules, 1989. **22**: p. 1261-1267.
159. Husken, D. and R.J. Gaymans, *The structure of water in PEO-based segmented block copolymers and its effect on transition temperatures.* Macromol. Chem. Phys., 2008. **209**: p. 967-979.
160. Mottu, F., et al., *Iodine-containing cellulose mixed esters as radiopaque polymers for direct embolization of cerebral aneurysms and arteriovenous malformations.* Biomaterials, 2002. **23**(1): p. 121-131.
161. James, N.R., J. Philip, and A. Jayakrishnan, *Polyurethanes with radiopaque properties.* Biomaterials, 2006. **27**(2): p. 160-166.
162. Bedoui, F., et al. *Enhancement of Mechanical Properties Upon Hydration in Copolymers of PEG and Iodinated tyrosine-derived Polycarbonates*. in *Mechanics of Biological and Biomedical Materials*. 2009.
163. Bedoui, F., et al. *Enhancement of Mechanical Properties Upon Hydration in Copolymers of PEG and Iodinated tyrosine-derived Polycarbonates*. in *MRS*. 2009.
164. Park, A. and L.G. Cima, *In vitro cell response to differences in poly-L-lactide crystallinity.* Journal of Biomedical Materials Research, 1996. **31**(1): p. 117-130.
165. Brash, J.L. and T.A. Horbett, *Proteins at Interfaces, An Overview*. Proteins at Interfaces II, Fundamentals and Applications. 1995: American Chemical Society. 1-23.
166. Llanos, G.R. and M.V. Sefton, *Does polyethylene oxide possess a low thrombogenicity?* J Biomater Sci Polymer Edn., 1993. **4**(4): p. 381-400.
167. Gombotz, W.R., et al., *Protein adsorption to poly(ethylene oxide) surfaces.* J Biomed Mater Res, 1991. **25**(12): p. 1547-62.
168. Malmsten, M., K. Emoto, and J.M. Van Alstine, *Effect of chain density on inhibition of protein adsorption by poly(ethylene glycol) based coatings.* Journal of Colloid and Interface Science, 1998. **202**(2): p. 507-517.

169. Wu, Y.L.J., et al., *Non-fouling surfaces produced by gas phase pulsed plasma polymerization of an ultra low molecular weight ethylene oxide containing monomer.* Colloids and Surfaces B-Biointerfaces, 2000. **18**(3-4): p. 235-248.
170. Herold, D.A., K. Keil, and D.E. Bruns, *Oxidation of polyethylene glycols by alcohol dehydrogenase.* Biochem Pharmacol, 1989. **38**(1): p. 73-6.
171. Yamaoka, T., Y. Tabata, and Y. Ikada, *Distribution and tissue uptake of poly(ethylene glycol) with different molecular weights after intravenous administration to mice.* J Pharm Sci, 1994. **83**(4): p. 601-6.
172. Meier, M.A.R. and U.S. Schubert, *Combinatorial polymer research and high-throughput experimentation: powerful tools for the discovery and evaluation of new materials.* Journal of Materials Chemistry, 2004. **14**(22): p. 3289-3299.
173. Rojas, R., *Exploration of biomaterials design space through combinatorial and high-throughput approaches: tyrosine-derived polycarbonates as a test study*, in *Chemistry*. 2009, Rutgers University: Piscataway. p. 167.
174. Higgins, J.S. and H.C. Benoit, *Polymers and Neutron Scattering*. 1994, Oxford: Clarendon.
175. Andrade, J.D. and W.Y. Chen, *Probing Polymer Surface Dynamics by Contact-Angle Hysteresis and Esca.* Surface and Interface Analysis, 1986. **9**(1-6): p. 418-418.
176. Andrade, J.D., L.M. Smith, and D.E. Gregonis, *The Contact Angle and Surface Energetics*, in *Surface and Interfacial Aspects of Biomedical Polymers, Volume 1: Surface Chemistry and Physics*, J.D. Andrade, Editor. 1985, Plenum Press: New York, NY. p. 249-292.
177. Fowkes, F.M., *DETERMINATION OF INTERFACIAL TENSIONS, CONTACT ANGLES, AND DISPERSION FORCES IN SURFACES BY ASSUMING ADDITIVITY OF INTERMOLECULAR INTERACTIONS IN SURFACES.* The Journal of Physical Chemistry, 1962. **66**(2): p. 382-382.
178. Comelles, J., et al., *The role of surface energy of technical polymers in serum protein adsorption and MG-63 cells adhesion.* Nanomedicine: Nanotechnology, Biology and Medicine, 2010. **6**(1): p. 44-51.
179. Stupack, D.G. and D.A. Cheresh, *Get a ligand, get a life: integrins, signaling and cell survival.* J Cell Sci, 2002. **115**(19): p. 3729-3738.
180. Zhang, Z., et al., *The alpha 5 beta 1 integrin supports survival of cells on fibronectin and up-regulates Bcl-2 expression.* Proc Natl Acad Sci U S A, 1995. **92**(13): p. 6161-5.
181. Streuli, C.H., *Integrins and cell-fate determination.* J Cell Sci, 2009. **122**(2): p. 171-177.
182. Folkman, J. and A. Moscona, *Role of cell shape in growth control.* Nature, 1978. **273**(5661): p. 345-9.
183. Meredith, J.E., Jr. and M.A. Schwartz, *Integrins, adhesion and apoptosis.* Trends Cell Biol, 1997. **7**(4): p. 146-50.
184. Frisch, S.M. and H. Francis, *Disruption of epithelial cell-matrix interactions induces apoptosis.* J Cell Biol, 1994. **124**(4): p. 619-26.
185. Meredith, J.E., Jr., B. Fazeli, and M.A. Schwartz, *The extracellular matrix as a cell survival factor.* Mol Biol Cell, 1993. **4**(9): p. 953-61.

186. Chuang, D.M., C. Hough, and V.V. Senatorov, *Glyceraldehyde-3-phosphate dehydrogenase, apoptosis, and neurodegenerative diseases.* Annu Rev Pharmacol Toxicol, 2005. **45**: p. 269-90.
187. Chen, C.S., et al., *Geometric control of cell life and death.* Science, 1997. **276**(5317): p. 1425-8.
188. Lynd, N.A. and M.A. Hillmyer, *Influence of polydispersity on the self-assembly of diblock copolymers.* Macromolecules, 2005. **38**(21): p. 8803-8810.
189. Lynd, N.A., A.J. Meuler, and M.A. Hillmyer, *Polydispersity and block copolymer self-assembly.* Progress in Polymer Science, 2008. **33**(9): p. 875-893.
190. Ryan, P.L., et al., *Tissue spreading on implantable substrates is a competitive outcome of cell-cell vs. cell-substratum adhesivity.* Proc Natl Acad Sci U S A, 2001. **98**(8): p. 4323-7.
191. Bornside, D.E., C.W. Macosko, and L.E. Scriven, *ON THE MODELING OF SPIN COATING.* Journal of Imaging Technology, 1987. **13**(4): p. 122-130.

Curriculum Vitae

Arnold Luk

Education

Rutgers University, Piscataway, NJ,
Ph. D. in Biomedical Engineering, Advisor: Dr. Joachim Kohn
September 2004 – October 2010

Drexel University, Philadelphia, PA
B.S., Biomedical Engineering, Minor: Business Administration
September 1999 – June 2004

Professional Experience

Elan Drug Delivery, King of Prussia, PA
Process Engineering Technical Services Co-op
March 2003 – September 2003

Abbey Color, Philadelphia, PA
Quality Control Technician
March 2002 – September 2002

GlaxoSmithKline, Conshohocken, PA
Associate Engineer Co-op
March 2001 – September 2001

Teaching Experience

Rutgers University, Piscataway, NJ
Teaching Assistant, Biomedical Engineering Senior Design
September 2005 – May 2006

Publications

Johnson, P.A., **Luk, A.**, Demtchouk, A., Patel, H., Sung, H-J., Treiser, M.D., Gordonov, S., Sheihet, L., Bolikal, D., Kohn, J., Moghe, P.V. Interplay of anionic charge, poly(ethylene glycol), and iodinated tyrosine incorporation within tyrosine-derived polycarbonates: Effects on vascular smooth muscle cell adhesion, proliferation, and motility. Journal of Biomedical Materials Research, 93A, 505-514, 2010.

Luk, A., Rojas, R., Murthy, N.S., Bolikal, D., Kohn, J. Examinations of physicochemical factors that cause polymeric substrates to transition between protein adsorption and repellence, PMSE Preprints, Vol. 102, Spring 2010.

Bedoui, F., Widjaja, L.K., **Luk, A.**, Bolikal, D., Murthy, N.S., Kohn, J. Enhancement of Mechanical Properties Upon Hydration in Copolymers of PEG and Iodinated Tyrosine-derived Polycarbonates. Materials Research Society Symposium Proceedings, Vol. 1132, 2009, 1132-Z09-12.

Sung, H-J.*, **Luk, A.***, Murthy, N.S., Liu, E., Joy, A., Bushman, J., Kohn, J., Moghe, P.V. Poly(ethylene glycol) as a potent matrix regulator for focal adhesion-mediated cell survival and apoptosis. Submitted to Soft Matter. *Equal first authors.

Luk, A., Murthy, N.S., Wang, W., Kohn, J. Study of hydration in random multiblock PEG-containing hydrophobic polymers using small-angle neutron scattering. In preparation.

Luk, A., Rojas, R., Murthy, N.S., Kohn, J. Examination of physicochemical factors that cause polymeric substrates to transition between protein adsorption and repellence. In preparation.

Joy, A., Cohen, D.M., **Luk, A.**, Anim-Danso, E., Chen, C., Kohn, J. Effect of surface peptides on polymer films overrides the influences of chemical composition and modulus in a library of methacrylate polymers. In preparation.